



UNIVERSITÀ DEGLI STUDI DI NAPOLI
FEDERICO II



UNIVERSITÀ DEGLI STUDI DI NAPOLI FEDERICO II

PH.D. THESIS IN

INFORMATION TECHNOLOGY AND ELECTRICAL ENGINEERING

**PATTERN RECOGNITION IN BREAST DCE-MRI
AUTOMATIC CANCER ANALYSIS**

GABRIELE PIANTADOSI

TUTOR: PROF. CARLO SANSONE

CO- TUTOR: PROF. MARIO SANSONE

XXIX CICLO

SCUOLA POLITECNICA E DELLE SCIENZE DI BASE

DIPARTIMENTO DI INGEGNERIA ELETTRICA E TECNOLOGIE DELL'INFORMAZIONE

*to my loving family and
to my love...*

Acknowledgements

I would like to express my appreciation and thanks to my advisors Professor Carlo Sansone and Professor Mario Sansone, you have been as mentors for me by encouraging my research and by allowing me to grow as a research scientist. Your advice on both research as well as on my career have been priceless.

A special thanks to Stefano Marrone, my lab mate, for the stimulating “discussions”, for the brilliant suggestions, for the sleepless nights we were working together before deadlines, and for all the fun we have had in the last years.

I am also grateful to Dr. Antonella Petrillo, Head of Division of Radiology, Department of Diagnostic Imaging, Radiant and Metabolic Therapy, “Istituto Nazionale dei Tumori Fondazione G. Pascale”-IRCCS, Naples, Italy, for providing access to DCE-MRI data. Moreover, we would like to thank PhD Roberta Fusco, from the same institution, for useful discussions.

Table of contents

Summary	1
1 Introduction	5
1.1 Breast cancer	5
1.2 Biomedical Imaging	8
1.2.1 Techniques for breast imaging	8
1.2.2 Magnetic Resonance Imaging (MRI)	12
1.3 Analysis of DCE-MRI for Breast Cancer	19
1.3.1 Computer-Aided Detection and Diagnosis	20
1.3.2 Therapy planning	35
2 Literature Review	37
2.1 Pre-processing	39
2.1.1 Breast Mask	40
2.1.2 Motion Correction	43
2.2 Lesion Detection	46
2.3 Tumour Diagnosis	51
2.4 Therapy Assessment	56

2.5	Datasets	59
3	Automated Detection, Diagnosis and Therapy assessment	65
3.1	Pre-processing	67
3.1.1	Breast Mask Extraction	67
3.1.2	Motion Correction	77
3.2	Lesion Detection	89
3.2.1	Pre-selection	89
3.2.2	Feature extraction	91
3.2.3	Segmentation by Classification	92
3.3	Lesion Diagnosis	93
3.3.1	LBP descriptor	93
3.3.2	Classification	95
3.4	Therapy Assessment	96
3.4.1	Feature Extraction	96
3.4.2	Classification	99
3.5	Putting it all together	100
3.6	Remote Computing	100
3.6.1	Architecture layers	101
3.6.2	Communication layer	103
3.6.3	Orchestrator layer	106
3.6.4	Application layer	108
3.6.5	Orchestrator layer implementation	108
3.6.6	Application layer implementation	112
3.6.7	Architecture behaviour	114
3.6.8	Exploit Parallelism	116
4	Experimental Results	117
4.1	Datasets	118
4.2	Evaluation Strategies	121
4.2.1	Breast mask and Segmentation evaluation	121

4.2.2	Motion Correction Quality Index evaluations	122
4.2.3	Remote Architecture evaluation	124
4.3	Pre-processing Phases	126
4.3.1	Breast Mask Extraction	126
4.3.2	Data Driven MCT Selection	131
4.4	Lesion Detection	135
4.5	Lesion Diagnosis	140
4.6	Therapy Assessment	144
4.7	Putting it all together	146
4.8	Remote Architecture	146
4.8.1	Compression tests	146
4.8.2	Transmission and Execution tests	148
4.8.3	Scalability evaluation	149
5	Discussion and Conclusions	151
6	Open Issues	161
	Bibliography	165
	List of figures	197
	List of tables	201

Summary

Breast cancer is the most common women tumour worldwide, about 2 million new cases diagnosed each year (second most common cancer overall). This disease represents about 12% of all new cancer cases and 25% of all cancers in women. Early detection of breast cancer is one of the key factors in determining the prognosis for women with malignant tumours. The standard diagnostic tool for the detection of breast cancer is x-ray mammography. The disadvantage of this method is its low specificity, especially in the case of radiographically dense breast tissue (young or under-forty women), or in the presence of scars and implants within the breast.

Dynamic Contrast-Enhanced Magnetic Resonance Imaging (DCE-MRI) has demonstrated a great potential in the screening of high-risk women for breast cancer, in staging newly diagnosed patients and in assessing therapy effects.

However, due to the large amount of information, DCE-MRI manual examination is error prone and can hardly be inspected without the use of a Computer-Aided Detection and Diagnosis (CAD) system. Breast imaging analysis is made harder by the dynamical characteristics of soft tissues since

any patient movements (such as involuntary due to breathing) may affect the voxel-by-voxel dynamical analysis.

Breast DCE-MRI computer-aided analysis needs a pre-processing stage to identify breast parenchyma and reduce motion artefacts. Among the major issues in developing CAD for breast DCE-MRI, there is the detection and classification of lesions according to their aggressiveness. Moreover, it would be convenient to determine those subjects who are likely to not respond to the treatment so that a modification may be applied as soon as possible, relieving them from potentially unnecessary or toxic treatments.

In this thesis, an automated CAD system is presented. The proposed CAD aims to support radiologist in lesion detection, diagnosis and therapy assessment after a suitable preprocessing stage.

Segmentation of breast parenchyma has been addressed relying on fuzzy binary clustering, breast anatomical priors and morphological refinements. The breast mask extraction module combines three 2D Fuzzy C-Means clustering (executed from the three projection, axial, coronal and transversal) and geometrical breast anatomy characterization. In particular, seven well-defined key-points have been considered in order to accurately segment breast parenchyma from air and chest-wall.

To diminish the effects of involuntary movement artefacts, it is usual to apply a motion correction of the DCE-MRI volumes before of any data analysis. However, there is no evidence that a single Motion Correction Technique (MCT) can handle different deformations - small or large, rigid or non-rigid - and different patients or tissues. Therefore, it would be useful to develop a quality index (QI) to evaluate the performance of different MCTs. The existent QI might not be adequate to deal with DCE-MRI data because of the intensity variation due to contrast media. Therefore, in developing a novel QI, the underlying idea is that once DCE-MRI data have been realigned using a specific MCT, the dynamic course of the signal intensity should be as close as possible to physiological models, such as the currently accepted ones (e.g.

Tofts-Kermode, Extended Tofts-Kermode, Hayton-Brady, Gamma Capillary Transit Time, etc.). The motion correction module ranks all the MCTs, using the QI, selects the best MCT and applies a correction before of further data analysis.

The proposed lesion detection module performs the segmentation of lesions in Regions of Interest (ROIs) by means of classification at a pixel level. It is based on a Support Vector Machine (SVM) trained with dynamic features, extracted from a suitably pre-selected area by using a pixel-based approach. The pre-selection mask strongly improves the final result.

The lesion classification module evaluates the malignity of each ROI by means of 3D textural features. The Local Binary Patterns descriptor has been used in the Three Orthogonal Planes (LBP-TOP) configuration. A Random Forest has been used to achieve the final classification into a benignant or malignant lesion.

The therapy assessment stage aims to predict the patient primary tumour recurrence to support the physician in the evaluation of the therapy effects and benefits. For each patient which has at least a malignant lesion, the recurrence of the disease has been evaluated by means of a multiple classifiers system. A set of dynamic, textural, clinicopathologic and pharmacokinetic features have been used to assess the probability of recurrence for the lesions.

Finally, to improve the usability of the proposed work, we developed a framework for tele-medicine that allows advanced medical image remote analysis in a secure and versatile client-server environment, at a low cost. The benefits of using the proposed framework will be presented in a real-case scenario where OsiriX, a wide-spread medical image analysis software, is allowed to perform advanced remote image processing in a simple manner over a secure channel.

The proposed CAD system have been tested on real breast DCE-MRI data for the available protocols. The breast mask extraction stage shows a median segmentation accuracy and Dice similarity index of 98% and 93% respectively

and 100% of neoplastic lesion coverage. The motion correction module is able to rank the MCTs with an accordance of 74% with a ‘reference ranking’. Moreover, by only using 40% of the available volume, the computational load is reduced selecting always the best MCT. The automatic detection maximises the area of correctly detected lesions while minimising the number of false alarms with an accuracy of 99% and the lesions are, then, diagnosed according to their stage with an accuracy of 85%. The therapy assessment module provides a forecasting of the tumour recurrence with an accuracy of 78% and an AUC of 79%. Each module has been evaluated by a leave-one-patient-out approach, and results show a confidence level of 95% ($p < 0.05$).

Finally, the proposed remote architecture showed a very low transmission overhead which settles on about 2.5% for the widespread 10/100 Mbps. Security has been achieved using client-server certificates and up-to-date standards.

Introduction

Mammary gland is an even and symmetrical organ, placed on the front wall of the chest, consists mainly of a fibrous tissue, a glandular component (15-20 lobes, each of which consists of lobules and each lobule has a lactiferous - from Greek 'that carries milk' - duct that drains into openings in the nipple), and an adipose tissue, more extended than glandular and fibrous tissues (Figure 1.1).

In order to understand the techniques, methods and approaches used in this thesis, it is necessary to investigate the context in which they were developed, describing the main types, the related characteristics of breast cancer and the theory behind the Dynamic Contrast-Enhanced Magnetic Resonance Imaging (DCE-MRI), focusing on the features that are particularly useful in highlighting the characteristics of neoplasms in exam.

1.1 Breast cancer

Our earliest written record regarding cancer (although the word cancer was not used) was discovered in Egypt and dates back to about 3000 BC. It is called the 'Edwin Smith Papyrus' and is a copy of part of an ancient Egyptian textbook on trauma surgery. It describes eight cases of tumours or ulcers

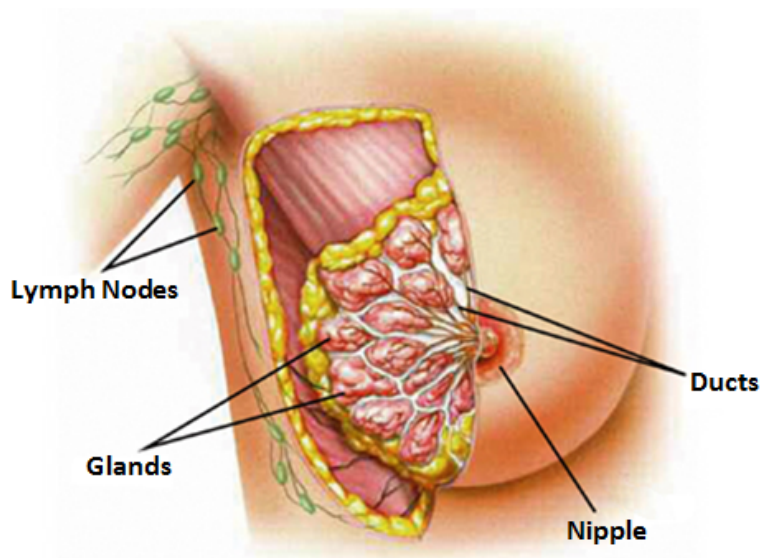


Figure 1.1: A female breast and its main parts.

of the breast that were treated by cauterisation with a tool called the fire drill. The conclusion of the document was: ‘There is no treatment’ [10, 93]. Nowadays, the surgery treatment is not the only possible approach. The modern knowledge of the disease is an important factor in the planning of curative or palliative therapy.

The number of cases of breast cancer worldwide has significantly increased since the 1970s, a phenomenon partly attributed to the modern lifestyles of Western world; in fact, recent studies have shown that tumours are, for the most part, environmental disease rather than genetic, with a ratio of 9:1 in cases attributable to environmental factors than cases attributable to genetic factors [11]. Among the environmental factors, we also have to consider any ethological factor is not genetically inherited, such as pollution, smoking, nutrition, radiation, stress, and traumas [23].

Neoplasms of the breast represent the most important lesions of this organ, although not the most frequent, they may assume macroscopic and

histological aspects extremely variable according to the type of tissue from which they originate. It is worth to note that breast cancer can also affect the men (even if it represents less of 1% of all male cancers) [83, 123]. In both sexes, the incidence is higher in the left breast and upper-outer quadrant breast as shown in fig.1.2 [62, 196].

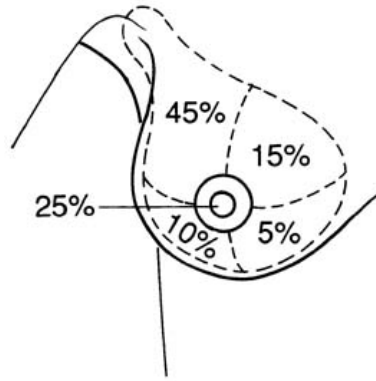


Figure 1.2: Spatial incidence of breast cancer.

It is possible to rank breast tumours according to a standardised classification system introduced specifically to simplify the communication process of medical oncologists; discriminating characteristics are the involved tumoural tissue, the histological characteristics highlighted and staging.

TNM (Tumour, Nodes, Metastases) Standardisation is very used [232]; it was developed in 1987 jointly according to the criteria of the UICC (International Union Against Cancer) and AJCC (American Joint Committee on Cancer); specifically, the TNM table makes use of that codes:

- **T** distinguishes the primary tumour whose size and nature is expressed by the value that comes with it (X - 0 - IS - 1MIC, 1a, 1b, 1c, 1d - 2 - 3 - 4a, 4b, 4c, 4d). TX or T0 indicates a tumour cannot be definable or detectable; IS indicates 'In Situ' lesions and is equivalent to the first stage of the spread of tumours. T1c tumours with size up to 2 cm to gradually evolve into T4b for tumour of any size but already adherents

to the skin that has led to a hollowing or orange peel skin until T4d that indicates an inflammatory carcinoma;

- **N** indicates, if and to what extent, the lymph nodes are affected by breast cancer. The values that accompany N are different (X - 0 - 1a - 1b1, 1b2, 1b3, 1b4 - 2 - 3) and indicates by N0, absence of metastasis to N3 when there is metastatic involvement of the lymph nodes belonging to the ipsilateral internal mammary chain (N3);
- **M** refers to the presence of any metastases. MX indicates the inability to assess the presence of distant metastases, M0 confirms the absence of them and M1 locates the metastases in distant organs.

In the case of breast cancer, table 1.1 shows the main TNM codes associating them with the staging code, allowing comparing patients and the results of different treatment protocols. Moreover, it allows formulating a more accurate therapeutic and prognostic opinion.

1.2 Biomedical Imaging

With the terms ‘imaging’ or ‘biomedical imaging’ or ‘diagnostic by imaging’ refers to the generic process through which it is possible to observe an area of a body not visible from the outside. The non-invasive diagnosis plays an important supporting role in prevention programs, and it is the most effective methods for early detection of cancers. However, the effectiveness of each imaging technique needs to be evaluated in a risk/benefit balance.

1.2.1 Techniques for breast imaging

Imaging techniques applied in the research of breast diseases are:

Mammography (RX): Uses ionising radiation (X-rays) at low energy (30 kVp) to impress images of the breast on planar X-ray films. This

Stage	TNM Code	Description	5-year survival
0	Tis N0 M0	Presence of in situ carcinomas:	93%
		<ul style="list-style-type: none"> Lobular carcinoma in situ: cancer is not aggressive but can present a risk factor for formation of a malignant lesion upcoming aggressive; Ductal carcinoma in situ: affects the cells of the ducts. The possibility of having a more aggressive cancer increase. 	
I	T1 N0 M0	Cancer is in the initial phase with a diameter less of 2 cm. There are no lymph nodes involved.	88%
IIA	T0 N1 M0	Cancer is localized in the lymph nodes of the breast.	81%
	T1 N1 M0	Cancer has a maximum diameter of 2cm, with infiltration in the lymph nodes of the breast.	
	T0 N0 M0	Cancer has a diameter of between 2cm and 5cm. There are no lymph nodes involved.	
IIB	T2 N1 M0	Cancer has a diameter of between 2cm and 5cm, with infiltration in the lymph nodes of the breast.	74%
	T3 N0 M0	Cancer has a maximum diameter of 2cm. There are no lymph nodes involved.	
IIIA	T0 N2 M0	Cancer has spread to lymph nodes of the breast.	67%
	T1 N2 M0	Cancer has a maximum diameter of 2cm, with considerable infiltration in the lymph nodes of the breast.	
	T2 N2 M0	Cancer has a maximum diameter of 5cm, with considerable infiltration in the lymph nodes of the breast.	
	T3 N1 M0	Cancer has a diameter greater than 5cm, with considerable infiltration in the lymph nodes of the breast and/or other structures.	
	T3 N2 M0	Cancer has a diameter greater than 5cm, with considerable infiltration in the lymph nodes of the breast and/or other structures.	
IIIB	T4 N* M0	Cancer has spread in the tissue adjacent to the breast (skin, ribs, thoracic and pectoral muscles) with infiltration of the lymph nodes of breast and/or of axillary cavity and/or of neck and/or of clavicle.	41%
	T* N3 M0	Cancer has spread in the tissue adjacent to the breast (skin, ribs, thoracic and pectoral muscles) with infiltration of the lymph nodes of breast and/or of axillary cavity and/or of neck and/or of clavicle.	
IV	T* N* M1	Cancer has developed metastases, typically in the bones, lungs, liver and brain.	15%

Table 1.1: TNM table with stage and survival index at 5 years.

instrument is the ‘gold standard’ for breast imaging because it is a simple test, fast running, highly specific and widely available on the territory; constituting, at present, the key exam for screening programs with the ability of recognition of the lesions when the tumour is not yet visible by palpation (preclinical stage). By contrast, the ionising radiations are, in the long term, themselves the cause of tumours [18] and the image quality is lower when compared to other diagnostic methods. Sensitivity: 85-90% for adipose breasts, 70% for dense (low fat content) breasts; specificity: 90-95%.

Ultrasound (US): Based on the principles of the emission of echo and the transmission of the ultrasonic waves (between 2 and 20 Mhz.

Higher frequencies have a greater resolving power of the image, but penetrate less deeply into the subject); it is often used to complement other investigations such as mammography and clinical examination or for further diagnosis of lesions which persist dubious. In addition, the US replaces mammography in the study of hyper-dense breasts (rich of glandular tissue) as in women under 40 years (so-called ‘under-forty’). In contrast, ultrasound has a low resolving power for the breasts with a normal distribution of tissues, and it is an operator-dependent procedure, since special skills are required (as manual dexterity and spirit of observation); at last it needs a coupling gel between the probe and the breast to eliminate the refraction effect of air. Sensitivity: 77%; specificity: 89% [157]. The US, in association with mammography, improves the diagnostic accuracy by increasing the sensitivity (up to 90%) and specificity (up to 98%).

Computed Tomography (CT/TAC): As for the Mammography, uses ionising radiations (X-rays) allowing reproducing sections or layers (tomography) of the patient body and to perform three-dimensional elaborations [102]. It has few benefits in the diagnosis of breast cancer because, although it is in tomographic projection, it does not provide additional meaningful information to the common mammography (RX planar) increasing only the dose of ionising radiations and the complexity of the acquisition procedure.

Nuclear Medicine (PET): In these investigation tools, all the diagnostic instruments for images that use a radio-pharmaceutical are collected. The radio-pharmaceuticals are formed by a radio-isotope tracer with a short half-life, chemically bound to a biologically active molecule, called ‘vector’, that indicates tissue metabolic activity. After a waiting period, during which the metabolically active molecule (usually a sugar) reaches a specified concentration inside the organic tissue to be analysed, the isotope (with short average life) decays, emitting a

positron. After a path that can reach a maximum of few millimetres, the positron annihilates with an electron, producing a pair of gamma photons both of 511 KeV of energy emitted in opposite directions (back to back photons) [36]. PET provides physiological information, unlike all other diagnostic tools that provide morphological information of the anatomical region under examination. The survey instruments offered by nuclear medicine are often recommended for the purpose of diagnosing and staging metastases or discover the involved lymph nodes. The power of radio-tracer, in fact, differentiating the metabolic activity of the cells, allows reaching a sensitivity of almost 100% and a specificity of 98% in the evaluation of lymph nodes and in the search for metastases [272].

Magnetic Resonance (MRI): Based on the physical principles of nuclear magnetic resonance, through the use of electromagnetic fields and radio frequencies, allows generating tomographic images (multi-layer) of tissues reconstructing a digital volume at three dimensions of the organ under examination. It is highly suitable for the investigation of lesions with strong neo-angiogenesis (the ability of a tissue to release VEGF growth factors that stimulate the proliferation of new blood vessels) and thanks to this prerogative MRI is widely used in the diagnosis of breast cancer even if it has contraindications related to long (about 40 minutes) capture process causing discomfort at patients for claustrophobic, or also other problems such as allergic to contrast media, pacemaker, ferromagnetic implants and extreme obesity. Sensitivity: 94%-100%; specificity: 75%-89% [27, 129, 130, 157, 197].

Dynamic Contrast-Enhanced Magnetic Resonance Imaging (DCE-MRI), due to its high sensitivity, has the greatest potential in screening high-risk women for breast cancer, in staging newly diagnoses patients and in assessing therapy effects. Some basis of Magnetic Resonance Imaging and dynamic contrast enhancing by contrast media are presented in the following Sections.

1.2.2 Magnetic Resonance Imaging (MRI)

The principle of nuclear magnetic resonance is based on measurement of the precession of the spin of protons (or other nuclei with a magnetic moment as shown in fig.1.3) when they are subjected to a magnetic field. In conventional MRI the energy acceptor system is represented by hydrogen nucleus (H), the simplest and the most copious element in the human body, characterised by a not zero spin quantum number (spin $1/2$).

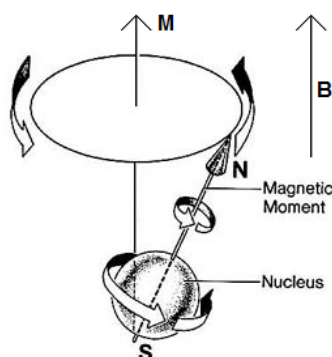


Figure 1.3: Magnetic moment and precession of a proton with spin.

The MRI device consists of a big main magnet capable of generating a static homogeneous magnetic field (B) whose intensity varies, depending on the application cases and of quality requirements, from 0.1T in 10T reaching almost 20T in the experimental applications (The first version of an MRI in Figure 1.4).

The magnetic fields are generated through the use of:

- **Permanent magnets:** Have a limited intensity and cannot be turned off, raising questions about safety and maintenance;
- **Resistive electromagnets:** Made of copper solenoids with a low constructive cost but high cost of use;

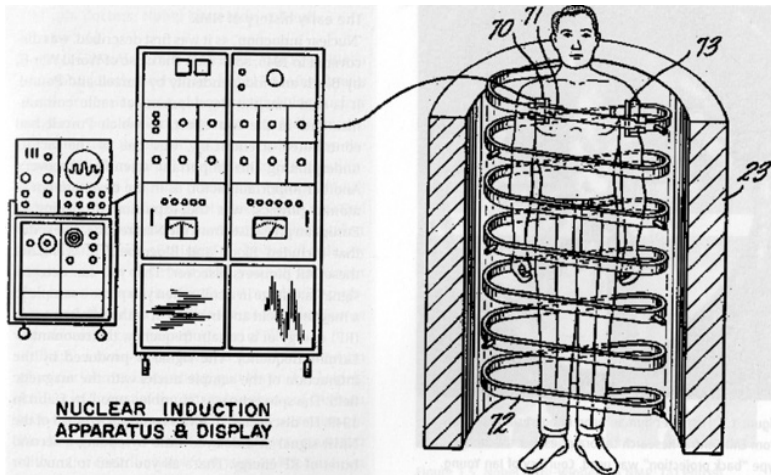


Figure 1.4: Raymond Damadian's: first 'Apparatus and method for detecting cancer in tissue.' [45]

- **Superconducting electromagnets:** Are the most common and consist of a solenoid made of a super-conductive material which, cooled with helium at a temperature of 4°K to reducing their electrical resistance, allow a more applicable cost.

Surrounded by the static magnetic field (B) generated by the main magnet, the spins of the protons inside the tissues tend to be aligned the lines of force (in parallel or anti-parallel way); because the spins that are aligned in parallel direction are in greater number, the tissue will possess a light total magnetisation (M). This alignment is never total, but rather the spins of the various protons begin to show a precession (fig.1.3) around the direction of the magnetic field.

This precession movement follows a specific frequency (Larmor frequency), typical of the atoms to be inspected and tuned to the magnetic field. In the condition of a 1T magnetic field and for the hydrogen atoms, the Larmor frequency is 42.6 MHz. Therefore, if a rotating magnetic field is applied to the patient and if it has the same Larmor frequency and sufficient energy it is possible to rotate the magnetisation of the protons of an arbitrary angle (said

flip-angle). This rotation of the main magnetisation vector occurs because of the physical principle of resonance (that naming the imaging technique).

After the impulse, the spins of the protons will gradually tend to return to their initial alignment along the field (relaxation phenomenon); the trend of the magnetisation is measured through a receiver coil in the plane perpendicular to the main magnetic field (this signal is called Free Induction Decay, or FID). That relaxation occurs with two separate time constants:

T_1 indicates the rate at which (how quickly) is reconstructed the magnetisation vector along the direction of the main field, and it depends on the interaction between protons and the surrounding molecules (spin-lattice relaxation);

T_2 indicates the rate at which (how quickly) is destroyed the component of transverse magnetisation in ideal conditions, and it depends on the mutual interaction of protons neighbours (spin-spin relaxation).

The generation of images occurs through the repeated acquisition of FID signals coming from the body and the appropriate modulation using the gradient coils (Fig. 1.5). Each voxel (Volumetric pixels, equivalent to a pixel in space in three dimensions) of the image has a frequency and a different phase respect to all the others, in this way it is possible to separate the signals coming from a single portion of tissue. The final image is achieved through instruments and elaborations such as filters in frequency (to highlight one Larmor frequency and therefore a single slice) and Fourier Transformations (to decompose the signal in *module* and *phase* just coded to represent the remaining two sizes).

The peculiarity of magnetic resonance imaging, compared to other imaging techniques, is the ability to produce images that reflect different physical properties depending on the type of acquisition sequence used. The classic sequences are:

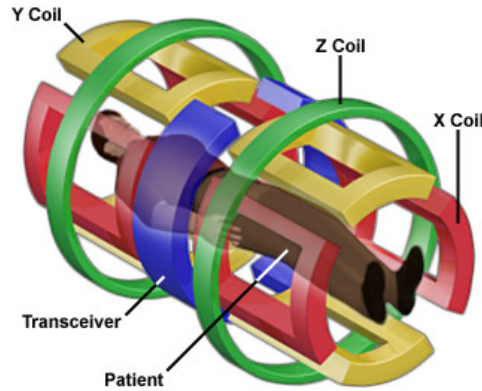


Figure 1.5: MRI Scanner Gradient Magnets.

Proton Density (PD): estimates the number of H protons in resonance per unit of the tissue (voxel) directly calculated by the amplitude of the FID signal;

T_1 weighed: higher brightness of the voxel indicates a short T_1 , typical of the tissue with a small molecular structure useful to highlights breast parenchyma or adipose tissue;

T_2 weighed: higher brightness of the voxel indicates a long T_2 and then highlights tissues containing water such as, for example, cyst.

Fat-suppression techniques [47, 49, 158] could also be used to suppress the signal from adipose tissue. It can be applied to both T_1 and T_2 weighted sequences and exploits the short relaxation times of fat tissue. Fat suppression can be achieved in some different ways [47, 49]:

- Difference in resonance frequency with water by means of frequency selective pulses (CHESS);
- Phase contrast techniques;
- short T_1 relaxation time by means of inversion recovery sequences (STIR technique);

- Hybrid techniques combining several of these fat suppression approaches such as SPIR (spectral presaturation with inversion recovery).

Dynamic Contrast-Enhanced MRI

One of the cellular mutations induced by tumours is the ability to generate new blood vessels with the aim to bring oxygen and nutrient factors to the tumour cells themselves (fig.1.6); this mutation, called neo-angiogenesis, is common to all types of cancer and it is supported by growth factors produced by the tumour cells themselves (VEGF growth factor).

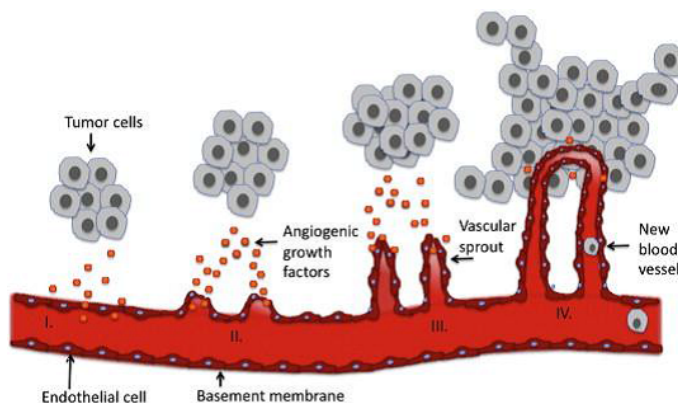


Figure 1.6: Neo-angiogenesis process induced by a malignant lesion.

With the aim to highlight this behaviour, DCE-MRI imaging involves the use of para-magnetic or super-para-magnetic contrast media which affects the information of the image, i.e. by altering the magnetic properties of the sensitive nucleus present in the tissue under examination (altering the relaxation times T_1 and T_2). The contrast agents are injected intravenously, and the most used are:

- Gadolinium (Gd-DTPA), which has the largest number of unpaired electrons and so the greater degree of para-magnetism;

- Iron Oxide particles (super-para-magnetic) whose effect is performed mainly on the T_2 relaxation time.

The contrast medium, circulating in the venous system, spreads with different speed in function of the tissue vascularisation and, just because of the tumour properties of neo-angiogenesis, allows to highlight the damaged tissue with respect to the surrounding healthy tissue.

Then, a complete DCE-MRI study consists of MRI images taken before (pre-contrast series) and after (post-contrast series) an intravenous injection of a contrast media (such as Gadolinium-based paramagnetic contrast agent).

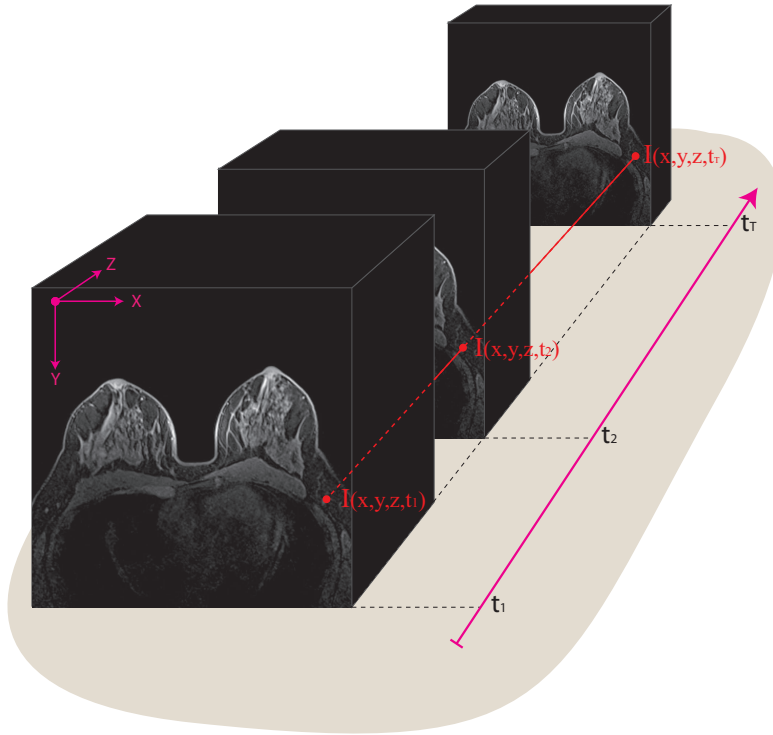


Figure 1.7: Structure of a DCE-MRI. The four dimensions (3 spatial + 1 temporal) of a complete dynamic study.

Experimental studies have shown that the intensity of the signal in time $SI(t)$ in the case of T_1 weighing well approximates the level of concentration

of contrast medium in time [230]. Studying the evolution of the time of the FID signal can be obtained a fourth dimension that, fixed a voxels (and then the 3 remaining dimensions), describes the trend, over time, of the effects of the contrast medium at that exact point in the tissue under examination (fig. 1.7). This curve is called Time Intensity Curve (TIC) or Enhancement Curve.

A visual diagnosis can be obtained by analysing the trend of the enhancement curve and comparing it to sample curves (fig. 1.8) typical of particular tumour formation or that they approximate the dynamics of the blood flow typical of neoplastic lesions [131].

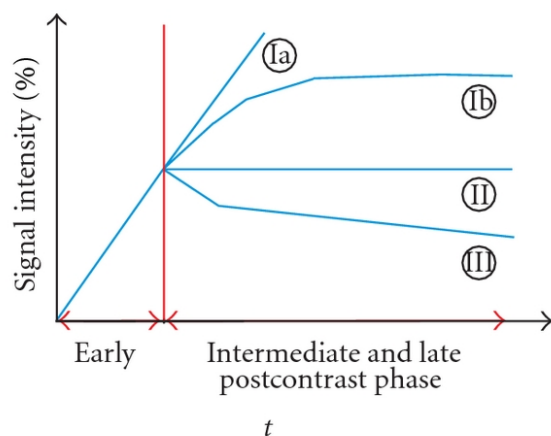


Figure 1.8: Guidelines for visual analysis of TIC curves.

The sample curves, shown in the graph, are considered guidelines for the visual interpretation of TIC and they can be divided [131]:

Type I: corresponds to a straight (Ia) or curved (Ib) line; enhancement (hence the contrast absorption) continues over the entire dynamic study [typical of healthy tissue or benign neoplasms];

Type II: a plateau curve with a sharp bend after the initial upstroke [typical of probably malignant lesions];

Type III: a washout time course [typical of malignant lesions].

1.3 Analysis of DCE-MRI for Breast Cancer

The common screening programs, based on use of mammography as a primary method of investigation, strongly suggest the use of ‘double reading’ (repeated assessment several times by the same radiologist or by different radiologists) with possible discussion among radiologists or, in the case of divergent opinions, the opinion of a third radiologist.

The overall assessment of breast cancer using imaging tools is the result of a process that at first passes through a visual analysis and then through subjective opinion; so the human error can occur, both in the visual analysis and in the last stage of subjective opinion.

In 1987 Nodine and Kundel [185], studying the movement of the eyes of five radiologists during the study of chest x-ray searching for lung cancer (very similar in morphology to breast cancer), showed that the reading process is organized and selective, mainly focused on the regions of the image that the physician considers the most information-rich: eye movement was neither comprehensive nor systematic and, at the end of the inspection of the image, some areas have never crossed from the look of the doctor. At the end of the study, the authors proposed a system of classification of errors divided into three categories:

Sampling Errors: occur when the lesion does not fall within the field of view of the radiologist;

Recognition Errors: occur when the lesion is crossed by the look of the doctor but is not recognised as such;

Decision-Making Errors: occur when a suspicious area is localised, but misclassified.

If we consider more complex diagnostic instruments such as DCE-MRI, object of this thesis, we should add that the search area is not a single two-dimensional image but a three-dimensional volume containing, for instance, 256 pixels * 128 pixels * 80 pixels for a total of about three million of voxels; we should also add that the information contained in the dynamic evolution of the contrast medium is an important decision parameter in the evaluation of neoplastic lesions.

Nowadays, radiologists make often use of tools that assist in the detection of cancerous lesions till also to the evaluation of a complete diagnosis [79, 87]: these instruments are known as Computer-Aided Detection and Diagnosis (CAD) and, supported by an appropriate and proved medical validity, are widely used in the analysis of complex medical investigations both for the extension of data to be taken into account (MRI\TAC\PET) and for an intrinsic uncertainty of the data due to the scanning process (US).

CAD systems analyse data through strict mathematical patterns, according to well-defined and deterministic algorithms. This feature allows to remove the difficulties due to intra-observability and inter-observability, represented by different valuations of the same region, under the same assumptions, by the same doctor on different moments, and different evaluations of the same region by different doctors. Math features behind the deductions (both in detection phase and in diagnosis phase) let to evaluate sensitivity and specificity of such instruments in a precise and strict way showing objective improvement in these parameters [25, 66].

1.3.1 Computer-Aided Detection and Diagnosis

A CAD system, essentially, is composed of a set of waterfall performed independent stages; implemented steps are congruent to the purposes of the system that can range from a simple support to the doctor by providing useful instruments and information, to a more complex automatism for the final classification of lesions into benignant or malignant.

The majority of the CAD proposals in literature follows a common schematic where same preprocessing stages are needed to prepare the data for the core of the CAD, according to the required final functionality. The first approach to CAD design was proposed in [35] for automatic masses segmentation and classification in mammography. With some easy adjustments, DCE-MRI data could be treated with the same approach (Figure 1.9).

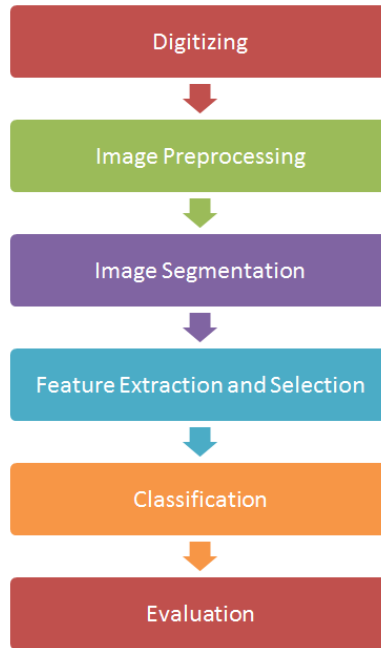


Figure 1.9: The first approach to CAD design. The proposal of [35] was designed for detection and classification of masses in mammography but can be easily applied to DCE-MRI.

It is worth to note that the last stage of Evaluation is not to be intended as a CAD step but as a stage where the performances of the whole CAD are evaluated and considered for further improvements of the CAD itself. There is no need that all the stages are implemented in order to classify a system as a CAD; in fact, there are very simple tools that implement only the early stages of the classification flow, but that provide important and often crucial

support in the final diagnosis. These support instruments, in the case of the study of a DCE-MRI breast, can implement: representations into different projection, three-dimensional reproductions of the scanned volume, temporal representation of the evolution of the dynamic signal (TIC) of a single Voxel or of a set of Voxel (average TIC), subtractive images, segmentation by thresholding, contrast adjustment and interpolation.

Each step of the proposed approach for CAD is now analysed in the following Subsections.

Digitizing

Instruments of modern diagnostic investigation are mainly electronic devices that produce a raw data that can be directly subject of the CAD elaboration. One of the few diagnostic method still on an analogical support is mammography. It is gradually shifting toward digitisation with indications of modern screening programs [69]. The digital imaging systems require the use of a standard format such as the DICOM format (Digital Imaging and Communications in Medicine). DICOM is a standard for handling, storing, printing, and transmitting information in medical imaging [180]. DICOM differs from some, but not all, data formats because it groups information into data sets. That means that a file of a chest x-ray image, for instance, contains the patient ID within the file, so that the image can never be separated from this information by mistake. Generally, a DICOM data object consists of some attributes, including items such as name, sex, ID, etc., and also one special attribute containing the image pixel data [20, 172].

We see, in table 1.2 that a large part of the data are related to the patient and so there is the need to treat it as confidential and sensitive data. The rest of the data are related to the technical characteristics of the acquisition process and it is important that a CAD system should consider them.

PatientID	MagneticFieldStrength (T)
PatientName	ContrastBolusAgent
PatientSex	EchoTime (TE - ms)
PatientBirthDate	RepetitionTime (TR - ms)
PatientAge	FlipAngle (FA - deg)
PatientWeight	PixelSpacing (mm)
PatientReligiousPreference	PixelSize (mm^2)
AcquisitionDateTime	SliceThickness (mm)
ProtocolName	BitsStored
Modality	HighBit
Manufacturer	BitDepth
Rows (px)	BitsAllocated
Columns (px)	FieldOfView (FoV - mm^2)
SeriesDescription	AcquisitionTime (TA - s)

Table 1.2: Some of the most important fields of DICOM header for magnetic resonance images.

Image Preprocessing

This phase includes a set of preliminary elaborations of the image at a low level with the purpose of improving the quality by reducing noise introduced into the acquisition step or correcting any artefacts due to patient motion. This last requirement is critical if the CAD system is developed for diagnostic tools with a long acquisition time such as the DCE-MRI. The average duration of an acquisition with the use of contrast media is 40–50 minutes and, even though the patient is immobilized in special breast-coils [38, 119], that gather the breast in a more or less rigid way, different artefacts may occur caused by breathing, by the different consistency of the breast tissues or even by the involuntary movements of the patient. So it is necessary to expand this stage by introducing a step of registration (or motion correction) of the sequence

of volumetric images in order to reduce the effect of these motion artefacts [238].

Image registration is a process which permits the transformation of the reference systems of two different images in order to compare them; for medical images, the registration process permits transforming or aligning two images collected in two different time instants or produced by different instruments. There is a large variety of algorithms for achieving image registration [28, 156].

Image Segmentation

Segmentation is the process of subdivision of an image in distinct Regions of Interest (ROI — connected sets of voxels) that are homogeneous compared to a given characteristic [13]. An example of tissue segmentation is presented in the Figure 1.10.

This stage is the most critical because the precision and quality of the segmentation results impact in a direct way on the performance of the next steps; the image segmentation can be achieved at different granularity levels:

- air\breast segmentation;
- parenchyma\adipose\glandular tissue segmentation;
- suspicious masses segmentation (fig. 1.10).

The proposed segmentation techniques can vary from the simplest thresholding segmentation based on signal intensity up to more advanced systems of segmentation by classification based on pattern recognition techniques and supervised learning, applied to a set of features.

Feature Extraction and Selection

With the techniques of feature extraction, the objects (regions identified in the previous phase or individual voxels) are represented by a vector of

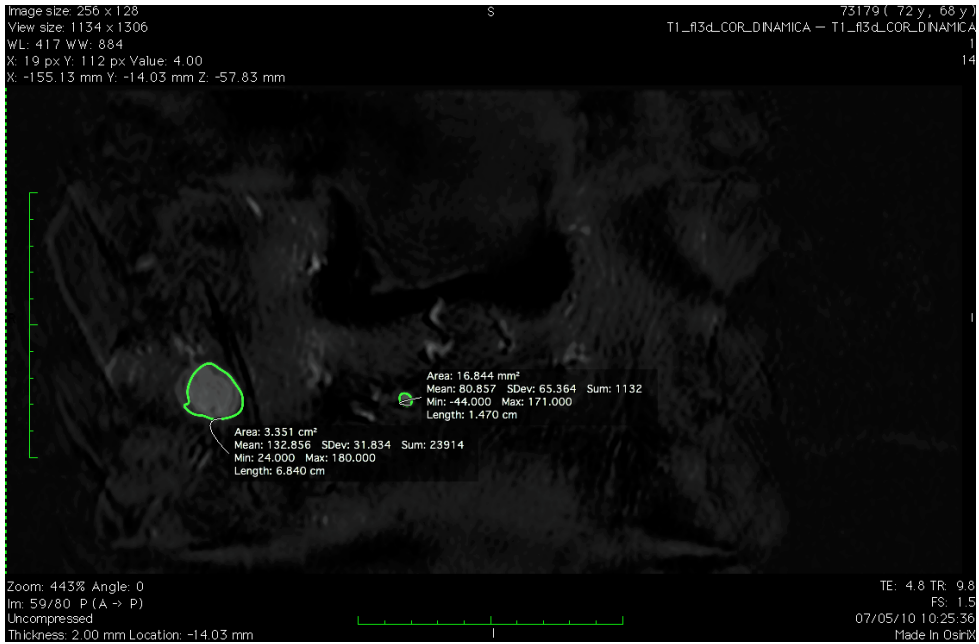


Figure 1.10: A DCE-MRI segmented slice. Two suspicious ROIs have been automatically detected by means of the CAD system.

parameters (feature) that provides a numerical projection of the features that are considered appropriate to describe the problem of classification [75, 243]. We can group the features according to the characteristics that they represent. Five major classes of features have been proposed for classification problems of neoplastic lesions by means of images (Table 1.3).

Feature Class	Symbol	Characterization
Dynamics	DYN	These features quantify the temporal kinetic of the signal by direct model-free measures obtained directly from the time intensity curve (TIC) [2, 19, 48, 74, 142, 171, 246].
Clinico-Pathologic	CLI	These features are directly extracted from the patient records and represent the clinical status and the pathological condition of the patient [254].
Morphological	GEO	With this features are quantified the shape and structure of the Regions Of Interest (ROIs). Malignant lesions may have very particular patterns of shape and specific irregularities on the borders. They can be intended both in two and in three dimensions [19, 166, 231, 248].
Textural	TXT	These features contain a set of measures designed to evaluate the perceived texture of an image on a global or local scale. The measures quantify the variations in the signal intensity, direction or entropy with the aim of discriminating different patterns [9, 31, 40, 46, 76, 96, 240].
PharmacoKinetic	PBPK	According to the Physiological Based PharmacoKinetics Modelling (PBPK), these features describe some physiological parameters (Absorption, Distribution, Metabolism, and Excretion — ADME) of tissues, calculated by mathematical models [26, 71, 73, 100, 224, 227, 241, 242].

Table 1.3: Features type classification and description according to five major classes.

A detailed list of the feature is contained in the following Tables. In particular, the Table 1.4 contains the main Dynamic features; the Table 1.5 contains a list of the main Clinico-Pathologic features; in the Table 1.6 are reported the main Morphological features; Textural features are listed on the Table 1.7; the Table 1.8 reports the main Physiological Based Pharmacokinetics (PBPK) modelling features.

Feature Name	Symbol
Area Under Curve	AUC
normalised AUC	$nAUC$
Relative Enhancement	RE
Relative Enhancement Slope	RES
Maximum of RE	$ReMax$
Basal Signal	BS
Time To Peak	TTP
Perfusion Index	PI
Sum Of intensities Difference	SOD
Wash-In Slope	WIS
Wash-Out Slope	WOS
Signal Enhancement Ratio	SER
Initial Enhancement	IE
Post-Initial Enhancement	PIE
AUC up to TTP	AUC_{TTP}
Contrast Enhancement Image	CEI
Curve Type	CT
Degani Curve Type	DCT
Derivative of Signal Intensity	dSI
Enhancement	E
Enhancement Slope Variance	ES_{var}
Enhancement Standard Deviation	E_{sd}
Maximum Intensity Time Ratio	$MITR$
Percent Enhancement	PE

Table 1.4: Dynamic features list.

Feature Name	Symbol
Race (categorical)	<i>RACE</i>
Age	<i>AGE</i>
Tumour laterality	<i>LAT</i>
Number of involved lymph nodes	<i>#LN</i>
Positivity to Estrogen-Receptor	<i>ER_{pos}</i>
Positivity to Progesterone-Receptor	<i>PR_{pos}</i>
Positivity to Hormone-Receptor	<i>HER2_{pos}</i>
Human epidermal growth factor receptor 2	<i>HR/HER2</i>
pathological Complete Response	<i>pCR</i>
Residual Cancer Burden	<i>RCB</i>
Parental history (categorical)	—

Table 1.5: Clinico-Pathologic features list.

Feature Name	Symbol
Area (2D)	<i>AREA</i>
Volume (3D)	<i>VOL</i>
Radius	<i>RAD</i>
Longest Diameter	<i>LD</i>
Circularity	<i>CIR</i>
Compactness	<i>COM</i>
Perimeter (2D)	<i>PER</i>
Surface (3D)	<i>SURF</i>
Smoothness	<i>SMOTH</i>
Roughness	<i>ROUGH</i>
Eccentricity	<i>ECC</i>
Solidity	<i>SOL</i>
Convexity	<i>CONV</i>

Table 1.6: Morphological features list.

Feature Name	Symbol
1st order gray-level statistics	
— Variance	<i>VAR</i>
— Skewness	<i>SKEW</i>
— Kurtosis	<i>KUR</i>
Gray-Level Co-occurrence Matrix (GLCM)	
— Energy	<i>ENE</i>
— Contrast	<i>GLCM_CONT</i>
— Correlation	<i>CORR</i>
— Homogeneity	<i>HOM</i>
— Variance	<i>VAR</i>
— Sum Average	<i>SUM</i>
— Entropy	<i>ENT</i>
— Dissimilarity	<i>DIS</i>
Gray-Level Run-Length Matrix (GLRLM)	
— Short Run Emphasis	<i>SRE</i>
— Long Run Emphasis	<i>LRE</i>
— Grey-Level Nonuniformity	<i>GLRLM_GLN</i>
— Run-Length Nonuniformity	<i>RLN</i>
— Run Percentage	<i>RP</i>
— Low Grey-Level Run Emphasis	<i>LGRE</i>
— High Gray-Level Run Emphasis	<i>HGRE</i>
— Short Run Low Gray-Level Emphasis	<i>SRLGE</i>
— Short Run High Gray-Level Emphasis	<i>SRHGE</i>
— Long Run Low Gray-Level Emphasis	<i>LRLGE</i>
— Long Run High Gray-Level Emphasis	<i>LRHGE</i>
— Gray-Level Variance	<i>GLRLM_GLV</i>
— Run-Length Variance	<i>RLV</i>
Gray-Level Size Zone Matrix (GLSZM)	
— Small Zone Emphasis	<i>SZE</i>
— Large Zone Emphasis	<i>LZE</i>
— Gray-Level Nonuniformity	<i>GLSZM_GLN</i>
— Zone-Size Nonuniformity	<i>ZSN</i>
— Zone Percentage	<i>ZP</i>
— Low Gray-Level Zone Emphasis	<i>LGZE</i>
— High Gray-Level Zone Emphasis	<i>HGZE</i>
— Small Zone Low Gray-Level Emphasis	<i>SZLGE</i>
— Small Zone High Gray-Level Emphasis	<i>SZHGE</i>
— Large Zone Low Gray-Level Emphasis	<i>LZLGE</i>
— Large Zone High Gray-Level Emphasis	<i>LZHGE</i>
— Gray-Level Variance	<i>GLSZM_GLV</i>
— Zone-Size Variance	<i>ZSV</i>
Neighbourhood Gray-Tone Difference Matrix (NGTDM)	
— Coarseness	<i>COA</i>
— Contrast	<i>NGTDM_CONT</i>
— Busyness	<i>BUSY</i>
— Complexity	<i>COMP</i>
— Strength	<i>STRN</i>

Table 1.7: Textural features list.

Feature Name	Symbol
Transfer constant or permeability surface area	K^{trans}
Efflux rate	k_{ep}
Extracellular Extra-vascular Space (EES) volume fraction	v_e
Blood plasma volume fraction	v_p
Permeability Flux	P_f
Capillary Transit Time	CTT

Table 1.8: Physiological Based Pharmacokinetics Modelling features list.

Depending on the classifiers used and on the purpose of the CAD system, the features can be combined with each other to provide the information required. Then, among all the candidate features, it is necessary to extract a small subset obtained through a phase of feature selection [91] in order to reduce the correlation between the features and remove those that do not provide decisive information in the classification step. Another aim of feature selection is to improve the performance of classifiers strongly influenced by the amount of inputs (Hughes Phenomenon [110], the curse of dimensionality, over-fitting and computational complexity).

Classification

In this step, the CAD system collects the information provided by the previous steps and expresses, for each element (voxel or ROI and related features), a classification by associating to each object a percentage that represents the affinity of that object in any given class. The final decision is directly taken according to the affinity with the classes. CAD systems could use different types of classifiers. In the case of supervised classification techniques, a training step is required before to be inserted in the operating flow of the CAD. The training phase aims to tune the parameters of the mathematical model to the specific problem, trying to maximising the prediction ability and, especially, the generalisation capability [222].

This stage should be considered on a general level as a stage of classification for each of the proposal in the CAD. Indeed, the most of our module proposals in this thesis require a classification stage after a suitable pre-processing and a feature extraction phase.

There are several approaches to classification, each with its own peculiarities, which make it more or less suitable in specific matters. The theory of classification states that there is not best classifier, that behaves better than the others.

To achieve a complete and fair evaluation, in the classification stage the contribution of different classification models needs to be taken into account. Then the following classifier will be applied and compared.

Multilayer Perceptron (MLP) is a feed-forward artificial neural network model that maps sets of input data onto a set of appropriate outputs [57]. An MLP consists of multiple layers of nodes in a directed graph, with each layer fully connected to the next one. Except for the input nodes, each node is a neuron (or processing element) with a non-linear activation function [216]. MLP uses a supervised learning technique called back-propagation for training the network [220, 221].

Decision Tree (DT) is a flow-chart like structure in which internal node represents a test on an attribute\feature, each branch represents the outcome of the test and each leaf node represents class label (decision taken after computing all attributes). A path from the root to a leaf represents classification rule. This flow-chart is used as a predictive model in statistics, data mining, and machine learning [212]. Training a Decision Tree is through greedy algorithms with a process of ‘top-down induction of decision trees’ (TDIDT) [207].

Naive Bayes (NB) is a classifier based on the application of Bayes’ theorem. It requires knowledge of *a priori* probabilities and the conditional probabilities related to the problem that, in the case of medical diagnoses, are not available because of the variability of data (physiological heterogeneity of patients, morphological heterogeneity of patients and variety of pathologies) [57, 222].

Support vector machines (SVM) this classifier constructs a hyper-plane (or set of hyper-planes) in a high-dimensional space, which can be used for classification tasks. Intuitively, a good separation (binary thresholding) is achieved by the hyper-plane that has the largest distance to the nearest training data point of any class [43].

Random Forest (RF) is an ensemble learning method for classification that operates by constructing a multitude of decision trees at training time and outputting the class according to a voting module combining all the output fed by each tree [24].

Adaptive Boosting (AdaBoost) is an ensemble learning meta-algorithm and it can be used in conjunction with many other learning algorithms to improve their performances [57, 70]. AdaBoost is adaptive: it means that subsequent classifiers built are tweaked in favour of those instances misclassified by previous classifiers. AdaBoost is sensitive to noisy data and outliers [222].

All the classifier are implemented in Java using Weka [265] and LibSVM [33] (where needed).

More details about the evaluation of each proposal in the CAD will be given in the result Section 4.2.

Evaluation

This step should not be intended as a CAD step but as a stage where the performances of the whole CAD are evaluated and considered for further improvements of the CAD itself.

The results of the classification are taken into account with the aim of evaluating the final performance of whole diagnosis\ detection system. For this purpose, in the design phase of the CAD, the so-called ‘gold-standard’ or ‘ground-truth’ is taken into account. The ground-truth, regardless of the aim of the system, represents the objective function of an optimisation and reducing errors process. For segmentation and\or classification of tumour lesions, the gold standard is achieved from the medical reports provided by expert radiologists. They consist of segmented ROIs, histopathologic reports and final diagnosis.

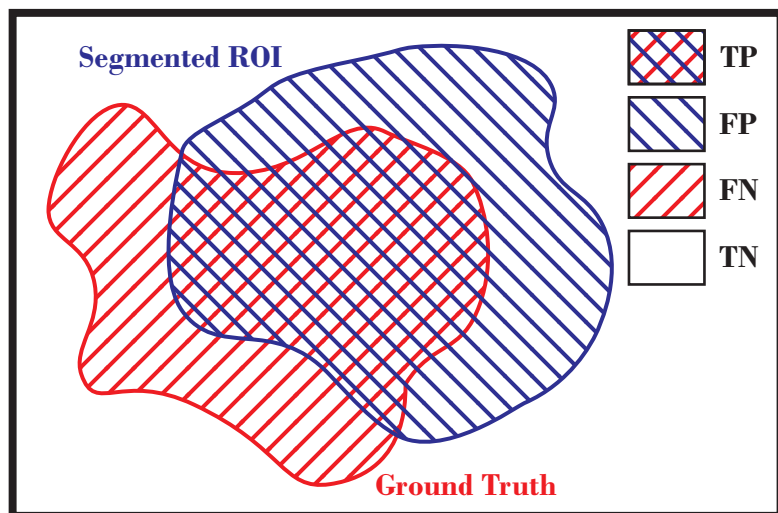


Figure 1.11: Overlap of a Segmented ROI mask with the ground-truth (for the 2D case).

According to the illustration in Figure 1.11 the following definitions are possible:

True Positive (TP) the number of elements belonging to the Positive class, classified by the system as belonging to the Positive class;

True Negative (TN) the number of elements belonging to the Negative class, classified by the system as belonging to the Negative class;

False Positive (FP) the number of elements belonging to the Negative class, classified by the system as belonging to the Positive class;

False Negative (FN) the number of elements belonging to the Positive class, classified by the system as belonging to the Negative class.

In the detection of neoplastic lesions, the most severe case is represented by the false negatives. This misclassification causes a delay in the diagnosis and so in the treatment of the disease and it can irremediably compromise

the patient's health. Instead, the false positives are tolerated (if not excessive in numbers) because they make to start the diagnostic investigation in the same way as true positives do; further clinical examinations will ensure (or exclude) the pathology identified from CAD.

More details about the evaluation of each proposal in the CAD will be given in the result Section [4.2](#).

1.3.2 Therapy planning

The result of a CAD is a complete diagnosis about the aggressiveness of lesions. For each patient with a malignant lesion, the best treatment has to be planned according to the disease staging and the patient clinical status. The treatment consists, in the most of the case, in surgery to remove the malignant lesion and to stop the spread of the disease in other locations and tissues. Different kinds of approaches are possible. The more invasive surgery type is the *Mastectomy*, where the whole breast (both the breasts, in more extreme cases) is removed to totally prevent the spread of the disease; for aesthetic purpose only, it is also possible to reconstruct the breast with plastic surgery. A more conservative approach is the *Quadrantectomy*, where a whole quadrant of the breast is removed. Skin also needs to be removed with some evident aesthetic consequence on the breast shape. The aim of surgery on a big area of the breast is to remove some malignant lesions that have not been well detected in the neighbour of the main lesion and to reduce any chances of recurrence. When the cancer is small and well confined, more localise surgery is possible. A *Lumpectomy* consists in the removing of cancerous tissues and all the close neighbourhood. The removed tissues are analysed to verify that the cancerous cells have been totally removed and the borders of the remains are all sane.

To increase the chances of success of all this kind of surgery, a pre-surgery treatment is possible. Neoadjuvant chemotherapy may be used to shrink cancer before surgery and to provide immediate systemic (full-body)

anticancer effects. The effect of this pre-surgery treatment can range from a complete disappearance of detectable cancer to a failure in the neoadjuvant effect. Some CAD or specific techniques (discussed in the next chapter) provide a forecasting of the treatment response for each patient.

The goal of all chemotherapy regimens is to prevent or arrest the systemic spread of disease. Neoadjuvant or preoperative chemotherapy is increasingly used for the treatment of locally advanced breast cancer and enables more breast-conserving surgeries to be performed by shrinking larger tumours [22, 67, 111, 128]. It would be convenient to determine those subjects who are likely to not respond to the treatment so that a modification may be applied as soon as possible, relieving them from potentially unnecessary or toxic treatments. Pathology measurements of residual disease in the breast and the number of positive lymph nodes at the time of surgery are established predictors of patient survival after neoadjuvant chemotherapy [22, 29, 67, 128], but are determined after completion of treatment and cannot be used as early indicators to improve treatment planning. Identifying surrogates that can predict outcome to therapy earlier or more accurately than current methods would be valuable to tailor treatments to individual patients.

Literature Review

In this chapter, a systematic literature review is performed, focusing on the analysis of breast cancer through Dynamic Contrast-Enhanced Magnetic Resonance Imaging (DCE-MRI). In particular, the review has been addressed for each different step: pre-processing, lesion detection, lesion classification and therapy assessment. Each work has been categorised according to the proposed theoretical approach and the used pattern recognition technique.

The research has been performed by means of the following database: PubMed (US National Library of Medicine, <http://ncbi.nlm.nih.gov/pubmed>), Scopus (Elsevier, <http://scopus.com>), Web of Science (Thomson Reuters, <http://apps.webofknowledge.com>), and Google Scholar (<http://scholar.google.it>). The search criteria used to find related works are a combination of the terms in Table 2.1.

The search string is, then, created by selecting a searching term from each column of the table to satisfy the Clinical Domain and the Diagnostic Test constraints and to search the required Specific Task by using one (or more of them) of the words in the last column. Furthermore, all reference lists of the obtained papers were examined for studies not indexed in the electronic databases.

Clinical Domain	Diagnostic Test	Specific Task
Breast Cancer	Contrast Enhanced Magnetic Resonance Image	Breast Segmentation
Breast Lesion	ce-MRI	Pectoralis Muscle
Breast Tumour	Contrast Enhanced Magnetic Resonance	Chest-Wall Detection
	ce-MR	Whole-Breast Segmentation
	Dynamic Contrast Enhanced Magnetic Resonance Imaging	Registration
	Dynamic Contrast Enhanced MRI	CoRegistration
	DCE-MRI	Motion Correction
		Similarity Measure
		Quality Index
		Quality Assessment
		Image Registration
		Lesion Detection
		Lesion Localization
		Lesion Segmentation
		Computer-Aided Detection
		Classification of Curves
		Lesion Classification
		Therapy Assessment
		Response
		Recurrence
		Disease-Free
		Computer-Aided Diagnosis
		CAD

Table 2.1: Search criteria for the literature review. The search string is a combination of terms from each column to satisfy the Clinical Domain, the Diagnostic Test and the Specific Task required.

When needed, the publications will be indicated with the surname of the first author and the year of publication.

By plotting the number of works with respect to the time (Figure 2.1), is evident that in the last two decades, the breast cancer analysis through DCE-MRI has been treated by many authors and there is a growing interest of the scientific community about these topics.

It has been recognised that this problem can be addressed in a pattern recognition framework with the use of suitable features and classifiers. This has prompted, increasingly, the use of semi-automatic or fully automatic systems to facilitate the study of DCE-MRI and support the work of radiologists.

In particular, it is possible to analyse the articles according to the performed task: whole breast segmentation (we will refer to that task as ‘breast

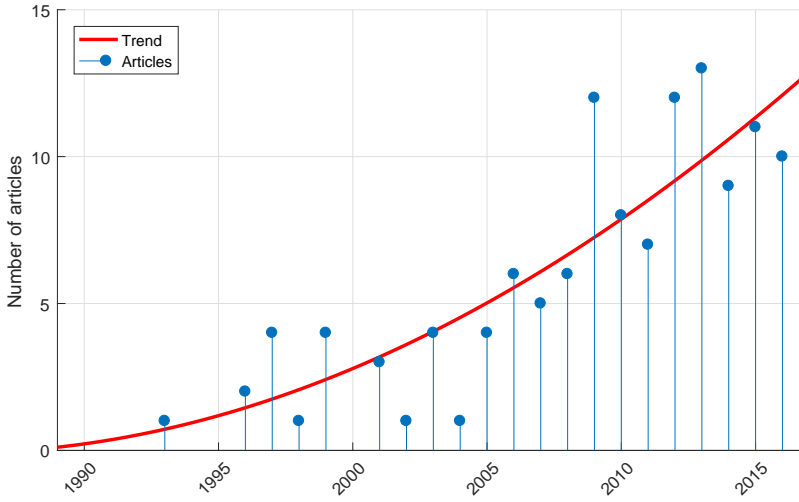


Figure 2.1: Interest of the scientific community. This figure shows the increasing number of articles involving computer-aided breast DCE-MRI analysis versus time. The interest of the scientific community is pretty evident.

mask extraction’); motion correction or image registration; lesion detection; lesion classification; Therapy assessment. Figure 2.2 shows the interest of the analysed literature regarding these CAD tasks.

2.1 Pre-processing

According to the methodologies proposed in this thesis, in the pre-processing phase both the segmentation of the whole breast tissues and the motion correction (also known as co-registration) are included. Then, all the literature proposals about breast segmentation and all the motion correction techniques (or approaches) have been analysed. In addition to the problem of motion correction, it was also analysed the state of the art about techniques for evaluating the results of a co-registration.

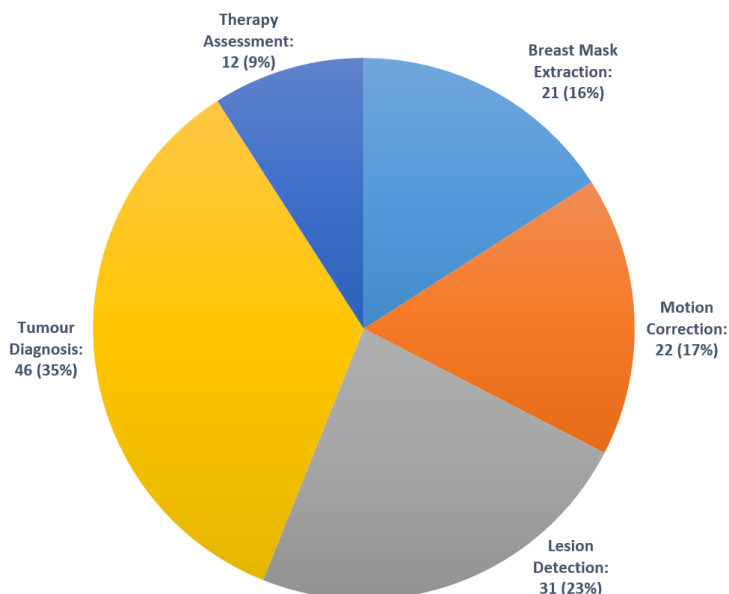


Figure 2.2: Pie-chart of the CAD tasks. This image shows the distribution of the analysed scientific community with respect to each task treated in this thesis.

2.1.1 Breast Mask

The breast mask extraction procedure lies in 3D image segmentation field. The so far published approaches can be completely categorised by using the following classes: Pixel-based, Atlas-based and Geometrical-based.

Pixel-based approaches: A voxel-by-voxel decision, mainly based on signal intensity. Most of this algorithms, in general, starts from an image thresholding to convert the grey-level image to a binary one [215, 252]. Then, some refinements (morphological or more complex operations) are required to improve the final mask [8, 257, 258]. They are easy to implement and do not require any prior information on patient's data but usually produces not very accurate masks.

Atlas-based approaches: Based on a direct comparison between the images (or the volumes) to be segmented and items from an anatomical atlas [68, 88, 90, 188, 251]. They can be used to segment the whole breast or just some anatomical structures [89, 146]. In general, this kind of approaches is very efficient when applied to a heterogeneous set of volumes, but it requires an atlas well representative of the population and of the used acquisition protocol, limiting their application and portability.

Geometrical-based approaches: Starting from a pixel-based segmentation, these approaches refine the mask by means of geometrical considerations (such as matching a deformable model to an image through energy minimization). Exploiting the geometrical considerations, they can obtain a breast mask that follows anatomical and physiological characteristics [78, 100, 148, 151, 174, 267]. They inherit advantages and disadvantages from the pixel-based approaches, usually providing more accurate mask at the cost of a heavier computational and design effort for the geometrical characterization of the human anatomy.

Some relevant approaches for breast mask extraction have been taken into account in this thesis. Vignati et al. [252] propose a pixel-based segmentation approach based on an Otsu's thresholding and morphological refinements post-processing. The obtained breast mask is often over-segmented but always cover the whole breast parenchyma. Goshal et al. [84] face with MRI segmentation by using a more sophisticated pixel-based technique based on a marker-controlled watershed algorithm. As regards the atlas-based techniques, a common criticism of these approaches is that, due to the wide anatomical variability, a limited atlas cannot, usually, correctly segment all types of breast shapes. For this reason, Fooladivanda et al. [68] implement an atlas-based segmentation only for the pectoral muscle, while use a pixel-based approach to detect the breast-air edge. As stated above, geometrical-based approaches try to spot the chest wall basing on geometrical constraints to

force the pectoral muscle segmentation to follow anatomical shapes. With this aim, Lu et al. [151] apply active contour refinements to a roughly extracted pectoral muscle mask and segment the breast by mix obtained results with those obtained by a pixel-based breast-air segmentation. A notable approach was proposed by Wu et al. [267], that uses geometrical considerations to refine the breast-pectoral muscle edge previously located by means of a Canny edge detector. This technique is one of the most effective so far proposed but fails in segmenting lesions lying on the pectoral muscle, since they confuse the edge detector.

In the Table 2.2 have been summarised all the so far approaches.

Papers	Approaches		
	Pixel-based	Atlas-based	Geometrical-based
Alshanbari2015 [8]	•		
Baluwala2015 [14]	•		
Fooladivanda2014 [68]		•	
Giannini2010 [78]			•
Gong2008 [82]		•	
Gubern-Merida2015j [88]		•	
Gubern-Merida2012 [89]		•	
Gubern-Merida2015 [90]		•	
Hayton1997 [100]			•
Kannan2011 [120]	•		
Liang2015 [146]		•	
Lin2013 [148]			•
Lu2006 [151]			•
Mustra2009 [174]			•
Ortiz2012 [188]		•	
Rosado-Toro2015 [215]	•		
Vignati2009 [251]		•	
Vignati2011 [252]	•		
Wang2011 [257]	•		
Wang2012 [258]	•		
Wu2013 [267]			•

Table 2.2: Literature analysis of breast-masking approaches.

2.1.2 Motion Correction

As important pre-processing step, a co-registration is required to improve the next stage results. Therefore, a literature review about the motion correction techniques is performed. In addition, different approaches to the evaluation of motion correction results are also analysed.

Motion Correction Techniques

Motion correction techniques (MCTs) can be categorised on the basis of the type of transformation used to register two images (or volumes). Rigid MCTs exploit affine transformations in order to preserve points, lines, and planes. Limited to the context of breast DCE-MRI, only a few works make use of MCT based on affine transformations [124, 278]. However, these former MCTs might not model adequately the deformation of soft breast parenchyma. Consequently, a ‘non-rigid’ MCT such as a Free-Form Deformation (FFD) transformations have been used [82, 103, 108, 109, 121, 145, 151, 162, 195, 211, 213, 214, 229, 252, 256].

In the literature, it is possible to find software that provide a complete and fully functional images registration toolbox. These software offer several approaches to motion correction, they support different modalities and are highly customisable making them suitable for several contexts. Thanks to their versatility are widely used in the medical context [122, 127, 176, 219].

With the aim to obtain better results, some MCTs introduce elasticity property and non compressibility constraints. These properties are specific of the tissue and lead to a better non-linear co-registration [109, 211, 229]. Moreover, a simulation of soft tissue biomechanics jointly with a pose estimation, improves the precision of the applied FFD transformations [59–61, 95, 104, 106, 116, 170].

Pharmacokinetics approaches could also be used jointly with the MCT. In some cases the time behaviour of the contrast agent helps the motion

correction estimation; in other instances, instead, it is also used to provide a tissue segmentation [103, 108, 100].

Finally, co-registration is frequently used to combine different modality with the aim of exploit information from other studies. In breast DCE-MRI it is usual to perform the co-registration with PET or CT [270, 55], DWI-MRI [169, 92] and mammography (where a free-form deformation is needed to simulate the breast compression in the mammography device) [108, 109, 170, 137].

Even if the need of a motion correction has been widely proved, the majority of the works do not apply any co-registration or motion correction approach. Only 25% of the so far examined literature uses an affine or a FFD MCT to improve the results of DCE-MRI data elaboration (see Table 2.3). It is worth to note that most of the contributions with a MCT has been found in the more recent works.

MCT type	# of articles	% of the literature
None	42	75.0%
Rigid or Affine	4	7.1%
Free-Form Deformation	10	17.9%

Table 2.3: Distribution of MCTs in the literature works.

Table 2.4 summarises all the used approaches in breast analysis by means of DCE-MRI.

Quality Indexes

The simplest and most widely used full-reference quality indexes are the mean squared error (MSE) [132, 239] and the peak signal-to-noise ratio (PSNR) [262]. They are computed by averaging the squared intensity differences of distorted and reference image pixels. These are appealing because they are simple to calculate, have clear physical meanings, and are mathematically convenient in the context of optimisation. However, they are not very well

Papers	Approach
Gong2008 [82]	FFD
Hayton1997 [100]	FFD
Hill2006 [103]	FFD
Hopp2012 [108]	FFD
Hopp2013 [109]	FFD
Kim2011 [121]	FFD
Klein2010 [122]	Toolbox
Krishnan1999 [124]	Rigid
Kroon2009 [127]	Toolbox
Li2009 [145]	FFD
Lu2006 [151]	FFD
Martel2007 [162]	FFD
Myronenko2010 [176]	Toolbox
Periaswamy2003 [195]	FFD
Rohlfing2003 [211]	FFD
Roosgard2012 [213]	FFD
Roosgard2015 [214]	FFD
Rueckert1999 [219]	Toolbox
Schnabel2001 [229]	FFD
Vignati2011 [252]	FFD
Wang2005 [256]	FFD
Zuo1996 [278]	Affine

Table 2.4: Motion Correction Techniques literature review.

matched to perceived visual quality. Moreover, these quality indexes rely on the assumption that the intensities of two images are linearly correlated, which is, in general, not satisfied in the case of multi-modality registration or contrast enhanced medical images.

To overcome these problems, other similarity measures have been proposed such as entropy (E) [234], normalize correlation (nC) [193, 209, 233], mutual information (MI) [42, 149, 154, 205, 233, 235, 253, 264] and normalized mutual information (nMI) [210, 211, 236]. In the medical context,

the last two measures are the most used for well handling the multi-modal co-registration or the motion correction with contrast-enhanced images.

In this thesis, a model-based quality index has been proposed. The Physiologically Based Pharmacokinetic (PBPK) models have been used as the underlying mathematical concept. To the best of our knowledge, no work about similarity measure, which overcomes the contrast-agent effects by considering PBPK modelling, has been published.

2.2 Lesion Detection

Lesion detection is the basis of an automated computer-aided diagnosis technique for the tumour classification in breast DCE-MRI. The next stages, such as tumour classification according to his malignity and the therapy assessment, highly depend on the results of this stage. The more are well detected the lesions the better will be the results of the next stages.

The task has been addressed in several ways. Some works propose a semi-automatic segmentation where a human operator provides a very rough segmentation such as a 2D square or a 3D cuboid. Then an automatic refinement improves the lesion detection using the rough segmentation as a starting point for a more precise final segmentation [168, 231, 238, 259].

The most used descriptors for the lesion segmentation task are the dynamic features (DYN) (already presented in Section 1.3.1).

Since the rough segmentation helps to focus the detection method on a very specific region, the segmentation approaches are very basic. The most of the semi-automatic methods start from very simple dynamic features such as signal intensity or close derivative features such as image differences, ratio or enhancement patterns. So far proposed segmentation methods for semi-automatic approaches are simple binary thresholding [139, 141, 231], or more complex methods such as Fuzzy C-Mean [19, 30, 34, 177, 178] or Graph-Cut [275, 276].

To achieve an automatic lesions segmentation more complex approaches are needed. Moreover, beside of the dynamic features, more specific features are used to accomplish the task automatically (also presented in Section 1.3.1).

Many approaches make use of dynamic features (DYN) [6, 13, 19, 30, 34, 64, 74, 81, 90, 114, 138, 139, 141, 165, 168, 173, 177, 178, 231, 238, 246, 248, 251, 252, 259, 260, 275, 276]; very few works make use of geometrical/morphological features (GEO) [139], textural features (TEX) [98] or pharmacokinetic features (PBPk) [152, 268]. This last two kind of features are mainly used in tumour classification.

The approaches to segmentation and lesion detection can be categorised according to the following division: filtering-based, morphological-based, unsupervised model-based and supervised model-based. In the filtering-based approaches a simple threshold is applied [13, 152, 231, 248, 251, 252]. The morphological-based segmentations make use of geometric based iterative algorithms such as Region Growing [139, 141, 168, 259], Graph-Cut [165, 275, 276] or Active Contours [6, 30]. Usually, they are manually initialised [168, 259, 275, 276]. However, to achieve an automatic segmentation, the seed or the initial region could be directly calculated from an automatically extracted rough segmentation (a filter-based approach [139, 141] or a model-based segmentation [6]). Finally, the model-based approaches could be classified in unsupervised and supervised methods. In the unsupervised methods lie the clustering algorithms such as k-Means [173], Vector Quantization (VQ) [141], Mean Shift [165], Density Based Clustering (DBC) [81] or Fuzzy C-Means (FCM) [19, 30, 34, 114, 138, 177, 178]. The majority of works makes use of supervised model-based methods such as Maximum Likelihood (ML) [238], Maximum a Posteriori (MAP) [238, 268], Linear Discriminant Analysis (LDA) [246], Multilayer Perceptron (MLP) [74], Cellular Neural Network (CNN) [64], AdaBoost [90], Support Vector Machines (SVM) [98, 246, 260] and Hidden Markov Random Field (HMRF) [268].

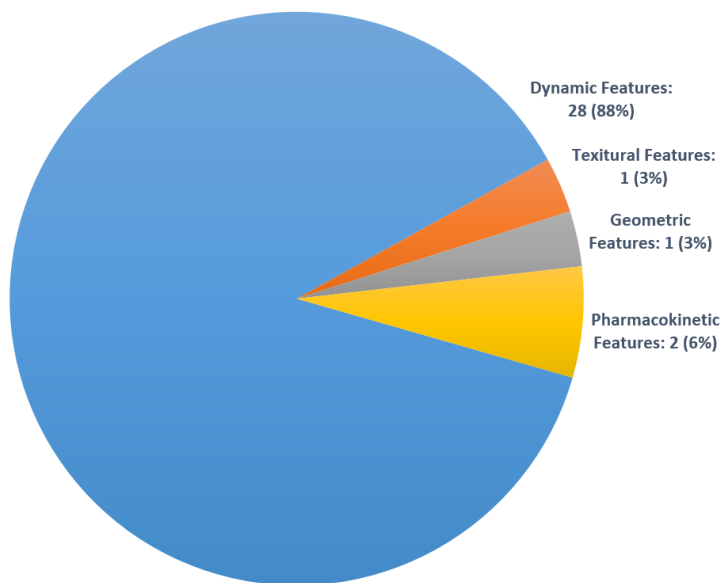
To further improving the final lesion detection result, the segmented regions could be enhanced by means of morphological refinements [13, 34, 248].

A complete report of the works considered for this literature review is in Table 2.5.

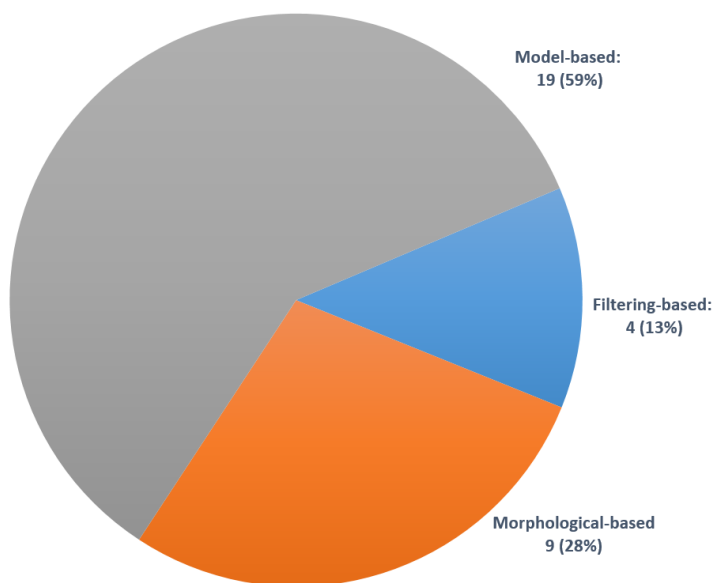
The Figures 2.3 show the distribution of the features and the approaches in the analysed literature.

Papers	Fully Autom.	MCT	Feature Set	Approach
Agner2009 [†] [6]	•		DYN	MODEL, MORPH
Arbach2004 [†] [13]	•		DYN	FILT
Bhooshan2010 [†] [19]			DYN	MODEL
Cai2014 [†] [30]			DYN	MODEL, MORPH
Chen2006 [†] [34]			DYN	MODEL
Ertas2008 [64]	•		DYN	MODEL
Fusco2012 [†] [74]	•		DYN	MODEL
Glaßer2013 [†] [81]	•		DYN	MODEL
Gubern-Merida2015 [90]	•	F	DYN	MODEL
Hassanien2012 [98]	•		TEX	MODEL
Jayender2014 [†] [114]	•		DYN	MODEL
Lee2008 [†] [139]	•		DYN, GEO	FILT, MORPH
Lee2010 [†] [138]	•	R	DYN	MODEL
Leinsinger2006 [†] [141]			DYN	FILT, MORPH
Lucht2002 [†] [152]	•	F	PBPK	FILT
McClymont2014 [165]	•	F	DYN	MODEL, MORPH
Meinel2007 [†] [168]			DYN	MORPH
Moftah2014 [173]	•		DYN	MODEL
Nagarajan2013j [†] [177]	•		DYN	MODEL
Nagarajan2013 [†] [178]			DYN	MODEL
Sinha1997 [†] [231]			DYN	FILT
Tanner2006 [†] [238]		F	DYN	MODEL
Twellmann2008 [247]	•		DYN	MODEL
Tzacheva2003 [†] [248]	•		DYN	FILT
Vignati2009 [251]	•	F	DYN	FILT
Vignati2011 [252]	•	F	DYN	FILT
Wang2013 [260]	•	R	DYN	MODEL
Wang2014 [†] [259]			DYN	MORPH
Xiaohua2005 [268]	•	F	PBPK	MODEL
Zheng2007 [†] [275]			DYN	MORPH
Zheng2009 [†] [276]			DYN	MORPH

Table 2.5: Lesion Detection literature review. For each work is reported the used feature set and the approach category according to the proposed classification of the literature review. MODEL: model-based; FILT: filtering-based; MORPH: morphological-based. Moreover, the presence of a human initialised approach or a fully automated approach for lesion segmentation is highlighted. Finally, for each work, the table reports the typology of the used Motion Correction Technique (MTC) when applicable. R: Rigid; F Free-Form Deformation. [†] indicates a work where lesion detection is part of a wider computer-aided system such as a lesion classification method.



(a)



(b)

Figure 2.3: Pie-charts of the used features (a) and the proposed approaches (b) for the Lesion Detection task in the analysed literature works.

2.3 Tumour Diagnosis

The most of the computer-aided approaches aim to lesion classification. Some of them include an automatic or semi-automatic tumour detection as a basis for the final stage of classification (e.g. in Tab. 2.5, the works with * include lesion detection as well lesion segmentation). Anyway, the starting point of a tumour characterization stage is one or more regions of interest (ROIs), and the output of this module is a binary classification into a benignant or malignant lesion. Some works provide a more precise categorization of the malignant lesions including the classification of different kind of tumours.

Beside of the dynamic features, more complex features are used to accomplish the ROIs classification task (all the features are presented in Section 1.3.1). The most used descriptors for tumour classification still remain are the dynamic features (DYN) [1, 2, 6, 5, 19, 30, 34, 65, 74, 80, 81, 131, 138–143, 152, 153, 167, 168, 179, 181, 231, 237, 238, 247, 248, 250, 254, 259, 271, 275, 276]. The runner up features are the textural (TXT) ones [5, 6, 19, 30, 98, 118, 138, 164, 166, 168, 177, 178, 181, 225, 226, 231, 248, 249, 259, 266, 275, 276]. Then, geometrical features (GEO) help to distinguish between malignant and benignant lesions [5, 6, 19, 30, 74, 80, 81, 107, 139, 166, 168, 181, 226, 231, 238, 248, 254, 259]. Finally, PBPK, even if computational heavy, are used to better describe the tissues [152, 181]. The clinico-pathologic features (CLI) are always used along with the other descriptors [81, 254].

To accomplish the binary ROIs classification into a malignant or benignant lesion, different classifiers have been proposed. The most used approach to classification is the Multilayer Perceptron (MLP) [1, 2, 13, 152, 153, 164, 165, 168, 181, 225, 237, 250, 254, 266]. Support Vector Machine (SVM) always provides best results when compared with other approaches [5, 6, 30, 118, 140, 138, 142, 143, 179, 177, 178, 226, 247]. Moreover, Linear Discriminant Analysis (LDA) is also used for the classification task [19, 80, 107, 231, 249, 275, 276]. Other classifiers have been used such as Bayesian

Classifier (BC) [19, 74, 248, 271], Decision Trees (DT) [74, 81], k-Nearest Neighbours (kNN) [164, 177] and binary Logistic Regression (LR) [238, 259]. Unsupervised approaches have also been tested, such as Fuzzy C-Mean (FCM) [34, 247], Vector Quantisation (VQ) [141] and Principal Component Analysis (PCA) [65]. Finally, more simple approaches by thresholding have been used [131, 139, 167].

Besides classical machine learning techniques, some preliminary deep learning approaches (DEEP) to the lesion diagnostic tasks have been proposed. At the moment, the only ones to apply these techniques in a CAD to DCE-MRI images for cancer diagnosis are Antropova et al [12]. The authors propose to extract slices from DCE-MRI segmented lesions to feed AlexNet [126], a pre-trained Deep Convolutional-Neural-Network (DeepCNN). The output from the last internal layer provides 4096 features used to train a Support Vector Machine (SVM) on the malignant/benignant classification task.

A complete report of the works considered for this literature review is in Tables 2.6 and 2.7.

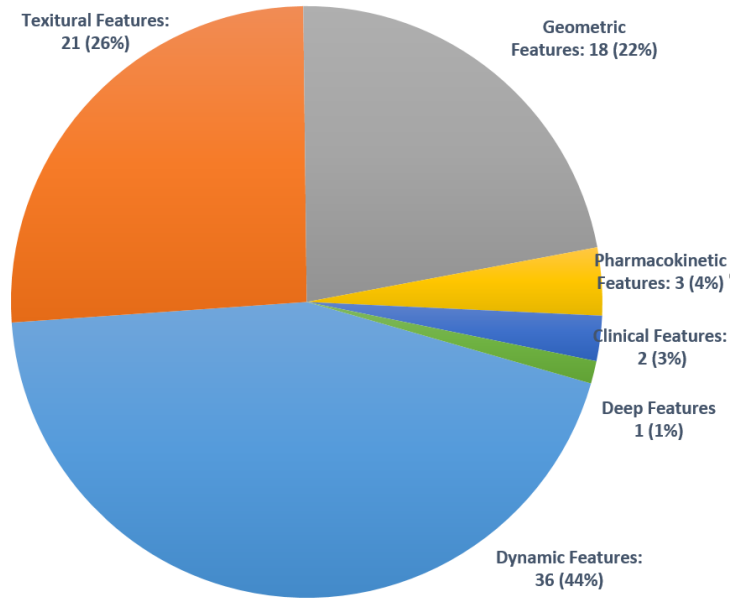
The Figures 2.4 show the distribution of the features and the approaches in the analysed literature.

Papers	MCT	Feature set	Classifier
Abdolmaleki1997 [1]		DYN	MLP
Abdolmaleki2001 [2]		DYN	MLP
Agner2009 [6]		DYN, TXT, GEO	SVM
Agner2011 [5]		DYN, TXT, GEO	SVM
Antropova2016 [12]		DEEP	SVM
Arbach2004 [13]		GEO	MLP
Bhooshan2010 [19]		DYN, TXT, GEO	LDA, BC
Cai2014 [30]		DYN, TXT, GEO	SVM
Chen2006 [34]		DYN	FCM
Eyal2009 [65]		DYN	PCA
Fusco2012 [74]		DYN, GEO	DT, BC
Gilhuijs1998 [80]		DYN, GEO	LDA
Glaßer2013 [81]		DYN, GEO, CLI	DT
Honda2016 [107]		DYN, GEO	QDA
Juntu2010 [118]		TXT	SVM
Kuhl1999 [131]		DYN	Threshold
Lee2008 [139]	R	DYN	Threshold
Lee2009 [140]		DYN	SVM
Lee2010 [138]	R	DYN, TXT	SVM
Leinsinger2006 [141]		DYN	VQ
Levman2008 [142]	F	DYN	SVM
Levman2010 [143]	F	DYN	SVM
Lucht2001 [153]		DYN	MLP
Lucht2002 [152]	F	DYN, PBPK	MLP

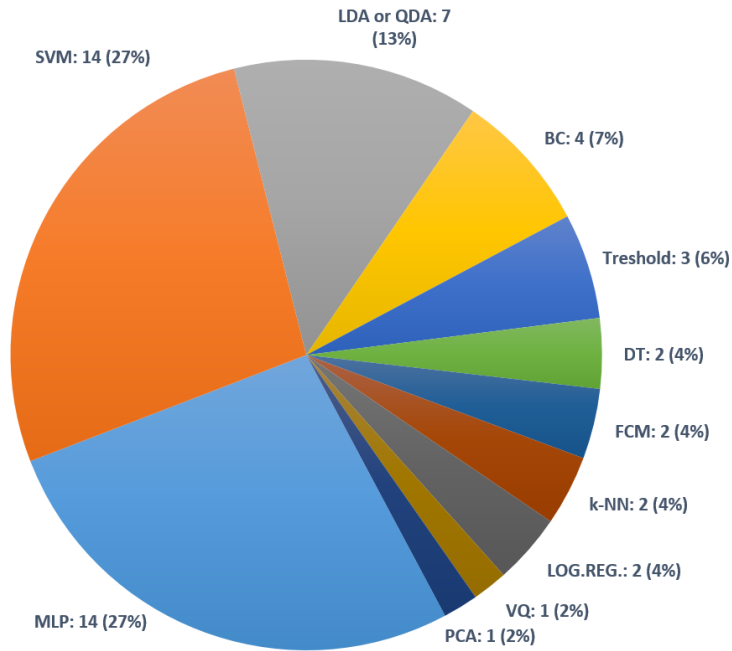
Table 2.6: Tumour Diagnosis literature review (1/2). For each work the used feature set and the approach category according to the proposed classification of the literature review are reported. Moreover, for each work, the table also reports the typology of the used Motion Correction Technique (MTC) when applicable. R: Rigid MCT; F Free-Form Deformation MCT.

Papers	MCT	Feature set	Classifier
Mayerhoefer2008 [164]		TEX	k-NN, MLP
McLaren2009 [166]		TEX, GEO	MLP
Meeuwis2010 [167]		DYN	Threshold
Meinel2007 [168]		DYN, TXT, GEO	MLP
Nagarajan2013j [177]		TEX	k-NN, SVM
Nagarajan2013 [178]		TEX	SVM
Navaei-Lavasani2015 [179]	F	DYN	SVM
Newell2010 [181]		DYN, TXT, GEO, PBPK	MLP
Sathya2013 [225]		TEX	MLP
Sathya2013j [226]		TEX, GEO	SVM
Sinha1997 [231]		DYN, TXT, GEO	LDA
Szabo2004 [237]	F	DYN	MLP
Tanner2006 [238]	F	DYN, GEO	LOG.REG.
Twellmann2008 [247]		DYN	FCM, SVM
Tzacheva2003 [248]		DYN, TXT, GEO	BC
Tzalavra2016 [249]		TEX	LDA
Vergnaghi2001 [250]		DYN	MLP
Vomweg2003 [254]		DYN, GEO, CLI	MLP
Wang2014 [259]		DYN, TXT, GEO, PBPK	LOG.REG.
Woods2007 [266]		TEX	MLP
Yang2014 [271]	R	DYN	BC
Zheng2007 [275]		DYN, TXT	LDA
Zheng2009 [276]		DYN, TXT	LDA

Table 2.7: Tumour Diagnosis literature review (2/2). For each work the used feature set and the approach category according to the proposed classification of the literature review are reported. Moreover, for each work, the table also reports the typology of the used Motion Correction Technique (MTC) when applicable. R: Rigid MCT; F Free-Form Deformation MCT.



(a)



(b)

Figure 2.4: Pie-charts of the used features (a) and the proposed approach (b) for the Tumour Diagnosis task in the analysed literature works.

2.4 Therapy Assessment

After a malignant breast cancer detection, therapy should be applied. For women with operable breast cancer, neoadjuvant chemotherapy (chemotherapy before surgery) may be used to shrink cancer before surgery and to provide immediate systemic (full-body) anticancer effects.

Some women who receive neoadjuvant chemotherapy will experience a complete disappearance of detectable cancer (a complete response). In these women, the risk of cancer recurrence following breast-conserving surgery has not been well defined. Women who undergo breast-conserving surgery after a complete response to neoadjuvant chemotherapy have a low risk of local or regional cancer recurrence (cancer recurrence in the area of the breast) [77, 97].

To assess the risk of local or regional cancer recurrence, researchers conducted several studies on the statistical connection between the kind of surgery and the recurrence of the tumour. Women underwent segmental Mastectomy (a type of breast-conserving surgery), Quadrantectomy or Lumpectomy, have a low risk of local or regional cancer recurrence. Most of the results conclude that risk of local or regional cancer recurrence is low among women who undergo breast-conserving surgery following a complete response to neoadjuvant chemotherapy [192].

For this reason most of the works about therapy assessment focus on the prediction of the pathological Complete Response (pCR) [115, 56, 3, 203].

In this thesis, the therapy assessment module has the disease-free recurrence prediction as the final goal. For each patient, a binary result about the recurrence of the primary tumour is produced.

To accomplish this kind of prediction, most of the literature proposals rely on dynamic (DYN) [37, 63, 112, 113, 144, 204, 202, 206, 245] or morphological (GEO) features [63, 117, 144, 183, 191, 204, 202, 206]. As dynamic features, percent enhancement (PE) and signal enhancement ratio (SER) have received particular attention for having a close relationship with the commonly

analysed pharmacokinetic parameter: the redistribution rate constant (k_{ep}). Within the morphological features (GEO), functional tumour volume (FTV), computed by voxels counting using enhancement thresholds, and change from baseline (Δ FTV) was often used. More accurate techniques make use of clinicopathologic (CLI) information [37, 63, 204] and Physiologically Based Pharmacokinetic features (PBPk) [63, 204].

A complete report of the works considered for this literature review is in Table 2.8.

Papers	Feature set
Choi2016 [37]	DYN, CLI
El-nasr2016 [63]	DYN, GEO, CLI, PBPk
Hylton2016 [112]	GEO
Jafri2014 [113]	DYN
Jones2013 [117]	GEO
Li2008 [144]	DYN, GEO
Newitt2011 [183]	GEO
Partridge2005 [191]	GEO
Pickles2009 [204]	DYN, GEO, CLI, PBPk
Pickles2016 [202]	DYN, TEX, GEO
Preda2006 [206]	DYN, GEO
Tuncbilek2012 [245]	DYN

Table 2.8: Literature analysis of therapy assessment approaches for recurrence prediction.

The Figure 2.5 shows the distribution of the features in the analysed literature.

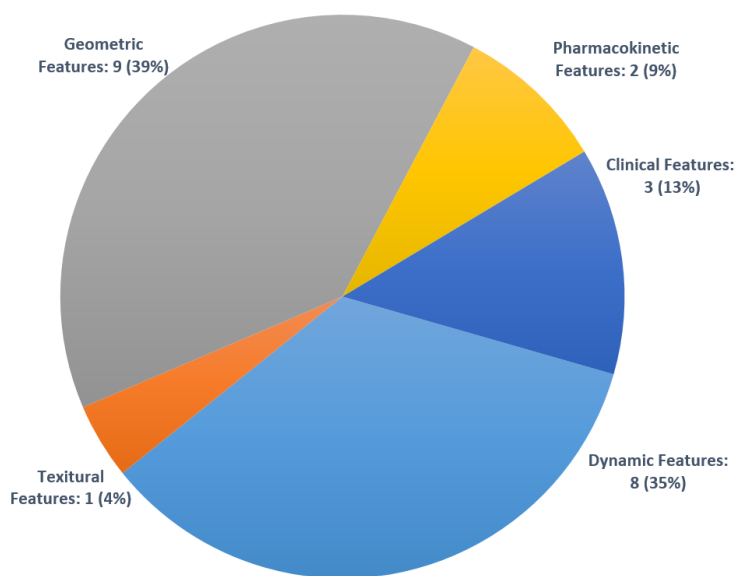


Figure 2.5: Pie-chart of the features used for the Therapy Assessment in the analysed literature works.

2.5 Datasets

The biomedical domain strongly relies on the data availability. Many specific fields suffer from lack of public data, and many researchers are able to produce reliable publication only because of private collaborations with medical structures.

Some causes of this lack of data could be found in the presence of personal information in the medical records and into the patient's data (mostly in the presence of tumour findings). Another possible cause of this non-disclosure of information could be connected to the frenetic activity of a very practical environment such as clinics and medical environments. The production of reliable and well-structured public data for research purposes requires much effort and much time not always available to physicians or radiologists.

A total of 145 papers has been analysed to produce a reliable literature review of the topics of that thesis. For each paper, all the information about the dataset (where available) have been extracted and structured in Table [2.9](#). Subsequently, some observations have been carried out from the table.

Papers	Type of Images	# Patients
Abdolmaleki1997 [1]	T1	156
Abdolmaleki2001 [2]	T1/T2	120
Agner2009 [6]	T1	41 [†]
Alshanbari2015 [8]	T1	20
Arbach2004 [13]	T1/T2	20
Baluwala2015 [14]	T1	50
Cai2014 [30]	T1	234
Chen2006 [34]	T1	121
Choi2016 [37]	T1	602
El-nasr2016 [63]	T1	60
Ertas2008 [64]	T1	19
Eyal2009 [65]	T1	65
Fooladivanda2014 [68]	T1	60
Fusco2012 [74]	T1	38
Giannini2010 [78]	T1	31
Gilhuijs1998 [80]	T1	27
Glaßer2013 [81]	T1	50
Gong2008 [82]	T1	40
Gubern-Merida2012 [89]	T1	27 [†]
Gubern-Merida2015 [90]	T1	126
Honda2016 [107]	T1 fat-sup.	90
Hopp2012 [108]	T1	11
Hopp2013 [109]	T1	78
Jafri2014 [113]	T1 fat-sup.	64
Jayender2014 [114]	T1	24
Juntu2010 [118]	T1	135
Kuhl1999 [131]	T1	205
Lee2008 [139]	T1	24
Lee2009 [140]	T1	20
Lee2010 [138]	T1	171
Leinsinger2006 [141]	T1	88
Levman2008 [142]	T1	94
Levman2010 [143]	T1	259
Li2009 [145]	T1	1
Lin2013 [148]	T1	31
Lu2006 [151]	T1	33
Lucht2001 [153]	T1	264
Lucht2002 [152]	T1	15

Table 2.9: Private datasets size for each work (1/2). The type of images composing the dataset and the presence of fat-suppression is reported. [†] These datasets are used in more than one work from the same authors group. In these cases only the more recent is reported.

Papers	Type of Images	# Patients
Martel2007 [162]	T1	3
Mayerhoefer2008 [164]	T1/T2	58
McClymont2014 [165]	T1	128
McLaren2009 [166]	T1	71
Meeuwis2010 [167]	T1	65
Meinel2007 [168]	T1	80
Nagarajan2013 [178]	T1	54
Newell2010 [181]	T1	90
Ortiz2012 [188]	T1	500
Partridge2005 [191]	T1	62
Pickles2009 [204]	T1 fat-sup.	54
Pickles2016 [202]	T1 fat-sup.	112
Preda2006 [206]	T1 fat-sup.	93
Rohlfing2003 [211]	T1 fat-sup.	17
Rosado-Toro2015 [215]	T2	14
Rueckert1999 [219]	T1	8
Sathya2013 [225]	T1 fat-sup.	85
Sinha1997 [231]	T1	43
Szabo2004 [237]	T1	10
Tanner2006 [238]	T1	44
Tuncbilek2012 [245]	T1	55
Twellmann2004 [246]	T1	6
Twellmann2008 [247]	T1	81
Tzacheva2003 [248]	T1	14
Tzalavra2016 [249]	T1	44
Vernaghi2001 [250]	T1	74
Vignati2009 [251]	T1 fat-sup.	21
Vignati2011 [252]	T1 fat-sup.	70
Wang2011 [257]	T1/T2	30
Wang2012 [258]	T1/T2	84
Wang2013 [260]	T1/T2	4
Wang2014 [259]	T1	99
Woods2007 [266]	T1	6
Wu2013 [267]	T1	60
Xiaohua2005 [268]	T1	15
Yang2014 [271]	T1	130
Zheng2007 [275]	T2 fat-sup.	31
Zheng2009 [276]	T2 fat-sup.	36

Table 2.10: Private datasets size for each work (2/2). The type of images composing the dataset and the presence of fat-suppression is reported. [†] These datasets are used in more than one work from the same authors group. In these cases only the more recent is reported.

Some public datasets are available for the research purposes. A list of the freely accessible DCE-MRI for breast cancer analysis is reported in Table 2.11.

Name	# Patients	# Works	Ground-Truth
ISPY1 ¹	207	N/A	pCR, DFS, Recur., ER, PR, HER2
BREAST-DIAGNOSIS ²	88	N/A	ER, PR, HER2
QIN Breast DCE-MRI ³	10	N/A	pCR
QIN-Breast ⁴	67	27	pCR
Breast-MRI-NACT-Pilot ⁵	64	N/A	pCR, DFS, Recur., ER, PR, HER2
TCGA-BRCA ⁶	139	4	ER, PR, HER2

Table 2.11: Public datasets. Number of subjects, related works and available ground-truths are reported.

In only two cases (‘QIN-Breast’ and ‘TCGA-BRCA’), the dataset’s page reports a list of the publication resulting from the use of the public data. The majority of the works proposed to evaluate the pathological Complete Response (pCR) to the treatment. The works arising from these two datasets never address the topics assessed in this thesis.

Moreover, two datasets (‘Breast-MRI-NACT-Pilot’ and ‘ISPY1’) are involved in a private competition. Thanks to the direct collaboration with University of South Florida (USF) and H. Lee Moffitt Cancer Center & Research Institute of Florida we have direct access to the data and to the ground truth. The contest’s aim was to identify imaging metrics (predictors) derivable from contrast-enhanced breast MR images that show a statistically-

¹<https://wiki.cancerimagingarchive.net/display/Public/ISPY1>

²<https://wiki.cancerimagingarchive.net/display/Public/BREAST-DIAGNOSIS>

³<https://wiki.cancerimagingarchive.net/display/Public/QIN+Breast+DCE-MRI>

⁴<https://wiki.cancerimagingarchive.net/display/Public/QIN-Breast>

⁵<https://wiki.cancerimagingarchive.net/display/Public/Breast-MRI-NACT-Pilot>

⁶<https://wiki.cancerimagingarchive.net/display/Public/TCGA-BRCA>

significant association with Disease-Free Survival (DFS) time. The results have not yet published, but they pushed us to develop the last stage of the Computer-Aided Detection and Diagnosis (CAD) for therapy assessment by forecasting the disease recurrence.

Compared with the whole amount of data (the sum of the number of patients of each private dataset and each public dataset is 6540 potential patients), the public number of patients is very few (575 public patients). Only the 9% of the patients is public and freely accessible.

By looking at the histogram of the sizes of the dataset for each work (Fig. 2.6), it is evident that the majority of the datasets contains a small amount of subjects with respect to the whole number of available patients.

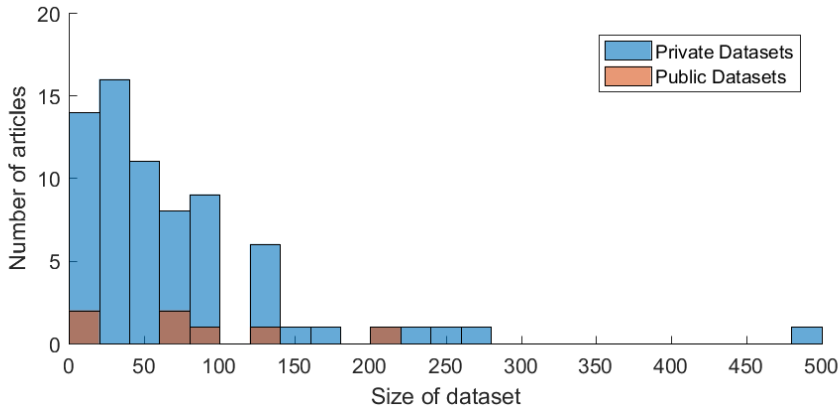


Figure 2.6: Database size histogram. The majority of the approaches are evaluated on small dataset.

Another important issue raised up from this literature analysis is that many parameters of each protocol strongly differs from such others. Indeed, the number of variable parameters is very high. The protocols could vary because of the following acquisition parameters: Acquisition Sequence, Acquisition Plane, Magnetic Field (T), Fat Suppression, Repetition Time (TR - ms), Echo Time (TE - ms), Flip Angle (FA - deg), Field of View (FoV - mm^2), Matrix

(px), Thickness (mm), Pixel Size (mm^2) and Acquisition Time (TA - s). By varying the former parameters, the resulting images could be different. Thus, a specific technique, trained on a fixed set of DCE-MRI acquisition parameters, could fail when applied to a different set of parameters.

Finally, another lack in the breast DCE-MRI is about the availability of follow-up datasets. To validate a therapy assessment algorithm, a multiple time acquisition DCE-MRI is required (such as in Fig.2.7). In particular, for each patient, different scans need to be acquired.

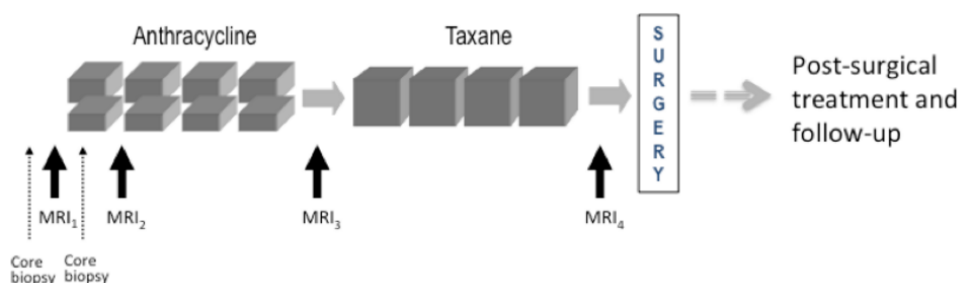


Figure 2.7: Explicative use of serial DCE-MRI examinations during neoadjuvant chemotherapy for breast cancer.

The aim of different scans is to following the tumour response during the therapy. Some algorithms rely on different DCE-MRI scans and could be very protocol-dependant.

Automated Detection, Diagnosis and Therapy assessment

The aim of this thesis is to develop an automated computer-aided detection (CAD) system for automatic detection of breast lesions, diagnosis of malignancy, and patient therapy success forecasting in Dynamic Contrast-Enhanced Magnetic Resonance Imaging (DCE-MRI).

The CAD architecture can be represented by a series of consecutive tasks as depicted in Figure 3.1.

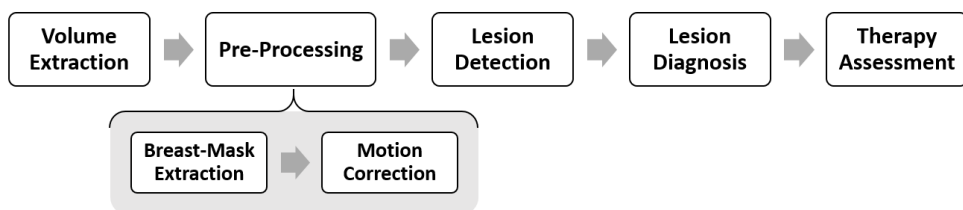


Figure 3.1: Block diagram of the automated proposed CAD.

Each block relies on the result of the previous one; however, the single functionality is developed as a stand-alone process able to work without the other blocks. The consequence of the approach designed as a flow is that the

performance of each block relies on the performance of the previous ones. Then, all the stages have been developed to maximize the performance as a single stage and then combined with the flow with the aim of evaluating the overall performance.

The *Volume Extraction* module extracts the DCE-MRI data from the patient's DICOM files and stores them in a four dimension matrix.

The *Pre-Processing* stage consists of a breast mask extraction stage and a motion correction stage.

In the *Breast Mask Extraction* phase a specific algorithm, aware of the breast anatomy, is able to produce a binary mask only representing the breast parenchyma and excluding background and other tissues. The aim of a breast masking is to reduce the computational cost of next stages and attenuate noise caused by extraneous voxel.

The patient involuntary movements, during the long DCE-MRI acquisition, could introduce artefact and thus affect the final result of the automatic DCE-MRI evaluation. The *Motion Correction* step aims to reduce these motion artefacts before of any further analysis.

The core of the CAD system consists of the next stages of Lesion Detection and Lesion Diagnosis.

In the *Lesion Detection* stage, the CAD scans the four dimension matrix, guided by the breast mask, with the aim of extract suspect tissues as Regions of Interest (ROIs). Each ROI is a group of connected voxel and represents a single lesion to be inspected.

Each ROI is, then, inspected by the *Lesion Diagnosis* module that is able to provide a diagnosis according to the binary class: benignant or malignant.

By exploiting the information derived from the malignant ROIs (when applicable), the stage of *Therapy Assessment* produces a forecasting about the disease recurrence.

Each CAD stage is carefully designed and depicted in the next sections.

3.1 Pre-processing

The pre-processing stage aims to improve the final results by reducing the noise (motion artefacts) and removing the air voxels and any unwanted tissues. In fact, it consists of a breast mask extraction stage and a motion correction stage.

3.1.1 Breast Mask Extraction

In literature, as presented in the Section 2.1.1, breast mask extraction could be approached in several ways: at a pixel level relaying on the signal intensity of few directly derived features; with geometrical approaches for better performing on the final shape of the breast mask; with atlas-based segmentation for exploit anatomical knowledge. In breast segmentation, the most difficult issue to address is discriminating the breast parenchyma from the pectoral muscle since signal intensities, textures and anatomical structures of these tissues are very close each other. The best approach to locate the pectoral muscle is relying on the atlas and exploiting a sort of anatomical knowledge from each subject composing the atlas. A drawback of the atlas-based approaches is in the composition of the atlas itself. Creating a big and reliable atlas is not an easy task and, when focusing on the pectoral muscle, leads to imprecise segmentation of the other borders. The proposed breast mask extraction approach overcomes the issue by mixing geometrical-based and pixel-based approaches. It relies on geometrical anatomical priors to take advance of anatomical knowledge of the breast key points and uses a pixel base segmentation to obtain the best threshold for each border.

It uses a pixel-based Fuzzy C-Means (FCM) clustering to shift the breast mask extraction from a simple grey-level based segmentation to a membership probability one. Moreover, it exploits novel geometrical consideration to weight the classes membership probability according to the breast anatomy. The result is an automated procedure, able to extract an accurate breast mask

without any prior information on the patient dataset (as in the case of atlases). The proposed procedure can be schematically depicted as composed of four main stages (fig. 3.2).

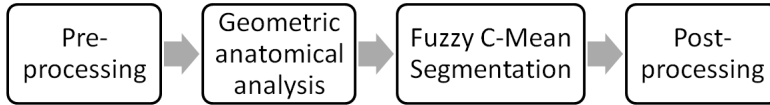


Figure 3.2: The breast mask extraction proposal at a glance.

Each step is intended to resolve a specific problem in breast segmentation, serving as input for the successive stage. The following subsections describe each stage, in order to facilitate the reader in understanding the underlying ideas. To provide a simpler description, when not otherwise specified, all operations are performed along each coronal slice.

The proposed Breast Mask Extraction approach has been published in [161].

Pre-processing

The pre-processing stage lays the foundations for successive stages. The first operation consists in reducing the 4D DCE-MRI data to a single 3D volume, whose voxels are chosen by taking the minimal values along the time dimension for each spatial coordinate. The result is a new 3D volume that preserves all information needed to identify the breast parenchyma boundaries, while strongly reduces the brightness of all those tissues that shows a huge vascularisation and contrast agent presence (like heart and pectoral muscle). Finally, to sharpen borders of the chest wall and to smooth heart and lungs ghosts, a *flattening* process was performed. Flattening consists in applying a 2D median filter on each coronal slice, in order to attenuate brightness variations only along axial and sagittal directions, producing *flat* (with respect to brightness) coronal slices. The flattened 3D volume represents the data on which all successive operation will be executed.

Geometric anatomical analysis

The first step needed in order to identify the breast anatomical geometry is determining the cuboid including the whole breast parenchyma. A primal binary breast mask is thus defined by apply Otsu's Threshold [189] on the flattened data volume. Then the cuboid including the primal mask is calculated, providing the boundaries points (a 2-upla for each dimension) within which the next operations will be applied (fig. 3.3).

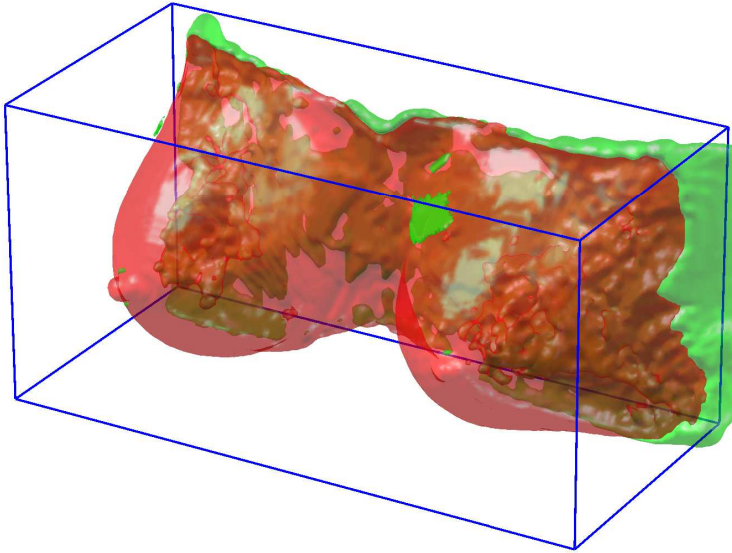


Figure 3.3: The cuboid containing the Otsu segmented volume. In green the breast mask ground-truth, in red the mask obtained by Otsu's segmentation. The cuboid includes almost all the ground-truth.

In order to characterise the anatomical geometry, seven key-points are used: two nipples points (NRP and NLP), two armpits points (ARP and ALP), one chest wall point (CWP), one sternum point (SP) and one heart point (HP). All key-points determination relies only on the primal breast mask and on the cuboid in which it is contained. The two nipples points are identified by finding the two highest points on the breast-air surface according to the

relative position with respect to the middle plane (red and green points in fig. 3.4). The chest wall key-point is identified by searching the point with the minimum height in the breast-air surface enclosed by the two nipples points (that collapses to a line when the nipples points are aligned on the same slice). Since the breast-air surface is a rough segmentation, it could present holes or missing parts; therefore, the point is searched only on the strictly positive values of the height (represented by the black point in fig. 3.4).

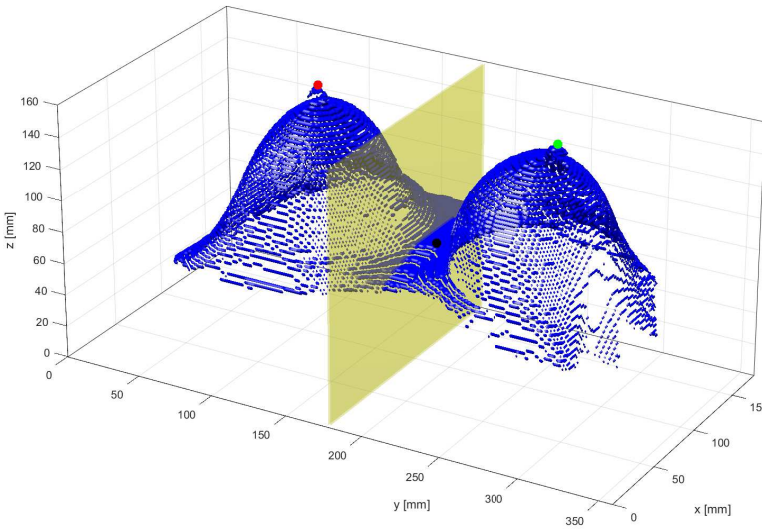


Figure 3.4: Automatic localisation of the nipples (in red and green, respectively, the right and left nipple key-points) and of the chest-wall key-point (in black). In blue the breast-air surface while in yellow the middle plane.

The two armpits, the sternum and the heart points, are calculated relying only on the cuboid boundaries. In particular, the armpits key-points are taken in the middle of the right (ARP) and left (ALP) edges of the back face of the cuboid (red and green points in fig. 3.5). Finally, the sternum point (SP) is calculated in the middle of the two armpits (black point in fig. 3.5), and the heart point (HP) is calculated in the middle of the sternum point and the left armpit point (magenta point in fig. 3.5).

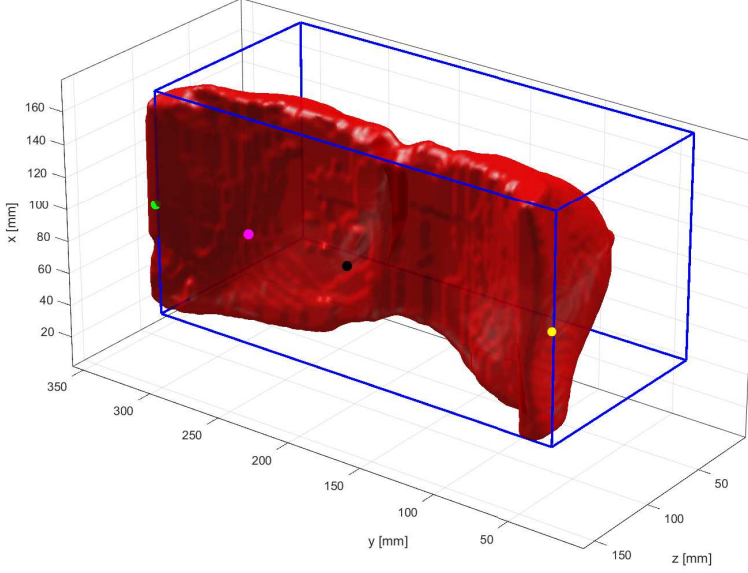


Figure 3.5: Automatic localisation of the armpits (in yellow and green, respectively, the right and left armpits key-points), of the sternum key-point (in black) and of the heart key-point (in magenta). In red the volume and in blue the cuboid previously detected.

Each key-point is provided with an action radius calculated according to the anatomy of the specific patient, defining a *pertinence sphere* for the related key-point. It follows that each key-point influence varies within the pertinence sphere, from a maximum value of 1 (reached in the centre) to a minimum value of 0 (reached on sphere surface and beyond). The *key-points influence function* $\mathbf{kpi}(\mathbf{KP}, \mathbf{KPr}, \mathbf{P})$ can be calculated according to the equation 3.1

$$\mathbf{kpi}(\mathbf{KP}, \mathbf{KPr}, \mathbf{P}) = \begin{cases} 1 - \frac{d(\mathbf{KP}, \mathbf{P})}{\mathbf{KPr}} & \text{if } d(\mathbf{KP}, \mathbf{P}) \leq \mathbf{KPr} \\ 0 & \text{if } d(\mathbf{KP}, \mathbf{P}) > \mathbf{KPr} \end{cases} \quad (3.1)$$

where \mathbf{KP} , \mathbf{KPr} and \mathbf{P} are respectively the key-point, its action radius and the generic point of the 3D volume in which the key-point influence function will be calculated; $d(\mathbf{A}, \mathbf{B})$ is the euclidean distance in a 3D space between the

points A and B, $SP.z$ and $CWP.z$ are the z 3D coordinates of the respective points. Finally, each action radius is calculated as shown in table 3.1.

$NRPr = d(NRP, CWP)$	$NLPr = d(NLP, CWP)$
$ARPr = d(ARP, NRP)$	$ALPr = d(ALP, NLP)$
$CWPr = d(CWP, SP)$	$SPr = HPr = SP.z - CWP.z$

Table 3.1: Key-Points action radii formulas.

Figure 3.6 reports a representative example of all the described key-points and their respective action radii.

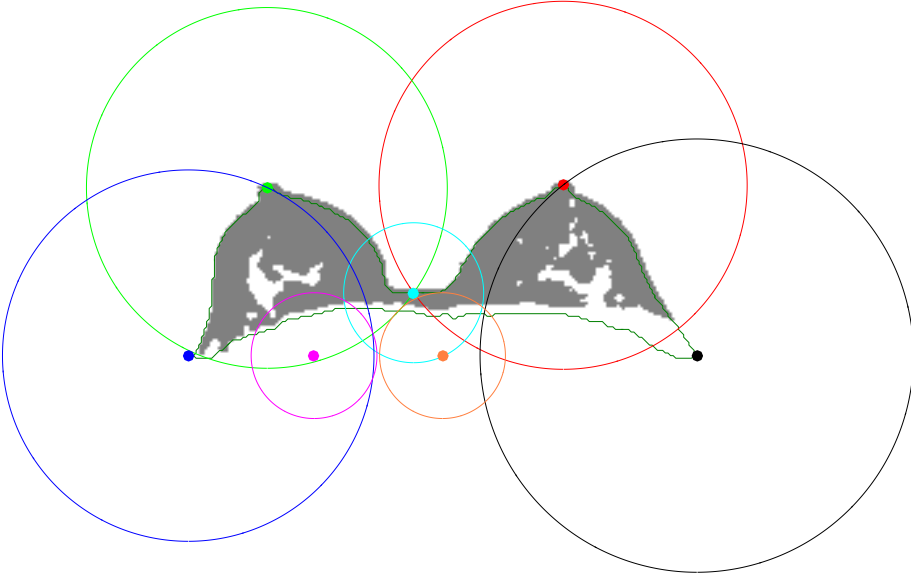


Figure 3.6: Action radius for each key-point. In grey the rough Otsu's segmentation, in dark green the desired breast mask and the key-points as follow: NRP (red), ARP (black), NLP (green), ALP (blue), CWP (cyan), SP (orange), HP (magenta).

Fuzzy C-Mean Segmentation

Traditional segmentation procedures, based on voxels brightness, make use of a threshold value to separate objects according to the image histogram. This procedure has demonstrated great potential in segmenting well defined object in images that does not have a wide grey scale dynamics. In DCE-MRI both conditions are not verified, making the voxel based segmentation approaches not able to distinguish (i.e.) chest wall from breast parenchyma without making additional consideration (like anatomical or geometric ones). For segmentation, Fuzzy C-Mean (FCM) is used. FCM is a clustering procedure very similar to the well known K-Means algorithm, but in which the voxel class membership is not a binary condition, but a probability vector (fuzziness). In this module, FCM is calculated on two classes: the breast tissues (the class with the higher signal intensity) versus the other tissues/air (the class with the lower signal intensity). It is worth noticing that a 3D FCM clustering produces an unsuitable result since it is not able to separate all the breast tissues. On the contrary, a slice-wise 2D clustering allows exploiting local anatomical consideration to achieve a more suited segmentation. Then a slice-by-slice FCM was applied, repeating the clustering along each anatomical axes. Each of these three fuzziness volumes, taking into account brightness transitions between each slice along a given projection, highlights different characteristics of the breast anatomy. In particular: the *Sagittal 2D-FCM* (fig. 3.7a) is able to better enhance the armpits cavities and to better reject the heart and the sternum tissues; in the *Transversal 2D-FCM* (fig. 3.7b) the pectoral muscle edges are well-defined, but fails the armpits cavities estimation (in the most of the patients the grey-levels of the armpits cavities show a significant difference between the right and the left side); the *Coronal 2D-FCM* (fig. 3.7c) can be used to easily detect the breast-air boundary, but shows a very high enhancement of pectoral muscle and heart.

To obtain a single fuzziness volume that better attenuate the pectoral muscle and the heart anatomy while enhancing armpit cavities and breast

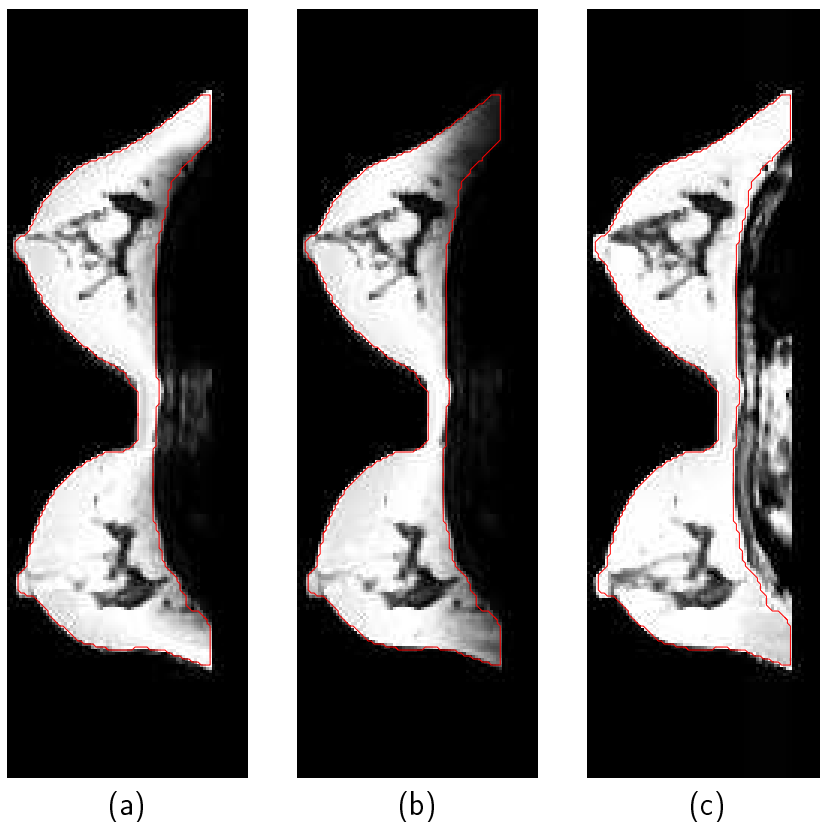


Figure 3.7: The three fuzziness volumes for breast mask extraction (obtained as a slice-by-slice among each projection). The sub-figures show a single transversal slice for each FCM volume. FCM performed slice-by-slice in (a) Sagittal, (b) Transversal and (c) Coronal.

tissues, the three FCM volumes are voxel-wise combined according to the equation [3.2](#).

$$\begin{aligned}
FCM_{\text{weighted}}(P) = & FCM_{\text{sagittal}} \\
& + FCM_{\text{frontal}} \cdot \text{kpi}(\text{NRP}, \text{NRPr}, P) \\
& + FCM_{\text{frontal}} \cdot \text{kpi}(\text{NLP}, \text{NLPr}, P) \\
& + FCM_{\text{sagittal}} \cdot \text{kpi}(\text{ARP}, \text{ARPr}, P) \\
& + FCM_{\text{sagittal}} \cdot \text{kpi}(\text{ALP}, \text{ALPr}, P) \\
& + FCM_{\text{transversal}} \cdot \text{kpi}(\text{CWP}, \text{CWPr}, P) \\
& - FCM_{\text{frontal}} \cdot \text{kpi}(\text{SP}, \text{SPr}, P) \\
& - FCM_{\text{frontal}} \cdot \text{kpi}(\text{HP}, \text{HPr}, P)
\end{aligned} \tag{3.2}$$

It is worth noticing that the first term is not weighted ensuring that each area not covered by the key-points and by their pertinence radii have, at least, a FCM sagittal contribution (the most reliable one); the last two terms are intended to attenuate the effects of the sternum and heart and, for this reason, are subtracted instead of added.

Weighted fuzziness volume is then normalised by a min-max normalisation in $[0, 1]$, after which a 3D median filtering is applied with the specific aim to remove (or at least reduce) the outlier introduced by anatomical peculiarities and facilitate the mask identification. Finally, starting from the processed weighted fuzziness volume, a binary breast mask is obtained by applying a thresholding on the fuzziness values. The best threshold is automatically detected by means of the Otsu's method on the processed weighted fuzziness values.

Post-processing

Post-processing is performed to refine the breast mask obtained in the previous stage. In particular, it consists in the following morphological refinements: a slice-by-slice hole-filling performed first along the frontal direction, then along the sagittal and finally along the transversal one. To be more precise, the frontal refinement fills only holes smaller than a quarter of the current mask

slice area (with a maximum area of $60mm^2$, determined from the maximum diameter of a lesion in the dataset). Then a 3D smoothing (with a Gaussian filter - 3D windows = $[3, 3, 3]$, $\sigma = .65$ and $\mu = 0$) is performed in order to mitigate the effects of a rough segmentation. Finally, to remove small volumes remaining from the heart or sternum, only the bigger connected volume is selected.

3.1.2 Motion Correction

Among the functions of the CAD, there is a sort of motion correction stage finalised to reduce the motion artefacts that might affect the ROI detection and evaluation [238].

As reported in Section 2.1.2, different motion correction techniques (MCTs) have been developed to attenuate the motion artefacts [85, 193]. Rigid MCTs exploit affine transformations in order to preserve points, lines and planes.

However, these MCTs might not model adequately the deformation of breast parenchyma. Consequently, a ‘non-rigid’ MCT such as a Free-Form Deformation (FFD) transformations might be used. Nonetheless, it is worth to note that it might not always be useful to use a complex MCT: in fact, slight deformations can be assumed to be noise overlapped on an un-deformed image and a simple median filter was successfully used.

Generally, MCTs consider voxel intensity fixed while only spatial transformations occur; therefore they rely only on the intensity based metrics. In DCE-MRI an additional issue is present: the voxel intensity changes also because of the contrast agent (CA) flow.

Another important issue is related to the assumption that a single MCT might be able to mitigate the effects of patient movements of different sizes. Some preliminary results in the case of small movements (depicted in Figure 3.8) show that an improper MCT might introduce new artefacts that could lead to unreliable lesion evaluation. Therefore it would be preferable to select the MCT tailored to each patient and to each exam.

There are two possible ways to choose the opportune MCT: (a) the physician might preliminary study the DCE data and, by means of a trial-and-error procedure, select the appropriate MCT or (b) an automatic procedure could rank a collection of MCTs using an adequate quality index (QI) which quantitatively summarise the performance of each MCT on that specific study.

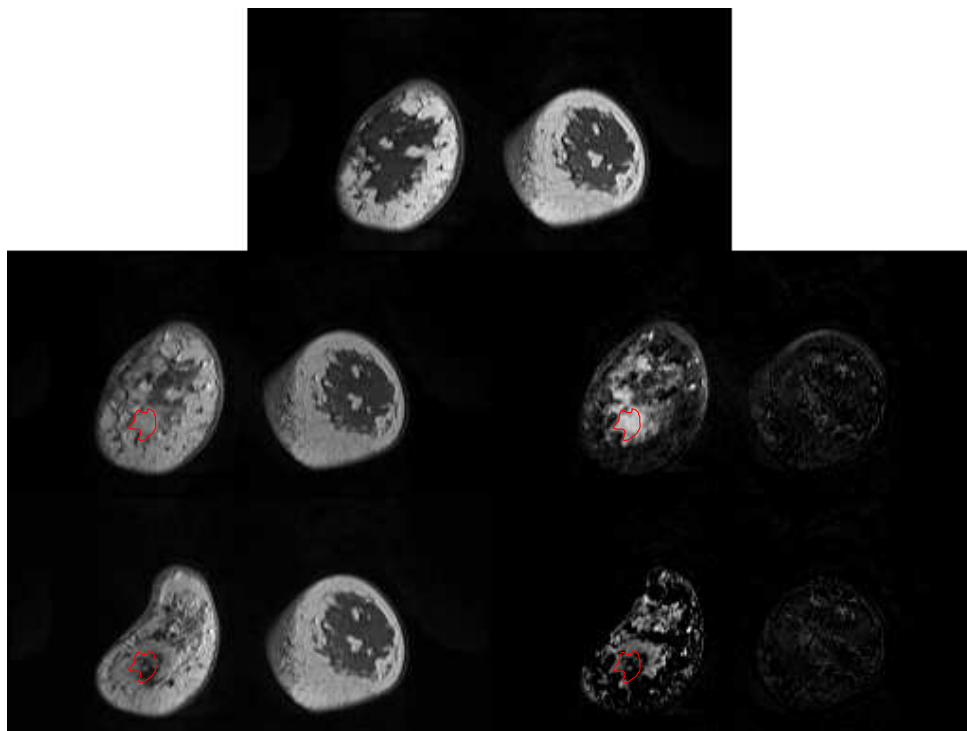


Figure 3.8: A representative case in which some evident artefacts are introduced by an improper MCT (3D free-form deformation with cubic interpolation). It is clear that the new artefacts could lead to an unreliable lesion evaluation. In the first row is shown the pre-contrast MRI data. In the middle row is presented: on the left, an MRI image from the post-contrast series (about 3 min. after the injection) without motion correction and on the right, the corresponding *subtractive* image. The *subtractive* image emphasises regions in which the contrast agent has mostly flowed. In the last row (after motion correction), the post-contrast image (left) and the corresponding *subtractive* image (right) are presented. An inappropriate MCT not only can introduce evident artefacts but also can impinge on the contrast agent effect undermining the final results. Specifically, can be observed a decrease of the enhancement in the manually segmented region of interest (in red).

Of course, the first one is operator-dependant and human-error prone. This module implements the last one approach.

The QI should be an adequate similarity measure able to quantify the difference between the pre-contrast image of a DCE-MRI series (source or reference image) and one, or more, of the subsequent images (target images) after being registered with respect to the source [160]. It has been already evidenced that existing QIs (MSE, PSNR, NCC, etc..) [262, 217, 209] might not be adequate to deal with DCE-MRI data because of the intensity variation due to CA (see Section 2.1.2). This motivated to searching for a new QI based on the most used tracer-kinetics modelling of blood flow (Tofts-Kermode, Extend Tofts-Kermode, Hayton-Brady, Gamma Capillary Transit Time) [241, 242, 100, 227].

In this thesis, a new tracer-kinetic based QI is assessed and proposed. It is suitable to provide an unbiased selection of the most appropriate MCT for a specific exam, study or patient. As in literature there is still an ongoing debate on which is the optimal tracer-kinetic model. To assess the module one QI for each model is constructed and evaluated on the available DCE-MRI dataset.

Each QI produces a ranking of every different MCTs considered for a specific patient; those rankings have been compared to a ‘reference ranking’ constructed *a priori* on a dataset. The correlation coefficient between each QI ranking and the *reference* ranking measures the degree of agreement and therefore the ‘goodness’ of each QI.

Further, computational times should also be considered to ensure that the proposal is clinically applicable. In fact, from some preliminary evaluation, the computing of one QI on a single exam could take up to 15 hours. Thus, a sampling strategy is adopted with the aim to break down the computational effort: the aim is to investigate whether just a small fraction of the whole volume is enough to produce a correct ranking.

The proposed QI has been published in [160] and the data-driven approach to the motion correction has been published in [199].

Motion Correction Techniques

The involuntary movements of the patient, during the DCE-MRI scan, could produce artefacts and thus affect the evaluation of DCE-MRI data. It is well known that, in order to reduce these motion artefacts, a kind of motion-correction should be executed before any DCE-MRI analysis [238]. In the graph in Figure 3.10 is shown how a motion correction technique can fix the time course of the time intensity curve by registering the voxels. The Motion Correction Techniques (MCT) currently used in medical image co-registration which have been examined in this study are:

2D-rigid (ML): an iterative, slice-by-slice, motion correction technique based on affine transformations and on signal intensity similarity values. The only available transformations are: translation, rotation, scale, shear or a mix of these above.

3D-rigid (R_AL & R_AC): a 3D affine motion correction according to the algorithm proposed by Rueckert et al. [219]. This MCT can be performed with different interpolation functions: linear (R_AL) or cubic (R_AC).

3D-non-rigid (R_BL & R_BC): a hierarchical transformation model according to the algorithm proposed by Rueckert et al. [219]. The hierarchical approach consists of a global 3D correction, modelled with affine transformations and a finest local correction by means of a FFD grid on a B-Splines voxel representation. Also this MCT can be performed with different interpolation functions: linear (R_BL) or cubic (R_BC).

ElastiX: a deformable transformation using a B-Spline representation (configured with *BSplineTransform* option). Currently, it is implemented in an open source software for intensity-based medical image registration [122].

Filtering approaches (MEDx3 & MEDx5): as hypothesised in some of our works [159], small deformations could be treated as superimposed noise on the correctly aligned images. Therefore, a median filtering could be applied. It was applied with a sliding window of 3x3x3 or 5x5x5 voxel.

Traditional Quality Indices

With the aim of quantifying the goodness of a MCT, different Quality Indices, measuring the similarity of the first image of the series and the registered images could be used. Typically, they have been based on voxel signal intensity, but it should be emphasised, as stated above, that they might not be able to distinguish intensity variations due to motion or to blood flow.

Root Mean Square Error (R-MSE) [262] - it is calculated on the differences in terms of signal intensity. It's able to quantify the difference of two volumes: the fixed reference (usually the pre-contrast volume), and one among the post-contrast volumes.

$$\text{R-MSE} = \frac{1}{T} \sum_t \sqrt{\frac{\sum_n (I_r(n, t) - I(n, t_0))^2}{N}} \quad (3.3)$$

Peak signal-to-noise ratio (PSNR) [262] - it is the ratio between the maximum dynamic range of the image (maximum possible power of the signal) and R-MSE (the power of noise that could affects the signal).

$$\text{PSNR} = \frac{1}{T} \sum_t 20 \cdot \log_{10} \left(\frac{\max_n I(n, t)}{\text{R-MSE}} \right) \quad (3.4)$$

Normalized Cross Correlation (N-CC) [217, 209] - it quantifies the differences between two images by removing the bias and comparing only the standard deviation, therefore it attenuates the effects of a

different distribution in the histograms due to the presence of a contrast agent (CA):

$$\text{N-CC} = \frac{1}{TN} \sum_{t,n} \frac{(I(n, t_0) - \mu)(I_r(n, t) - \mu_r(t))}{\sigma \sigma_r(t)} \quad (3.5)$$

where $\mu = \sum_n I(n, t_0)/N$ and $\mu_r(t) = \sum_n (I_r(n, t))/N$ are the averages of I and I_r respectively, and $\sigma = \sqrt{\sum_n (I(n, t_0) - \mu)^2}/N$ and $\sigma_r(t) = \sqrt{\sum_n (I_r(n, t) - \mu_r(t))^2}/N$ are the standard deviations of the two images.

Physiological tissue models

As already observed in the introduction, in DCE-MRI voxel intensity changes because of the contrast agent flow. Contrast medium concentration could be modelled by means of several approaches commonly used in breast DCE-MRI. The different approaches can be catalogued on the base of the underlying physiological assumptions concerning blood plasma and the extra-vascular extracellular space (EES).

The description of the following models refers to the notations established in the Table 3.2:

Tofts-Kermode (TK) model [241, 134]: This model uses a simple compartmental approach (Figure 3.9) in which the intra-vascular compartment can be neglected. The $C_t(t)$ is calculated as the convolution of an exponential impulsive response and a specific Arterial Input Function (AIF) $C_p(t)$ (Eq. 3.6 and symbols as in Tab. 3.2).

$$C_t(t) = K^{\text{trans}} \int_0^t e^{-\frac{K^{\text{trans}}}{v_e}(t-s)} \cdot C_p(s) ds \quad (3.6)$$

Extended Tofts-Kermode (ETK) model [242]: This model improves the previous one, in fact, plasma volume fraction v_p has been added assuming that the intra-vascular compartment influence can not be neglected (Eq. 3.7 and symbols as in Tab. 3.2).

$$C_t(t) = K^{\text{trans}} \int_0^t e^{-\frac{K^{\text{trans}}}{v_e}(t-s)} \cdot C_p(s) ds + v_p C_p(t) \quad (3.7)$$

Hayton-Brady model [100]: The authors proposed a bi-exponential model (Eq. 3.8 and symbols as in Tab. 3.2).

$$C_t(t) = \frac{A}{(a-b)} (e^{-at} - e^{-bt}) \quad (3.8)$$

Gamma Capillary Transit Time [227]: Schabel proposed the Gamma Capillary Transit Time model (GCTT) in order to unify many of the previous proposed models such as TK, ETK, adiabatic tissue homogeneity (ATH) and two-compartment exchange (2CX) (Eq. 3.9 where Γ is the upper incomplete gamma function [4] and other symbols as in Tab. 3.2).

$$\begin{aligned} \tau &= \frac{t_c}{\alpha} \\ R_v(t) &= \Gamma\left(\frac{t_c}{\tau}, \frac{t}{\tau}\right) \\ R_p(t) &= \frac{E e^{-k_{ep}t}}{(1 - k_{ep}\tau)^{t_c/\tau}} \cdot \left[1 - \Gamma\left(\frac{t_c}{\tau}, \left(\frac{1}{\tau} - k_{ep}\right)t\right) \right] \\ C_t(t) &= F \cdot (R_v(t) + R_p(t)) * C_p(t) \end{aligned} \quad (3.9)$$

In order to complete the description of *TK* and *ETK* models, different AIF could be used:

Weinmann [263] proposed a bi-exponential AIF (Eq. 3.10):

$$C_p(t) = D \cdot \sum_{i=1}^2 a_i e^{-m_i t} = D(a_1 e^{-m_1 t} + a_2 e^{-m_2 t}) \quad (3.10)$$

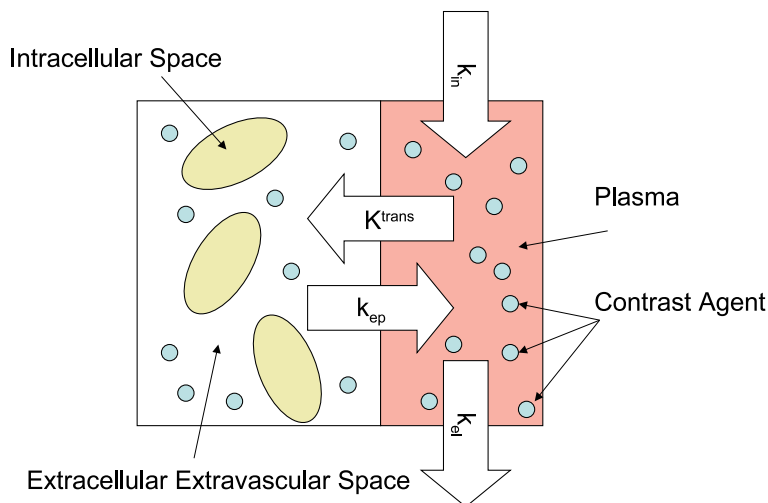


Figure 3.9: Compartmental approach for the distribution of the contrast agent within the tissue. The symbols are described in Table 3.2.

Symbol	Description	Units
$C_p(t)$	Tracer concentration in blood plasma	$\frac{\text{mmole}}{\text{liter}}$
$C_t(t)$	Tracer concentration in voxel	$\frac{\text{mmole}}{\text{liter}}$
K^{trans}	Volume transfer constant or permeability surface area (product per unit volume of tissue between EES and plasma)	$\frac{1}{\text{min}}$
k_{ep}	Efflux rate constat from EES to plasma $k_{\text{ep}} = \frac{K^{\text{trans}}}{v_e}$	$\frac{1}{\text{min}}$
v_e	EES volume per unit volume of tissue	-
v_p	Blood plasma volume per unit volume of tissue	-
E	Extracted blood fraction	-
F	Blood flow to the tissue of interest	$\frac{1}{\text{min}}$
t_c	Blood capillary transit time	min
α	Dispersion of capillary transit time	-

Table 3.2: Physiological Models Symbols.

Assuming that D is the injected dose of contrast medium ($\frac{\text{mmole}}{\text{kg}}$), a_i are the amplitudes ($\frac{\text{kg}}{\text{liter}}$) and m_i are the decay time constants ($\frac{1}{\text{min}}$) for

each exponential. The parameters values are [263]: $D = 0.1 \frac{\text{mmole}}{\text{kg}}$, $a_1 = 3.99 \frac{\text{kg}}{\text{liter}}$, $a_2 = 4.78 \frac{\text{kg}}{\text{liter}}$, $m_1 = 0.144 \frac{1}{\text{min}}$, $m_2 = 0.0111 \frac{1}{\text{min}}$.

Parker [190] proposed a population-averaged AIF modelled via a mixture of 2 Gaussian curves plus an exponential modulated with a sigmoid function (Eq.3.11):

$$C_p(t) = \sum_{i=1}^2 \frac{A_i}{\sigma_i \sqrt{2\pi}} e^{-\frac{(t-T_i)^2}{2\sigma_i^2}} + \alpha \frac{e^{-\beta t}}{1 + e^{-s(t-\tau)}} \quad (3.11)$$

Assuming that A_i , T_i and σ_i are the scaling constants (mmole · min), centres (min), and widths (min) of the i^{th} Gaussian; α and β are the amplitude (mmole) and decay constant ($\frac{1}{\text{min}}$) of the exponential; and s and τ are the width ($\frac{1}{\text{min}}$) and centre (min) of the sigmoid, respectively. The parameters values are [190]:

$A_1 = 0.809 \text{mmole} \cdot \text{min}$, $A_2 = 0.330 \text{mmole} \cdot \text{min}$, $T_1 = 0.17046 \text{min}$, $T_2 = 0.365 \text{min}$, $\sigma_1 = 0.0563 \text{min}$, $\sigma_2 = 0.132 \text{min}$, $\alpha = 1.050 \text{mmole}$, $\beta = 0.1685 \frac{1}{\text{min}}$, $s = 38.078 \frac{1}{\text{min}}$, $\tau = 0.483 \text{min}$.

Proposed Quality Indices

In order to design a Quality Index suitable for dealing with both spatial transformations and signal intensity variations due to contrast media, the following approach is proposed.

The contrast agent concentration $C_t(t)$ is calculated from the DCE-MRI data according to [228] only for a subset of voxels within the whole DCE volume. The chosen subset (called pre-selection volume) should include voxels having a maximum relative-enhancement above 30% in order to have a large vascularisation [159].

Subsequently, $C_t(t)$ is fitted to one of the models described in section 3.1.2 solving a non-linear curve-fitting problem in the least-squares sense (Figure 3.10).

The median value over the whole subset of the squared 2-norm of the residual [160] is proposed as the Quality Index (QI):

$$E = median_n \sqrt{\sum_t (C_t^{fitted}(t) - C_t^{measured}(t))^2} \quad (3.12)$$

Different QIs are obtained in the following condition:

- *TK-W*: using the Tofts-Kermode (TK) model and the AIF suggested by Weinmann;
- *TK-P*: using the Tofts-Kermode (TK) model and the AIF proposed by Parker;
- *ETK-W*: using the Extended Tofts-Kermode (ETK) model and the Weinmann AIF;
- *ETK-P*: using the Extended Tofts-Kermode (ETK) model and the AIF suggested by Parker;
- *HB*: using the Hayton-Brady model;
- *GCTT*: using the Schabel model and the Parker AIF.

Combining QIs

With the aim of proposing a more reliable QI some mixture of the previous suggested model-based QIs are tested. In order to be the index of comparable ranges, a min-max normalisation is applied on the patient-base values of the QI under examination. After the normalisation, the QIs were mixed with different combination strategy:

- *MIX-MEAN*: after the min-max normalisation, all the QIs were mixed with a mean function.

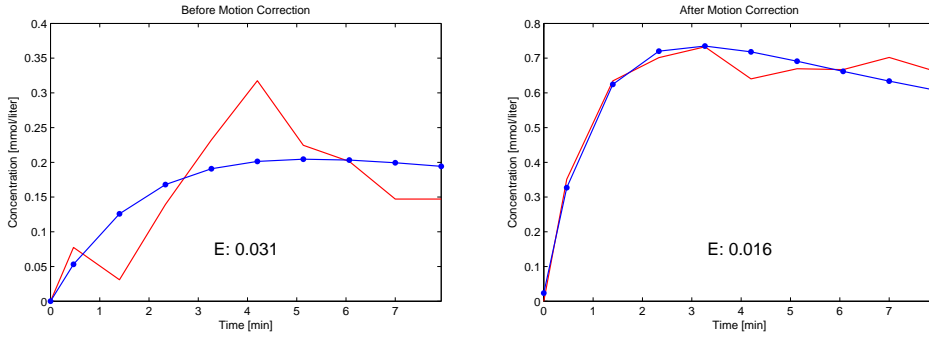


Figure 3.10: Fitting (blue) of DCE-MRI sampled data (red) by means of a physiological model (ETK-P). The error values (E), calculated as in Eq. 3.12, are shown. The motion-corrected data (on the right) better fits the underlying physiological model achieving a lower value of the fitting error.

- *MIX-MEDIAN*: after the min-max normalisation, all the QIs were mixed with a median function.
- *MIX-MAX*: after the min-max normalisation, only the maximum value among all QI is considered.
- *MIX-MIN*: after the min-max normalisation, only the minimum value among all QI is considered.

In particular, the first four indices are mixed in order of performance.

Sampling Strategy

With the aim to apply the MCTs ranking in a clinical scenario, the execution times and the computational load should also be considered. Therefore, to reduce such impact, a sampling strategy is evaluated.

On the basis of some preliminary results, the size of the dataset, after the pre-selection stage, consists of 35000 voxels on average (in the range: 10000-70000 for a DCE-MRI with a spatial resolution of 128x256x80 voxels).

Consequently, the execution time, needed to evaluate a QI, could rise to 10 hours for each study.

Therefore, a sub-sampling of the dataset is proposed. A fixed percentage of the whole pre-selected volume is randomly extracted; the most suitable MCT is selected by computing the QI only on the subset of the motion corrected volume. For reducing the computational load, the dimension of the dataset to be analysed should be a very little portion of the entire pre-selected data. Several fractions of the whole preselected volume have been tested with the aim of finding out the more suitable ratio that could break down the computational load while preserving the results. A Monte Carlo simulation on 100 different sub-sets for each ratio ranging from 100% to 0% with a 0.01% step has been executed. For each extraction, the best QI (previously selected) is evaluated and then the ranking for each MCT was extracted by means of S-RCC. As overall performance indicator of each specific ratio the median value of the QI over the 100 extractions is considered. A more specific performance indicator considers the first selected MCT and, among the 100 extractions, calculates the average hit-rate of the proposed QI among all the patient dataset.

3.2 Lesion Detection

Lesion detection is the basis of an automated computer-aided diagnosis technique for the tumour classification in breast DCE-MRI. Most of the literature proposals propose a semi-automatic approaches using human initialization and then, using a simple thresholding based on few basic features, or finer geometrical refinement can provide the final segmentation.

The purpose of this module is to fully automate the identification of lesions (whether malignant or benign) as sensibly as possible, while simultaneously minimising the number of false alarms. The next stages, such as tumour classification according to his malignity and the therapy assessment, highly depend on the results of this stage. The more are well detected the lesions the better will be the results of the next stages.

The whole lesion detection process can be modelled as a series of successive refinements (fig. 3.11) on patient DCE-MRI images, each one intended to highlight suspect lesions while eliminating noise, offsets and foreign tissues (muscle, bones, etc.). The result is a binary voxel by voxel labelling (intended for suspicious/not suspicious) whose union represent a Region Of Interest (ROI) to be submitted to expert radiologist's advice or to further automatic analysis.



Figure 3.11: Block diagram of the Lesion Detection method.

The proposed Lesion Segmentation approach has been published in [159].

3.2.1 Pre-selection

Each voxel is associated with a Time Intensity Curve (TIC) representative of the temporal dynamics of the signal. TIC reflects the absorption and the

release of Contrast Agent (CA), following vascularisation characteristics of the tissue under analysis [131].

Moreover, for each time instant k the Relative Enhancement (RE) is defined as eq. (3.13):

$$RE(k) = \frac{TIC(k) - TIC(0)}{TIC(0)} \quad (3.13)$$

RE curve still models the absorption of the contrast agent along time, but refers to it (to a first order approximation) in mmol/kg.

Pre-selection step is used to reduce the number of voxels to be submitted to the classifier: each voxel is pre-classified. All voxel in which $\max(RE(t))$ is below 30% of the basal signal are marked as *not-suspicious* while all the others are marked as *unsure* and will be submitted to the subsequent classification step.

This step represents the novelty contribution to lesion detection. As outlined in Figure 3.12, separating suspicious from pre-selection mask voxels is much more difficult than separating not-suspicious from pre-selection mask voxels, since the TICs of the first two kinds of voxels are more similar than those belonging to the second two kinds of voxels. As a matter of fact, classifiers trained on suspicious and pre-selected voxels had a greater generalisation ability with respect to ones trained on the suspect and not-suspect ones. In particular, in the second case, the obtained classifier is unable to reliably recognise suspect voxel from not suspect ones, generating an output very close to the pre-selection mask.

By using this step, a first rough segmentation is carried out inside the breast mask. That leads to focusing the discriminant power of the classifier on a smaller problem only inside the pre-selection mask.

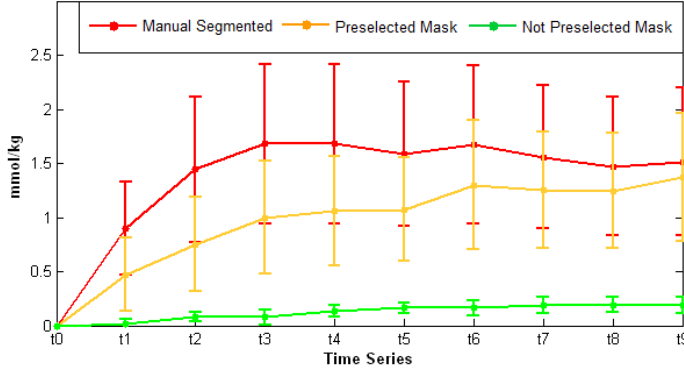


Figure 3.12: Examples of average TICs over the three types of ROIs. Vertical bars represent standard deviations.

3.2.2 Feature extraction

Starting from data provided by DCE-MRI images is possible to extract several sets of features, representative of specific characteristics and properties. For the breast segmentation task and lesion detection, the dynamic features show best results [74].

At this stage, according to the physician suggestion (domain experts), we have used only five features (within all the dynamic feature presented in Section 1.3.1) to fully describe the Time Intensity Curve (TIC). They are defined on mathematical models (but not on pharmacokinetics), and this makes them computationally efficient and robust to contrast agent variation. The dynamic features used at this stage are:

- *Area under TIC (AUC)*, total amount of contrast agent absorbed;
- *Relative Enhancement at Maximum Point (ReMax)*, contrast agent peak;
- *Time To Peak (TTP)*, the time in which ReMax is gained;
- *Wash-In Slope (WIS)*, angular coefficient of linearised approximation of TIC curve from time 0 to TTP;

- *Wash-Out Slope (WOS)*, angular coefficient of linearised approximation of TIC curve from time TPP to last time.

3.2.3 Segmentation by Classification

This last stage performs a segmentation of the whole DCE-MRI volume into different ROIs. Each ROI is composed of the connected voxels considered belonging to a lesion by a classifier. In this module, the classification is performed through a Support Vector Machine (SVM) classifier (with third-degree Radial Basis Function kernel; unitary cost; $\epsilon = 10^{-3}$). The best classifier for the specific task is chosen according to the results presented in the Chapter 4 within the considered classifiers illustrated in the Section 1.3.1.

The optimisation of the SVM is performed on a subset of the dataset never used for training and testing the classifier.

3.3 Lesion Diagnosis

In this phase, each ROI, is segmented by the previous stage, is classified according to the aggressiveness of the lesion. While there is a certain amount of evidence that dynamic information can be used for lesion classification, it still remains unclear whether other kinds of feature (e.g. texture-based) can add useful information. The classification is, then, performed on Local Binary Patterns on Three Orthogonal Planes (LBP-TOP) descriptors belonging to the category of textural features. To the best of our knowledge, this would be the first time that LBP-TOP descriptors are used for breast tissue classification in DCE-MRI.

The Lesion Diagnosis is performed according to the simple schema in Figure 3.13.

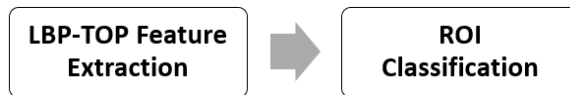


Figure 3.13: Block diagram of the lesion diagnosis approach.

The proposed Tumour Diagnosis approach has been published in [198].

The following section will introduce some concepts about LBP, LBP-TOP and the approaches of classification.

3.3.1 LBP descriptor

Local Binary Patterns on Three Orthogonal Planes (LBP-TOP) [186] provides a very efficient set of feature by thresholding the neighbourhood of each pixel and considers the result as a binary number. As threshold, the luminance value of the pixel in the centre of the neighbourhood is considered. Then the binary numbers are interpreted as a local pattern and a histogram of the occurrences for all the patterns of the image is calculated. This simple 2D implementation provided very good performance in unsupervised texture

segmentation [186]. The original Local Binary Patterns (LBP) operator was only defined to deal with the 2D spatial information. Later, it was extended to a spatio-temporal context for dynamic texture analysis with the Volume-LBP (VLBP) [274]. The VLBP address the spatio-temporal problem handling a 3D volume with the X, Y and T axis. The neighbourhood is then considered on a 3D windows over both the spatial and temporal dimension. To make VLBP computationally simple and easy to be extended, an operator based on co-occurrences of Local Binary Patterns on Three Orthogonal Planes (LBP-TOP) was also introduced. LBP-TOP considers three orthogonal planes: XY, XT and YT, and concatenates LBP histograms in these three directions as shown in Figure 3.14.

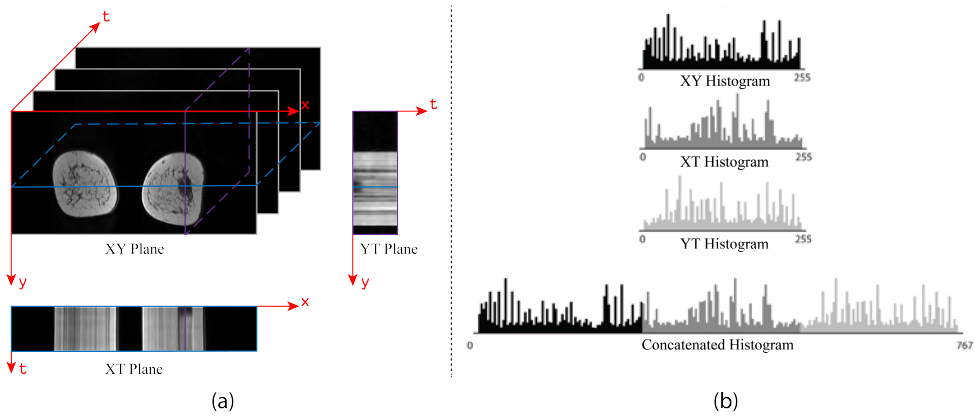


Figure 3.14: LBP-TOP extraction strategy starting from the 3D volume (a) till to the concatenates histogram (b) on the bottom-right.

LBP and LBP-TOP have proved to have great potential respectively in face description [7] and visual speech recognition of moving lips [273].

In order to fit LBP-TOP features to the 4D DCE-MRI volume (composed by X,Y,Z and T axis), The histograms are calculated for each slice (on the coronal planes of the DCE-MRI). The LBP-TOP features were extracted only for the voxel within the ROI that need to be classified. Then the histogram of

the patterns for all the slide are summed into one global histogram that refers to the whole ROI. A multi-resolution version of the LBP-TOP as proposed into [186] with a temporal radius of 1 and 2 is implemented and used. Then, for each ROI, there are three histograms from temporal radius 1 (XY-1, XT-1, YT-1) and three histograms from temporal radius 2 (XY-2, XT-2, YT-2). With the purpose of achieving better results different feature sets are defined and evaluated, as reported in Table 3.3.

Feature Set	XY	XT	YT
XY	•		
XT		•	
YT			•
XYXT	•	•	
XYYT	•		•
XTYT		•	•
ALL	•	•	•

Table 3.3: Different subset of LBP-TOP feature for lesion diagnosis.

3.3.2 Classification

This last stage provides a classification of each ROI according to the LBP-TOP features. The best classifier for this specific task, chosen after a preliminary result presented in Chapter 4, is a Random Forest (RF) (made up of 100 Random Trees each one using a random subset of the features with no limitation on its maximum depth). The peculiarity of Random Forest to train different Random Trees on a subset of the features is the key-point in the classification of such a large set of features provided by LBP-TOP.

3.4 Therapy Assessment

In this specific module, DCE-MRI semi-quantitative features have been used to discriminate the recurrence of the disease. The patient has a recurrence if cancer is found after surgery treatment. Usually, a period of time of 4-years is considered to assess a recurrence-free treatment result.

After voxel-by-voxel lesion segmentation and then, after lesion-by-lesion aggressiveness diagnosis, only the malignant lesions have been considered at this stage. For each patient with at least a malignant lesion, the feature extraction and, consequently, the classification is performed to produce the final binary judgement about a possible recurrence of the tumour.

3.4.1 Feature Extraction

A set of different features has been used to assess the recurrence (the most common are presented in the Section [1.3.1](#)).

Dynamic features

Dynamic features (DYN) are extracted directly from the Time Intensity Curve (TIC). Since a whole lesion is analysed at this stage, the median value of the single feature is considered as representative value for that features in each ROI under examination. The considered dynamic features are: signal enhancement ratio (SER), percent enhancement (PE), post-initial enhancement (PIE), area under curve (AUC), normalised area under curve (nAUC), maximum relative enhancement (ReMax), wash-in slope (WIS), wash-out slope (WOS) and Degani curve type (DCT).

In addition to the features proposed in the literature and so far listed, two new features have been added. Relying on the fact that AUC and, in particular nAUC, brings information about the most active part of the lesion, the percentage of the most active part is considered as a new feature. In the

Figure 3.15 an example of nAUC map for a single slice is given. It is easy to spot the most active regions of the tumour.

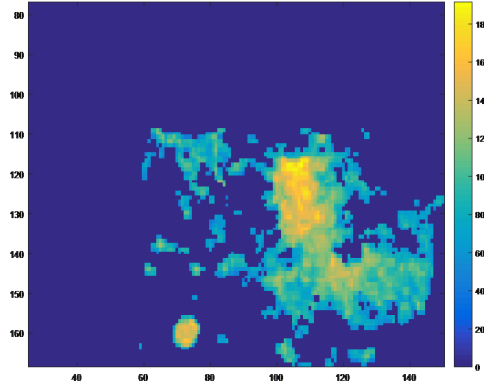


Figure 3.15: Normalized Area Under Curve map for a single slice calculated inside the lesion ROI. It is easy to spot the most active regions of the tumour.

By varying the approach of how to thresholding the nAUC map two different features are proposed: AUGT, AULT. In *AUGT* (Area Under Global Threshold) a global threshold, chosen with the Otsu method, within the nAUC values of all the patients. In *AULT* (Area Under Local Threshold) a patient based thresholding is performed by applying Otsu only on the value of the single patient.

Pharmacokinetic features

Physiologically Based Pharmacokinetic features (PBPK) extraction is performed relying on the Tofts-Kermode (TK) model [134, 241], a simple compartmental approach in which the intra-vascular compartment can be neglected.

According to this model the time course of the contrast agent concentration $C_t(t)$ is the result of convolution between an exponential kernel and arterial input function (AIF) $C_p(t)$ (Eq. 3.14 and symbols as in Table 3.2).

$$C_t(t) = K^{\text{trans}} \int_0^t e^{-\frac{K^{\text{trans}}}{v_e}(t-s)} \cdot C_p(s) ds \quad (3.14)$$

The pharmacokinetic parameters were calculated from the mean signal intensity of the ROI over the time course of the acquisition, resulting in three pharmacokinetic parameters: the transfer constant (K^{trans}), the extracellular extra-vascular space fraction (v_e) and the Efflux rate (k_{ep}). The *Transfer constant* (K^{trans}) or permeability surface area indicates the rate constant of contrast agent transfer from the plasma compartment into the extracellular extra-vascular space. The *Efflux rate* (k_{ep}) quantifies the ratio of contrast agent escapes from the extracellular extra-vascular space back into the plasma compartment. While the *extracellular extra-vascular space fraction* (v_e) can be calculated from the ratio of K^{trans} to k_{ep} . The pharmacokinetic features have been extracted only in the baseline volume (the DCE-MRI acquired before of any treatment), because any treatment could affect the behaviour of the breast tissues and, then, on the reliability of this kind of features.

Morphological features

In this stage, very simple geometrical features have been used, in particular volumes and the longest diameters of the lesions have been carried out. The morphological features bring information about the sizes of the lesion and, when evaluated in the different phases of the treatment, could be used to evaluate the effectiveness of a treatment. Therefore, for each geometrical measurement, the values before and after the neoadjuvant treatment are considered as features.

Clinicopathologic features

The following features are directly extracted from the patient record and represent the clinical status and the pathological condition. The considered feature are: Race (categorical), Age, tumour laterality, positivity to Estrogen-

Receptor (ER_{pos}), positivity to Progesterone-Receptor (PR_{pos}), positivity to Hormone-Receptor ($HER2_{pos}$), $HR/HER2$ status, pathological Complete Response (pCR) and Residual Cancer Burden (RCB).

3.4.2 Classification

To better exploit the differences between feature types, an ensemble of classifiers has been designed.

Multi-classifier

The proposed Multiple Classifier System (MCS) combines the results of two classifiers trained separately with dynamic and pharmacokinetic features feature on a side and on morphological and clinicopathologic feature on the other hand (Fig. 3.16).



Figure 3.16: Block diagram of the therapy assessment Multiple Classifier System. Weighted Majority Voting (wMV) as combining strategy was used.

In each classification branch an AdaBoost classifier is trained using 100 decision stump as weak classifiers.

Combining

The result of each branch is the probability of disease recurrence derived from a classification of the specific feature group. The combination is obtained with a weighted Majority Voting (wMV) strategy.

3.5 Putting it all together

The final intent of this thesis, besides of designing each single module to the best of our knowledge, is to create an automated CAD to support the physician in the hard task of inspecting a DCE-MRI study.

An automated CAD should, then, performs all the cascade of the modules, as presented in Figure 1.9. The final version of the CAD is intended to produce, for each patient, different ROIs, a classification of aggressiveness for each ROI and, if a malignant lesion is present, a Therapy assessment in terms of recurrence of the primary tumour.

The first version of our automated CAD implements the first four steps of the designed architecture. In particular, it applies the Breast Mask extraction step, the motion correction module, the Lesion Detection and the Lesion Diagnosis. The results of a so designed CAD will be presented in Chapter 4.

3.6 Remote Computing

The biomedical sector requires a continuous verifying and updating of the proposed approaches. In most of the cases, only a close collaboration with physicians has allowed improvements in the results.

Thus, to push the collaboration of more physicians and to have a valuable feedback for further improving the techniques and to apply the research progress in a realistic environment, a framework for tele-medicine that allows advanced medical image remote analysis in a secure and versatile client-server environment is proposed.

In this section, the high-level architecture for remote processing of data, with a special attention to security and scalability issues, is presented. Moreover, a preliminary implementation of the proposal has been realised using low impact technologies and up-to-date standards.

The system is designed with the following three constraints in mind:

- easy integration into third-party client-side software;
- TCP/IP network infrastructure;
- up-to-date open standards.

To provide easy integration, the responsibilities between a pre-existent client-side software and the client-side application of the proposed architecture have been divided: the first one has to interact with the user, making all operation required to interact with proposed architecture totally transparent to the operator, while the second one has to manage the data transmission and results reporting. The proposed strategy allows meeting the easy integration goal as long as the third-party client implements (with the aim of a plug-in, API or other forms of customization) the steps required to interact with the proposed system client-side application.

The proposed architecture for remote processing approach has been published in [200, 201].

In the following, the general structure and a case-study implementation is presented.

3.6.1 Architecture layers

The system is organised as a multilayer client-server architecture implementing a multi-client/single-server model. Within the same node, different layers communicate using the file-system (see Fig. 3.17).

Each layer has a well defined role as presented in the following sections.

L1 - Communication

This layer manages every detail of transmission and synchronisation (security, physical interconnection, etc.). It creates communication channels between client and server for data transfer.

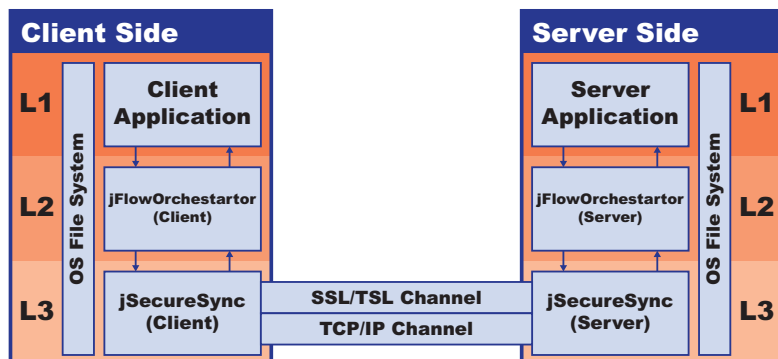


Figure 3.17: Layers overview of the proposed architecture for remote computing. Each layer provides: Communication (L1), Orchestration (L2) and Application (L3).

L2 - Orchestrator

This layer manages communication flow between client and server. It adapts the data generated from the application on the client (layer 3) in a suitable format to be adequately processed by the application layer on the server side. This layer manages the job required by the client and sends notifications in regards to the job's status.

L3 - Application

This layer represents the application used both on client and server side. On the client, it represents the pre-existing image processing software plus the client-side tools, while on the server side it is composed of all software, tools and means needed to provide required operations done, if necessary, as parallel operations.

It is worth to underline that the Communication layer can be completely implemented without knowledge of the final context and application. The Orchestrator layer can be only partially decoupled from the specific context,

while the Application layer cannot be delineated without a specific context and application.

3.6.2 Communication layer

The component which implements connection establishment and management, command transmission and file-state synchronisation is called *jSecureSync*. It has been coded in Java in order to increase portability.

Running both on the client side and on the server side, it implements the multi-client/single-server model: the client starts communication, then the server creates a new thread for each accepted incoming connection. Once communication is established, client and server side operate symmetrically: on both sides, *jSecureSync* runs a Connection Manager module that manages every aspect of file synchronisation over the opened channel. After the Connection Manager starts, client and server act like peers.

Client and server modules establish two different channels (Fig. 3.17) exploiting Java TCP/IP sockets:

- a non-secure channel (via plain TCP/IP): it is used to transmit heavy data (like volume data) and does not carry private sensible information;
- a secure channel (via SSL over TCP/IP): it is used to transmit commands and private sensible information.

Clients and server communicate through a protocol with low overhead (coded in hexadecimal format). Fig. 3.18 presents the protocol commands:

- **HELO**: Client asks to open a channel (for synchronisation process) with the server;
- **ALIVE**: Used by peers to communicate, to be active, or to ask for information about the status of the other peer;

- **OK v1.0:** The server acknowledges a client request and, at the same time, it instruct the client on the version of the protocol used;
- **SND_RQ:** The peer requests to synchronise a file over the secure channel (SSL over TCP/IP);
- **INSECURE_SND_RQ:** The peer requests to synchronise a file over the non-secure channel (plain TCP/IP);
- **SND_ACK:** Acknowledges to allow the other peer to send over the secure channel (SSL over TCP/IP);
- **INSECURE_SND_ACK:** Acknowledges to allow the other peer to send over the non-secure channel (plain TCP/IP);
- **CLOSING_CONNECTION:** Calling peer informs the other one that after this command it will stop the communications by closing all channels (ack is not requested).

SSL/TLS channel security has been realised using a symmetric authentication policy (client-authenticated mode [52–54]), issued during user registration as an authorised client (see Fig. 3.19). This means that every new client has to successfully achieve a one-time registration step to be recognised as a real, authorised client and receive its couple of security certificates (one to verify server authenticity, and the other as proof of being a trusted client to the server). Certificates contain a Public Key and a Signature, both used to identify the user on server-side and to grant access to server features. The procedure for authentication and authorization through certificates is achieved by means of Java services using Java Authentication and Authorization Service (JAAS) [133, 187] classes. This choice guarantees compatibility over different networks architecture supporting the TCP/IP stack protocols and portability (all virtualization is made by the Java Virtual Machine). This implementation uses Elliptic curve Diffie-Hellman (ECDH) [16, 32] as session key agreement

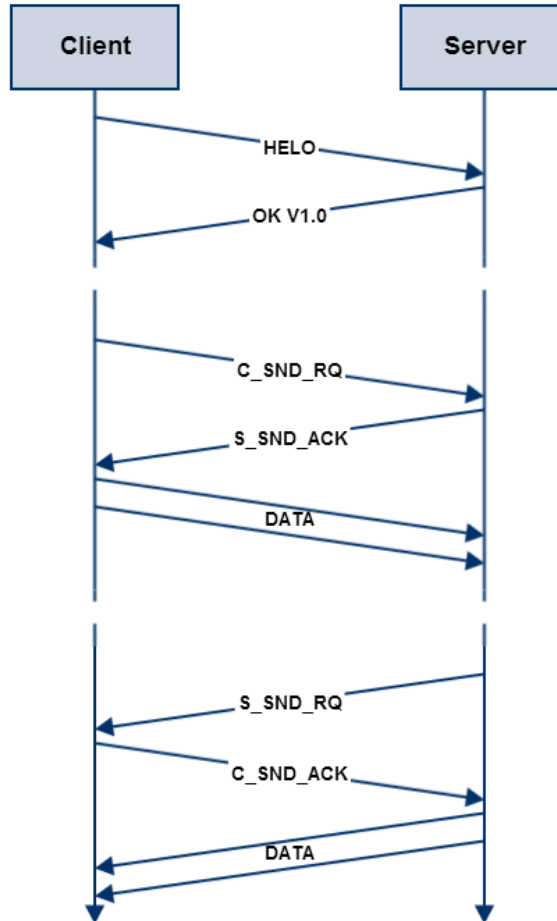


Figure 3.18: Client-Server communication protocol timing.

protocol, while the channel is secured by using an AES 128bit encryption with Cipher-Block Chaining (CBC) as cipher block modality [39, 54]. The use of Client-Authenticated mode allows the server to extract client credential directly from SSL session, making authentication and authorization step achievable through JAAS services without using an ad-hoc access protocol. Digital certificates are provided according to X.509 standard and key pairs

are encrypted with a 3072bit RSA algorithm. The SSL encoded configuration string is 'TLS_ECDHE_RSA_WITH_AES_128_CBC_SHA' [15, 21].

JSecureSync does not perform any kind of analysis on the file to be transmitted. It only synchronises all files in a specific folder (between client and server), providing a trusted isolated server disk quota to every client.

Before sending, every file undergoes a compression. The compression phase can affect both transmission time (heavy compression files are smaller and require lower transmission time) and the required computational load (heavy compression algorithms often require dedicated computational capability).

3.6.3 Orchestrator layer

The middle layer (L2) has been implemented as an abstract object (jFlowOrchestrator) that provides all abstract methods to perform brokerage between L3 and L1, by orchestrating the steps of each request and the server-side computational flow progress. It also provides adaptation for the application layer (L3) data inputs and outputs: different software can run on the application level both on the server and on the client side requiring different file format or data arrangement. For example, as in the case study presented in the following sections, a medical image software could require a remote processing of a medical study. However, it is not required to send all the data to the CAD server (e.g. private information concerning patient name, age, etc. must be dealt with separately). Exploiting the underlying layer (L1) services, the Orchestrator layer (L2) takes charge over the adaptation and coordination of the data flows. The jFlowOrchestrator provides three main abstract methods:

- **bool *fileFilter*(File file)**

This method is used to define which kind of element (including file name, file type, folder, etc) needs to be monitored for changes;

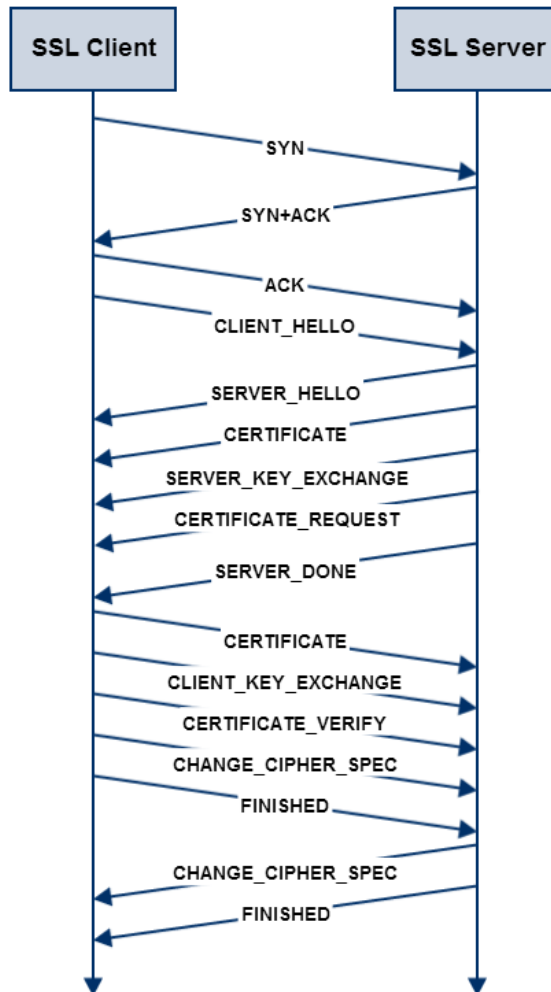


Figure 3.19: SSL Client Authenticated mode timing protocol.

- **bool *serveFileFromPeer*(File file)**

This method is used every time a monitored file is modified by the other peer;

- **bool *serveFileToPeer*(File file)**

This method is used every time a monitored file is modified by the higher (L3) layer.

3.6.4 Application layer

The top layer (L3) has to be implemented according to client side software and server side advanced processing software and tools. Client and server side software must provide a way to implement a communication with L2 layer (over file system) to:

- request a job (client);
- serve a job request (server);
- execute progress synchronisation (client and server);
- provide results (server);
- retrieve results (client).

3.6.5 Orchestrator layer implementation

In medical image analysis context, all abstract methods have been implemented to work on biomedical image data and server processing software: the resulting module is called *jM-FlowOrchestrator*.

In this context, it is worth mentioning that DICOM is the de-facto standard for biomedical images [175]. It is a strongly structured file composed of image row data and patient meta-data used in human and veterinary medicine diagnostic imaging. The DICOM standard supports the handling, storing, printing, and transmission of medical imaging. It includes a file format definition and a network communications protocol. The communication protocol is an application protocol that uses TCP/IP to communicate between

systems. DICOM standard transmission features are intentionally not used with the aim of decoupling proposed architecture effectiveness from any particular application context.

For advanced data processing on the server side, at layer L3, MATLAB [163] (R2013b version) has been chosen because *i*) it requires no special handling of larger sized vector or matrix (images), *ii*) it has advanced ToolBoxes (Image Processing, Parallel and Distributed Computing, Artificial Intelligence) and *iii*) it has the ability to invoke external classification and data mining tools (Fig. 3.22). In particular, some implemented steps of the so far depicted CAD proposal make use of methods to interact with Weka [94] machine learning and data mining suite. This choice makes it possible also to parallelise client request executions by different MATLAB instances, each strongly bound to a specific CPU using MATLAB Parallel Toolbox. It is worth noting that the MATLAB environment has to be installed only on the server-side, while on the client-side the pre-existing software can still be used. According to the DICOM standard the image data can be compressed using a variety of compression standards, including JPEG, JPEG Lossless, JPEG 2000, and Run-length encoding (RLE). In the proposed architecture, signal intensity data is compressed as 4D volume to exploit spatial correlation between near slice of the same time series and temporal correlation between the same slice across different time series. For this reason, the architecture always has a compression stage, independently on the image format used in the DICOM file. This thesis also demonstrates that the format file required by remote processing tools is achieved with the appropriate organisation of the data for a better compression ratio (see Fig. 4.14). For this reason DICOM files, after a suitable processing step, are compressed in MATLAB format. To achieve MATLAB compression without the MATLAB software, the open source Java JMatIO library was used.

On the client side, jM-FlowOrchestrator performs:

- DICOM file analysis to generate two different files: one for volume data ('volume.mat' containing only signal intensity) and one containing only meta-data ('patient.mat' containing only privacy sensible information). Both files are directly stored in MATLAB file format and sent to client by exploiting the potential of the lower layer (jSecureSync);
- Update L3 on the actual processing state (for example, the remaining time) of the requested feature on the server side.

On the server side, jM-FlowOrchestrator performs:

- Data preparation according to the server L3 application layer's required formalism;
- MatLab results, data gathering and transmission to server side L1 layer;
- Client side L2 layer status updating.

Remote processing specifications (both job required and status updates) are memorised in an XML file transmitted over the secure channel together with MATLAB formatted files containing sensitive data. That file is periodically exchanged between client and server.

A single DCE-MRI study can contain as many as 800 DICOM files. Each file represents a single 2D slice and the meta-data DICOM tag about the study and the patient. By exploiting the potentiality of the lower layer (secure and non-secure channel offered by L1), the DICOM files are split. The volume information, extracted from all the DICOM files of the same patient, consists of the 12 bit coded signal intensity for each voxel and is stored in a 4D matrix. Stripped of all sensitive information, it can be sent over the non-secure channel (step 6 of sequence diagram in Fig. 3.20). The meta-data provided by DICOM format normalised (often with a high internal redundancy and with information that is not strictly necessary for the purpose of processing) and compressed (in MATLAB format) are prepared to be

transmitted over the secure channel (step 9 of the sequence diagram in Fig. 3.20). All compression tests on patient data were performed considering both meta-data and signal intensity as 4D volume. Results show as MATLAB achieves a better Compression Ratio (CR) than the Zip4j protocol (the runner-up), exploiting the spatial and temporal correlation typical of DCE-MRI images, and the MATLAB “sparse-matrix” data representation. For those reasons, MATLAB compression is chosen at the middle level (L2 – jM-FlowOrchestrator) only for the DICOM content (both on images and meta-information). Other file types (XML) are compressed using Zip4j protocol to preserve their human-readability.

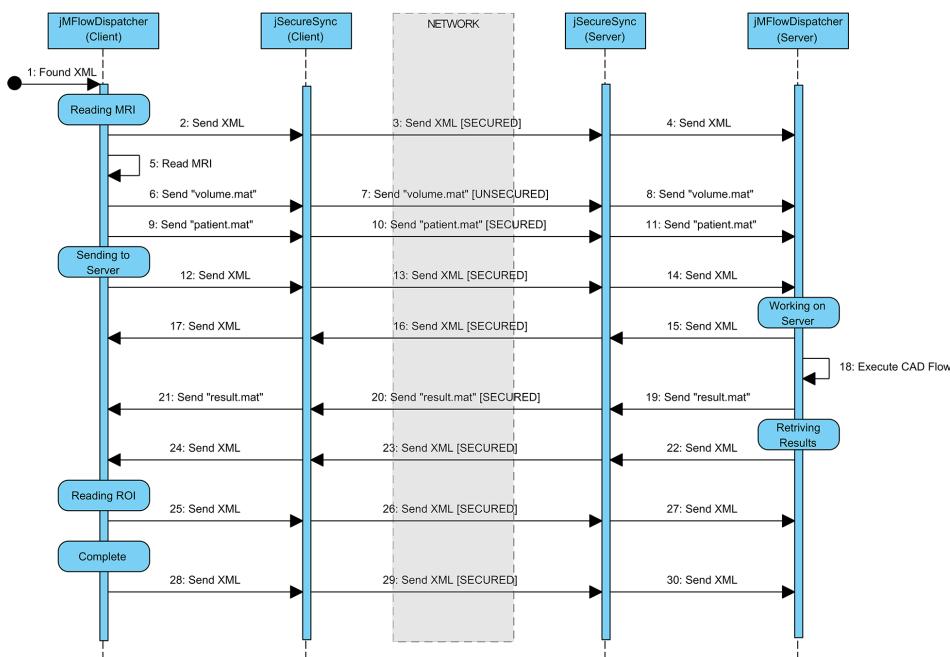


Figure 3.20: Component level sequence diagram for a single job request execution. Rounded rectangles on temporal line represent state changing.

The component level sequence diagram in Fig. 3.20 shows the message passing protocol sequence in the described context for a flow execution scenario:

- Rounded rectangles over the temporal line represent state changing;
- Intra layer communication (a different layer on the same machine) is performed by using file system services;
- Inner layer communication (same layer on a different machine) is performed through communication channel provided by L1 layer.

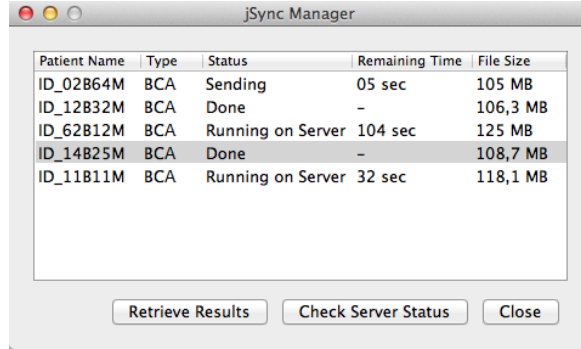
3.6.6 Application layer implementation

On the client-side, the widespread OsiriX medical image tool [218] was chosen, due to its powerful interface and since it has an open plug-in system.

In particular, an OsiriX plug-in capable of interacting with jM-FlowOrchestrator (using the file system) is developed, to give the end-user the ability to:

- Export selected patient DICOM files to jM-FlowOrchestrator;
- Use GUI for required operation on server side, with the possibility to change any parameter;
- Progress display for each required operation;
- Import obtained results from jM-FlowOrchestrator and view them by using the powerful OsiriX interface.

The plug-in allows the user to send patient's data (selecting the required operation), to check in-service operation (with an estimation of the remaining time) and to gather the results. On the arrival of the results, the system alerts the user by means of a pop-up. Clicking the 'Retrieve Results' button (Fig. 3.21), the OsiriX 3D viewer interface is loaded and the results are shown (in this case, the automatically detected lesions).



Patient Name	Type	Status	Remaining Time	File Size
ID_02B64M	BCA	Sending	05 sec	105 MB
ID_12B32M	BCA	Done	-	106,3 MB
ID_62B12M	BCA	Running on Server	104 sec	125 MB
ID_14B25M	BCA	Done	-	108,7 MB
ID_11B11M	BCA	Running on Server	32 sec	118,1 MB

Retrieve Results Check Server Status Close

Figure 3.21: OsiriX GUI example showing how the user can check the status of each job and can retrieve results within OsiriX main window.

On the server side, an advanced modular system for the waterfall execution of any job flow (made up of subsequent steps) called *MatlabFlowManager* is developed. Many simple modules can be combined to form a more complex system easily through a simple XML flow configuration file. The XML configuration file contains the modules internal settings and the modules interconnection settings. The CAD proposal presented in this thesis is used as server side algorithm to be executed via the proposed framework. The final layout of the architecture, with all the chosen applications both on the client side and on the server side, is depicted in Figure 3.22.

The DCE-MRI data segmentation flow processing defined, in accordance with BLADeS, is achieved by means of the followings steps:

- 4D volume extraction from patient DICOM images;
- BreastMask extraction (a binary mask representative of voxel belonging to breast parenchyma, excluding background, bone, skin and pectoral muscles voxel);
- Motion Correction
- Lesion Segmentation (using weka [94] and libsvm [33] packages).

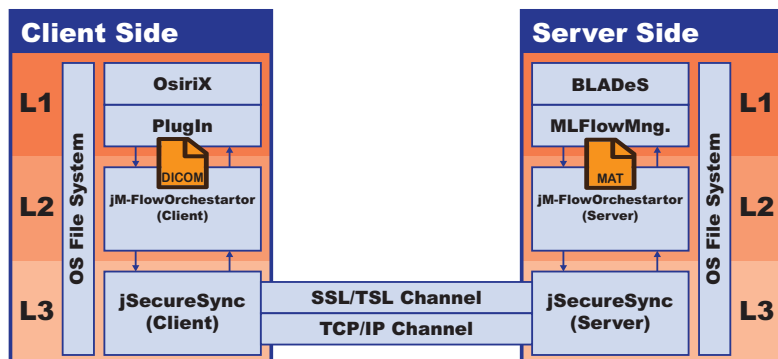


Figure 3.22: The proposed architecture in the specific context of DCE-MRI evaluation, by using OsiriX and a previously proposed CAD tool (BLADeS [159, 200]).

- Lesion Diagnosis (using weka [94])

Each step is obtained using one or several modules developed in MATLAB.

3.6.7 Architecture behaviour

To better understand the whole architecture, a step-by-step scenario of the medical context is presented.

The physician loads the patient DCE-MRI data (from the local files or from the clinical PACS server) into OsiriX; then loads the installed plug-in, selects the remote required task in a drop-down menu (in that case, the name of the remote task that implements BLADeS on the server was ‘BCA’ - ‘Breast Cancer Analysis’) and starts a new remote job request. The plug-in takes into account the DCE-MRI data as a whole and copies the DICOM files into the specific folder of the Java client side of the architecture by creating a new sub-directory named with a new unique ID. Finally, the plug-in also creates an XML file containing the required remote job, and the status ‘Reading MRI’. The folder monitor daemon, implemented into jM-FlowOrchestrator (L2),

catches the XML file (step 1 of Fig. 3.20) and acquires the DICOM files (step 5 of Fig. 3.20) by creating two different files in the MATLAB format: one file ('volume.mat') containing the whole 4D volume of the DCE-MRI image data without any patient information or any kind of private data, and one file ('patient.mat') containing the sensitive data (such as patient name, age, height, weight, etc.). jM-FlowOrchestrator (L2) saves each of these files (the XML file - step 2 of Fig. 3.20 - and the 2 MATLAB formatted file - steps 6 and 9 of Fig. 3.20) into the folder of the lower level (L1 - jSecureSync), marking the XML and the 'patient.mat' file as secure and 'volume.mat' as non-secure. The folder monitor daemon, implemented into jSecureSync (L1), as in the upper level, catches that files and transmits over the right channel (either secure or non-secured) previously instantiated with the server side according to the remark of the upper Layer (steps 3, 7 and 10 of Fig. 3.20).

On the server side, the jSecureSync (L1) module receives all three files and moves them to the upper level folder (steps 4, 8 and 11 of Fig. 3.20). Into the jM-FlowOrchestrator (L2) server module, unlike what is performed on the client side, no specific operation is performed but simply the files are moved from the lower transmission level to the upper application level starting the required task (in the specific context the CAD segmentation workflow - step 18 of Fig. 3.20).

Each status update is performed by updating the XML file and re-syncing it between the peers. For example, once the jM-FlowOrchestrator (L2) server module starts the workflow execution, the status into the XML changes into 'Working on Server' and the folder monitor daemon of each level provides to move the XML file through each level and, of course, between peers (steps 15, 16 and 17 of Fig. 3.20). Each GUI refresh shows the punctual status of each job request (Fig. 3.21).

Once the required task is completed, the result is saved on the server side (into MATLAB format) and, with the same strategy of the client-to-server communication, is moved to the client side (steps 19, 20 and 21 of Fig. 3.20)

where jM-FlowOrchestrator (L2) performs a conversion from the MATLAB format to the XML format. It is then ready to be retrieved into the OsiriX software upon user request.

Furthermore, once the GUI receives an XML file containing the status ‘Retrieving Results’, it alerts the user with a pop-up message.

With respect to the execution time, the whole architecture, therefore, only adds the time needed to transmit files and adapt data formats from client to server and vice-versa. Transmission times include: time needed to adapt data from both applications layers; compression and decompression times and the actual sending time via TCP or SSL channels. In the performance assessment, we also focused on how much the architecture impacts the execution time by evaluating the overhead percentage.

3.6.8 Exploit Parallelism

For the specific case study, the automated CAD proposal in breast DCE-MRI deployed on the server side, is not yet ready to be directly parallelised. On the other hand, the architecture is able to schedule different executions of the same CAD elaboration, one for each request. Each MATLAB instance is bound to a single job request and to a specific CPU with the aim to improve the local performance. In this way, the architecture is able to increase the overall system throughput, and also the one of a not parallelised service. The jM-FlowOrchestrator (L2) together with MatlabFlowManager (L3) takes care of the binding with the local CPUs or the dispatching of the job to a least busy server, exploiting the parallelism in a clustered manner too.

Experimental Results

In this chapter will be illustrated the datasets used for the evaluation, then, will be presented the chosen evaluation criteria to carried out the test and finally the results of each proposed approach. Moreover, where possible, a comparison with some literature proposals is performed.

To obtain a fair generalisation performances evaluation, a cross-validation (CV) is required. Among the different CV techniques, Leave-one-Out CV (LoO-CV) provides a pretty good approach by training the model on all the dataset except for one observation (feature-set) and by testing on this observation. In this thesis, some modules extract different feature observations for each patient, therefore, it is mandatory to validate the model by avoid mixing intra-patient observations. A LoO-CV on a patient basis is, then, performed obtaining a Leave-one-Patient-Out Cross-Validation (LoPO-CV).

Each module has been evaluated by a LoPO-CV approach, and results show a confidence level of 95% ($p < 0.05$).

All the results are here presented without any remark. A detailed discussion with some remarks, are reported in chapter [5](#).

4.1 Datasets

All the tests are performed on real Dynamic Contrast-Enhanced Magnetic Resonance Imaging (DCE-MRI) data coming from different sources.

Thanks to the partnership with "Istituto Nazionale Tumori IRCCS - Fondazione G.Pascale", a national institution devoted to study and care of tumours and, with the collaboration of Antonella Petrillo, MD and Roberta Fusco, PhD, we collected and analysed up to 42 patients (average age 40 years, in range 16-69) with breast DCE-MRI (in order to simplify, this dataset will be referred by the name 'DSpascale42'). All subjects showed histopathologically proven lesions. MRI images are recorded with a 1.5 T scanner (Magnetom Symphony, Siemens Medical System, Erlangen, Germany) equipped with breast coils. Per each subject, 10 series of DCE T1-weighted images (80 slices each) have been acquired with parameters reported in Table 4.2. One series (t_0) was acquired before and 9 series (t_1 - t_9) after intravenous injection of Gadolinium-diethylene-triamine penta-acetic acid (Gd-DOTA, Dotarem, Guerbet, Roissy CdG Cedex, France). Injection has been performed via an automatic system (Spectris Solaris EP MR, MEDRAD, Inc., Indianola, PA); Dose: 0.1 mmol/kg; Injection flow rate: 2 ml/s and followed by a flush of 10 ml saline solution.

The dataset also contains the following ground-truth: the segmentation of breast tissues and a voxel-by-voxel segmentation of all the suspicious nodules (both benignant lesions and malignant tumours). Moreover, the histopathologically proven malignity has been reported for each lesion (19 benign lesions and 23 malignant) as reported in the table 4.1.

The available ground truth for the first depicted dataset is sufficient to validate the breast segmentation, the lesion segmentation and the lesion classification modules. All the information about the follow-up of the patients are not available for this dataset.

With the aim of also validate the follow-up module, others dataset have been considered in this thesis. Two public sources have been used and fused

Benignant Lesions	
— Fibroadenoma	12
— Fibrocystic Dysplasia	3
— Not Defined	4
<hr/>	
	19
Malignant Lesions	
— Ductal	2
— Infiltrating Ductal	9
— In Situ Ductal	3
— Infiltrating Lobular.	2
— Infiltrating Ductal-Lobular	2
— Not Defined	5
<hr/>	
	23

Table 4.1: Lesions details for the private dataset ‘DSpascale42’.

to obtain a bigger set of 226 patients only composed by malignant lesions but complete of the ground truth about the follow-up endpoint.

During neoadjuvant chemotherapy for breast cancer analysis, three DCE-MRI scans were scheduled for all patients in the ensemble: MRI_1 before treatment; MRI_2 after one cycle of chemotherapy; MRI_3 after completion of Anthracycline treatment and before surgery or further treatment. Subjects receiving Taxane were scheduled for an additional exam, MRI_4 , after completion of all chemotherapy treatment and before surgery (see Figure 2.7).

The first public dataset [41, 182] of this ensemble is composed of 64 patients (in order to simplify, this dataset will be referred by the name ‘DSpublic64’). MRI images are recorded with 1.5 T scanner (Signa, GE Healthcare, Milwaukee, WI) using a phased array breast coil. Per each subject, 10 series of DCE T1-weighted fat-suppressed images (different number of slices each) have been acquired unilaterally with parameters reported in Table 4.2.

A minimum of three time points was acquired during each contrast-enhanced MRI protocol: a pre-contrast scan (t_0), followed by 2 consecutive

post-contrast time points: early (t_1) and late (t_2) phases. The gadopentetate dimeglumine contrast agent (Magnevist, Bayer HealthCare, Berlin, Germany), was injected at a dose of 0.1 mmol/kg of body weight (injection rate = 1.2 mL per second) followed by a 10 mL saline flush, with injection starting coincident with the start of the early t_1 phase acquisition. Imaging time was approximately 5 minutes per acquisition, resulting in effective early and late post-contrast time points of 2.5 minutes and 7.5 minutes from the start of the contrast injection, respectively, using standard k-space sampling. Fat suppression was performed using a frequency-selective inversion recovery preparatory pulse.

The second public dataset [41, 112] of the ensemble contains 162 subjects (in order to simplify, this dataset will be referred by the name ‘DSpublic162’). MRI images have been performed on a 1.5T field strength scanner using a dedicated breast radio-frequency coil. All the contrast-enhanced T1-weighted images have been performed unilaterally over the symptomatic breast and in the sagittal orientation. The contrast-enhanced series consist of a high resolution (≤ 1 mm in-plane spatial resolution) three-dimensional, fat-suppressed, T1-weighted gradient echo sequence as reported in the Table 4.2 Scan time length for the T1-weighted sequence was required to be between 4.5 and 5 minutes. The sequence was acquired once before contrast injection and repeated at least twice following injection.

The datasets are used in the following modality: ‘DSpascale42’ has been used to test individually the breast mask extraction, the motion correction, the lesion detection and diagnosis modules. The ‘DSpublic64’ and ‘DSpublic162’ have been used to test the therapy assessment stage as a combined bigger dataset and as training and test (to further validate the proposed approach). Furthermore, the ‘DSpascale42’ was used as a test set for the whole workflow from the breast mask extraction till to the lesion classification with the aim of validating a complete automatic CAD.

	DSpascale42	DSpubic64	DSpubic162
Sequence	FLASH 3D	FLASH 3D	FLASH 3D
Plane	Coronal	Sagittal	Sagittal
Fat Suppression	No	Yes	Yes
Field	1.5 <i>T</i>	1.5 <i>T</i>	1.5 <i>T</i>
TR	9.8 <i>ms</i>	8 <i>ms</i>	≤ 20 <i>ms</i>
TE	4.76 <i>ms</i>	4.2 <i>ms</i>	4.5 <i>ms</i>
FA	25 <i>deg</i>	20 <i>deg</i>	≤ 45 <i>deg</i>
FoV	370x185 <i>mm</i> ²	18-20x18-20 <i>cm</i> ²	16-18x16-18 <i>cm</i> ²
Matrix	256x128 <i>px</i>	256x192 <i>px</i>	≥ 256 x192 <i>px</i>
Pixel Size	1.445 <i>mm</i>	0.70x0.94 <i>mm</i>	≤ 1 <i>mm</i>
Thickness	2 <i>mm</i>	1.4 <i>mm</i>	≤ 2.5 <i>mm</i>
TA	56 <i>s</i>	18.2 <i>s</i>	4.5-5 <i>min</i>

Table 4.2: DCE-MRI acquisition parameters for the different used dataset.

4.2 Evaluation Strategies

With the aim of providing a proper effectiveness evaluation for each stage of the CAD, specific procedures have been developed.

4.2.1 Breast mask and Segmentation evaluation

The breast mask and the segmentation stages provide voxel-by-voxel binary masks as result. To assess the effectiveness of the proposed approaches, the extracted masks are compared with a manually segmented gold-standard by an experienced radiologist. To quantitatively compare obtained masks with respect to the gold-standard, it is possible to consider measures based on True Positive (*TP*), True Negative (*TN*), False Positive (*FP*) and False Negative (*FN*), or regions overlap measures (as in Section 1.3.1 and Figure 1.11).

- **Accuracy:** an overall index for the goodness of segmentation, that considers correctly segmented voxels with respect to all voxels. Accuracy is calculated as: $ACC = (TP + TN) / (TP + TN + FP + FN)$.

- **Sensitivity:** defined as the number of voxels of the gold standard correctly segmented over the total number of voxel of the gold standard mask. It gives information on over-segmentation: a value next to 1 indicates a high precision in recognising the real mask, while values next to 0 indicate an high number of wrong (over) segmented voxels. Sensitivity is calculated as: $SEN = (TP)/(TP + FN)$.
- **Specificity:** defined as the number of voxels correctly segmented as not belonging to the gold standard over the total number of voxel not belonging to the ground truth. It gives information on under-segmentation: a value next to 1 indicates a high precision in recognising voxels outside if the original mask, while values next to 0 indicate an high number of wrong (under) segmented voxels. Specificity is calculated as: $SPE = (TN)/(TN + FP)$.
- **Dice Similarity Coefficient (DSC) [51]:** an overlap measure used to compare the similarity between the Gold Standard (GS) volume and the automatic segmented (SEG) one. DSC is calculated as: $DSC = (2 \cdot n(GS \cap SEG))/(n(GS) + n(SEG))$, where $n(\cdot)$ represents the number of voxels in the enclosed volume.

To statistically validate results, a leave-one-patient-out approach was used.

4.2.2 Motion Correction Quality Index evaluations

Reference Ranking

In order to compare the performance of the different Quality Indexes (QIs) the following approach is proposed. First, a ‘reference ranking’ of the Motion Correction Techniques (MCTs) is determined. Subsequently, each QI has been used to provide a ranking of the MCTs. Finally, the QI that provides the ranking most similar to the reference one is selected.

The reference ranking has been achieved exploiting the *a posteriori* accuracy of the tumour segmentation for each subject. The segmentation is achieved with the lesion detection module of the proposed CAD. The accuracy has been calculated with respect to a manual, voxel-by-voxel, segmented Region of Interest (ROI).

According to the Figure 4.1 a flow of the first three stages was implemented to produce the reference ranking and for the comparison patient-by-patient. The lesion detection accuracy has been used for ranking of the MCTs for each patient.

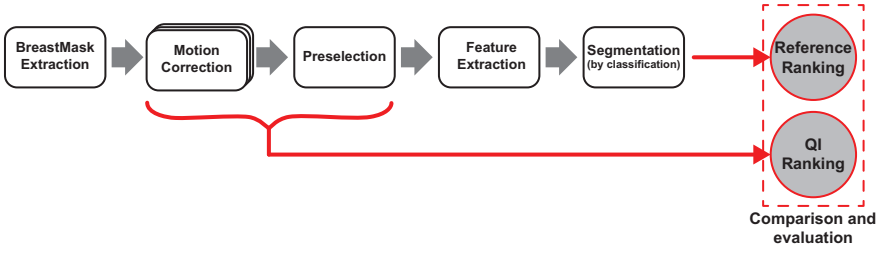


Figure 4.1: Processing flow for ‘reference ranking’ and assessment strategy. In order to rank different MCTs, the first tree module of the CAD has been used. Each MCT was assigned a rank on the basis of the agreement between the CAD segmented Region of Interest (ROI) with a manual ROI. Subsequently, the ranking of different MCTs was compared with the ranking obtained by means of the QI.

Comparison among rankings

The effectiveness of each QI was evaluated by extracting and comparing the Spearman rank correlation coefficients (S-RCC). This coefficient has been evaluated comparing the ranking provided by each QI with respect to the ‘reference ranking’ (Figure 4.1) according to the following:

$$\text{S-RCC} = 1 - \frac{6 \sum d_i^2}{n(n^2 - 1)} \quad (4.1)$$

where d_i is the element-wise difference between ranks and n is the number of rank positions.

4.2.3 Remote Architecture evaluation

With the purpose of assessing the proposed architecture for remote execution of the so far designed protocols, the following tests have been executed.

Data compression tests

Different compression protocols have been compared: Java Native Zip library, Lempel-Ziv-Markov (LZMA), the Zip4j open source library and MATLAB file format compression. The Zip4j library has been chosen due to its large diffusion. It provides several levels of compression (0. Store, 1. Fastest, 3. Fast, 5. Normal, 7. Maximum, 9. Ultra) requiring different times. Of course, the compression ratio and compression times affect the transmission times. Therefore, in order to choose the optimal compromise between compression ratio and the overall transmission time, several compression levels have been tested evaluating the Compression Ratio (CR) as in the equation 4.2:

$$CR[\%] = \left(1 - \frac{\text{compressed size}}{\text{original size}} \right) \cdot 100 \quad (4.2)$$

As the DICOM files include private information that must be sent on the secure channel (see Section 3.6.2), the compressed DICOM images have not been sent. Instead, the Orchestrator layer (see Section 3.6.3) extracts meta-information, sending it only one time for each patient, before signal intensity 4D data. This has the advantage of not sending the same information multiple times, i.e. the patient meta-data.

Transmission and Execution tests

The total execution times, made up of both transmission times (from client to server and vice-versa) and the server computational time, have been compared to evaluate transmission and execution times.

The transmission time includes all the operations required by the proposed architecture (such as the compression/decompression time or the time needed to adapt data from both application layers) to move the execution of the required job from a local context to a remote environment.

Moreover, the Overhead (OH) has been calculated according to the equation 4.3.

$$OH[\%] = \frac{TransmissionTime}{TransmissionTime + ExecutionTime} \cdot 100 \quad (4.3)$$

Scalability test

To evaluate performance and feasibility of the proposed system, local execution vs. remote server execution has been evaluated. The total execution time (constituted by client-to-server transmission time, server processing time, server-to-client transmission time) in the client-server architecture is compared with the time needed by the same operation when it is entirely performed on physician's workstation.

Scalability has been tested by evaluating the system throughput (number of produced output per time unit, considered as the number of results produced by the system in one hour under a huge load regime) in four different configurations:

- Local: job is entirely performed on the radiology workstation;
- 1 CPU: job is performed through server using one CPU;
- 2 CPUs: job is performed through server using two CPUs;
- 4 CPUs: job is performed through server using four CPUs.

Throughput is defined in eq.4.4 (for the local configuration) and in eq.4.5 (for the remote configurations) and the unit of measurement is: $\frac{jobs}{h}$.

$$TP_{local} = \left(\frac{1hour}{single_job_execution_time} \right) \quad (4.4)$$

$$TP_{server} = \left(\frac{1hour}{single_job_execution_time} \right) \cdot \#CPU \quad (4.5)$$

For each remote configuration, the speed-up has been calculated according to eq.4.6 as proposed in [101].

$$speedup = \frac{TP_{remote}}{TP_{local}} \quad (4.6)$$

4.3 Pre-processing Phases

In this section, the results of Breast Mask extraction and motion correction are reported. The motion correction module performs a data-drive motion correction techniques (MCTs) selection.

4.3.1 Breast Mask Extraction

To verify the effectiveness of each step which composes the proposed breast masking extraction approach, Table 4.3 compares the performance obtained by applying all the breast mask extraction stages versus those obtained by using only a Fuzzy C-Means clustering (stages 1 and 3) and those obtained by all stages but the post-processing refinements. The reported results confirmed that the use of all stages gives rise to the best performance.

The tables 4.4 and 4.5 compares the results of the proposed approach with those obtained by using our implementation of the algorithms described in section 2.1.1. Both tables report the median values over 42 patients ('DSpace42') of *ACC*, *SPE*, *SEN* and *DSC*, while table 4.5 also shows lesion

Stages	ACC [%]	SPE [%]	SEN [%]	DSC [%]
1,3	95.83 (± 0.60)	74.65 (± 3.85)	99.41 (± 0.04)	81.94 (± 4.30)
1,2,3	96.75 (± 0.39)	86.88 (± 2.62)	98.59 (± 0.23)	87.55 (± 2.68)
All	97.56 (± 0.42)	95.67 (± 1.11)	98.12 (± 0.41)	91.36 (± 1.49)

Table 4.3: Performance comparison among different combination of proposed breast mask extraction method stages. The table shows median values over 42 patients ('DSpascale42') with the corresponding 95% confidence intervals.

coverage (minimum, maximum and average value over 42 patients) and execution times.

As it is evident, the proposed method obtained the best results, with an accuracy and dice similarity index of 97,56 ($\pm 0,42$) and 91,36 ($\pm 1,49$) respectively. Moreover, it produces a breast mask that always includes neoplastic lesion (with a coverage of 100% in all considered patients), even when located across pectoral muscle or under the armpit cavities.

Method	ACC [%]	SPE [%]	SEN [%]	DSC [%]
Our Proposal	97.56 (± 0.42)	95.67 (± 1.11)	98.12 (± 0.41)	91.36 (± 1.49)
Wu et al.[267]	88.41 (± 2.50)	96.07 (± 0.76)	89.18 (± 3.24)	68.96 (± 10.46)
Fooladivanda et al.[68]	87.57 (± 2.97)	87.43 (± 5.36)	88.10 (± 4.02)	65.40 (± 10.32)
Lu et al.[151]	86.20 (± 3.03)	87.14 (± 3.07)	87.05 (± 3.97)	63.41 (± 7.80)
Vignati et al.[252]	82.40 (± 1.13)	99.90 (± 0.25)	79.29 (± 1.32)	60.32 (± 3.57)
Goshal et al.[84]	80.10 (± 2.68)	98.70 (± 0.28)	77.60 (± 2.63)	58.80 (± 7.74)

Table 4.4: Comparison of the breast mask extraction proposed approach with some literature proposals (1/2). The table shows median values obtained in Leave-one-Patient-Out over 42 patients ('DSpascale42') with the corresponding 95% confidence intervals.

Finally, figure 4.2 shows an image for each of the four stages of the proposed method, describing the key characteristics, while figure 4.3 shows the final extracted 3D breast mask.

Method	Lesion Coverage [%]			Exec. Time [s]
	Min	Max	Avg	
Our Proposal	100.00	100.00	100.00	81.01 (± 0.00)
Wu et al.[267]	0.00	100.00	94.95	196.90 (± 6.97)
Fooladivanda et al.[68]	21.71	100.00	85.31	more than 1h
Lu et al.[151]	11.37	100.00	90.68	227.12 (± 5.07)
Vignati et al.[252]	100.00	100.00	100.00	3.97 (± 0.05)
Goshal et al.[84]	96.20	100.00	99.86	88.16 (± 1.04)

Table 4.5: Comparison of the breast mask extraction proposed approach with some literature proposals (2/2). The table shows median values obtained in Leave-one-Patient-Out over 42 patients (‘DSpascale42’) with the corresponding 95% confidence intervals.

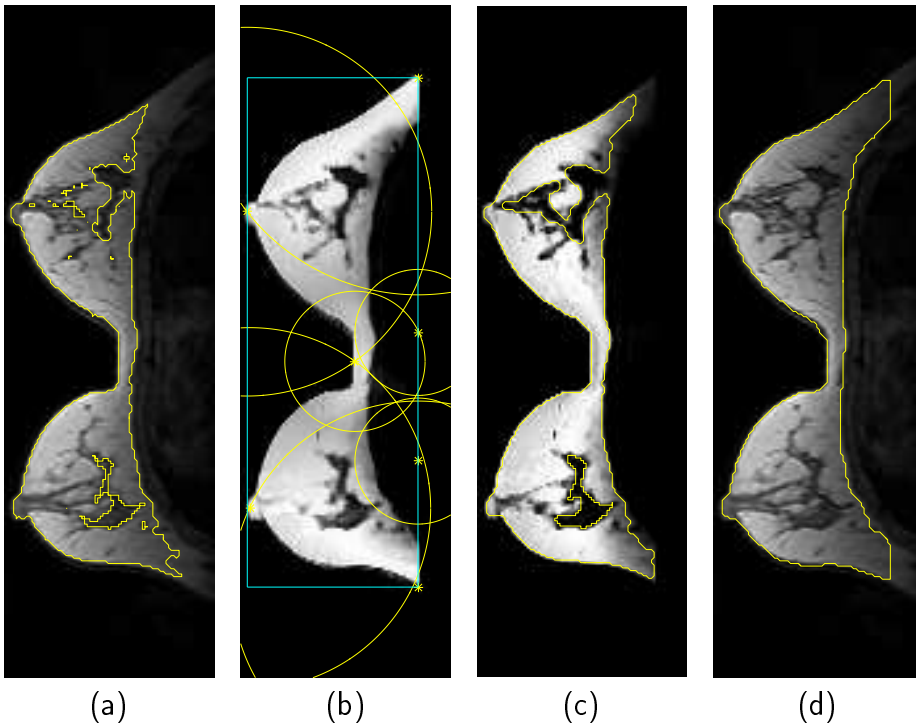


Figure 4.2: Breastmask extraction stage by stage results (in transversal projection). (a) Basic Otsu's segmentation: the armpit cavities were not included. (b) Grey level representation of the weighted combined class membership, with geometrical key-points and their pertinence sphere (yellow points and circles). In cyan the cuboid boundaries. (c) Segmentation of the weighted combined class membership. (d) Final mask segmentation, over the real data, after post-processing refinements. It is worth noticing how armpit cavities breast parenchyma was correctly included and hole were filled.



Figure 4.3: Final 3D reproduction of breast mask extracted with the proposed approach.

4.3.2 Data Driven MCT Selection

The table 4.6 shows the ‘Reference Ranking’ evaluated for each of 30 subjects (a subset of ‘DSpascale42’) over all the MCTs and used to produce the final assessment of the proposed Quality Index (QI) in choosing the best motion correction technique (MCT).

The table 4.7 presents the performances of all the QIs introduced in the Section 3.1.2. The ranking of each patient obtained with each QI is compared to the reference ranking (see table 4.6) in terms of Spearman (S-RCC) rank correlation coefficient. The median values are reported.

In the last section, a sampling strategy is applied with the aim of improving the performance of the QI (*ETK-P* - see table 4.7) evaluation. By varying the percentage of the whole volume in the range from 100% to 0% with a step of 0.01%, the median value over the Monte Carlo simulation (100 iterations) is evaluated. The results are presented in fig. 4.4.

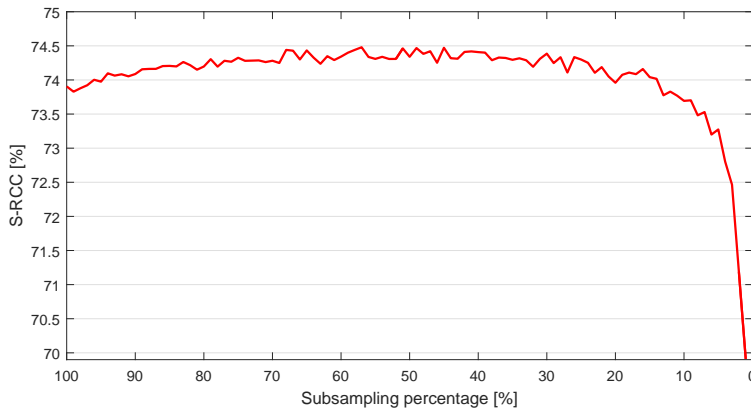


Figure 4.4: Result of sub-sampling strategy in terms of S-RCC over the sampling percentage.

The sub-sampling approach is able to reduce the computation time of the QI from about 15 hours to 30 minutes (by using a percentage of 15%) without affecting the global performances.

Finally, with the aim of assessing the effectiveness of QI for the problem of selecting the best MCT tailor for the patient, the hit-rate is calculated by varying the sampling percentage. The hit-rate is obtained by comparing, for each patient, the first rank provided by the QI with the ‘reference ranking’. The results on the Monte Carlo simulation (100 iterations) provide the hit-rate (fig. 4.5).

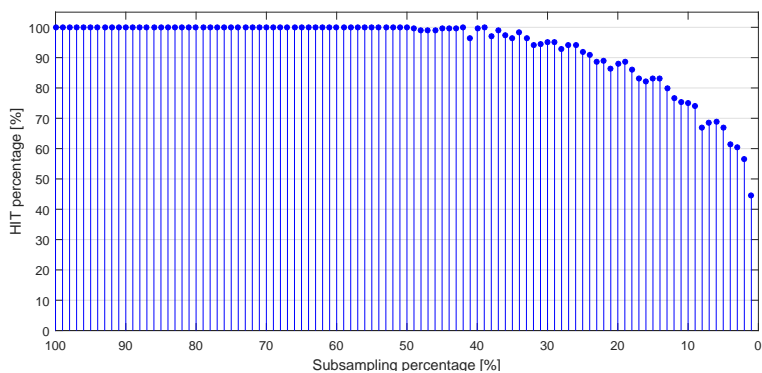


Figure 4.5: Hit percentage over the sampling percentage.

Patient	NO	ML	MEDx3	MEDx5	R_AC	R_AL	R_BC	R_BL	ElastiX
p01	9	7	4	1	6	5	3	8	2
p02	2	5	6	1	4	4	8	7	3
p03	5	4	3	9	6	1	8	7	2
p04	2	4	6	7	5	3	4	9	1
p05	4	5	2	1	4	6	7	8	3
p06	2	9	4	1	5	7	8	6	3
p07	2	1	5	3	7	8	6	9	4
p08	3	4	1	2	4	4	7	6	5
p09	8	5	2	3	6	7	4	9	1
p10	9	4	1	2	3	5	6	8	7
p11	4	6	3	2	7	8	5	9	1
p12	4	2	1	1	2	2	2	5	3
p13	6	5	7	8	1	4	2	9	3
p14	6	8	4	1	3	2	7	9	5
p15	3	3	2	1	2	2	3	4	2
p16	6	7	4	1	2	3	7	8	5
p17	4	6	3	1	8	5	7	9	2
p18	4	6	2	1	5	7	3	9	8
p19	8	4	3	1	6	7	6	5	2
p20	4	5	9	3	2	1	6	8	7
p21	7	6	1	6	2	3	9	8	5
p22	4	7	2	1	6	3	9	8	5
p23	2	5	3	2	5	4	6	7	1
p24	5	7	2	1	6	4	3	9	8
p25	5	3	4	2	2	6	7	8	1
p26	4	7	2	1	6	2	5	8	3
p27	4	6	2	1	8	7	5	9	3
p28	3	4	2	1	7	5	8	9	6
p29	4	1	2	3	1	2	2	4	1
p30	6	7	1	2	4	5	3	8	9
median	4	5	2.5	1	5	4	6	8	3
mode	4	4	2	1	6	2	7	9	3

Table 4.6: Reference ranking. For each subject (row) the rank (with respect to the CAD accuracy results) of each MCT is reported. It is worth to note that although the median filtering approach (MEDx3 and MEDx5) achieve, in general, better results with respect to other MCTs, no single MCT is always in the first rank position for all the subjects.

QI	S-RCC
R-MSE	6.90%
PSRN	13.56%
N-CC	18.26%
HB	31.31%
GCTT	51.15%
TK-W	55.95%
TK-P	59.17%
ETK-W	58.33%
ETK-P	73.91%
MIX-MIN	66.67%
MIX-MEAN	64.17%
MIX-MAX	61.67%
MIX-MEDIAN	60.35%

Table 4.7: Comparison among QIs. The Spearman (S-RCC) rank correlation coefficients have been calculated per each subject by comparing the ranking produced by each QI (in the rows) with the ‘reference ranking’ (in table 4.6). Median values over 30 patients (a subset of ‘DSpascale42’) are reported.

4.4 Lesion Detection

The figure 4.6 shows (in red) a manually segmented ROI (the gold-standard) over the pre-contrast DCE-MRI image.

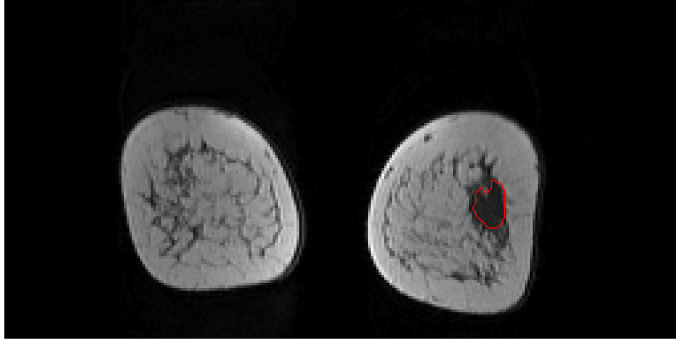


Figure 4.6: DCE-MRI slice in a pre-contrast image with a manual selected ROI (in red).

The figures 4.7 and 4.8 summarises the results produced by each step of the proposed method for a benignant lesion and for a malignant lesion respectively.

The table 4.8 reports the results of the evaluation study with and without motion correction and pre-selection phase, and by varying the classifier. For each combination, the table reports the mean value (evaluated on a leave-one-patient-out basis) of sensitivity, specificity and accuracy, in decreasing order of accuracy.

To further validate the detection approach, table 4.9 reports an evaluation on a bigger dataset of 42 patients (the whole ‘DSpascale42’ dataset). In this table only the Motion Correction varies; the pre-selection is always applied and Support Vector Machine (SVM) is used. Moreover, more Motion Correction techniques have been tested: Affine deformations, Free Form Deformation (FFD) with cubic or linear interpolation and Elastix [122], an open source software for intensity-based medical image registration. All the

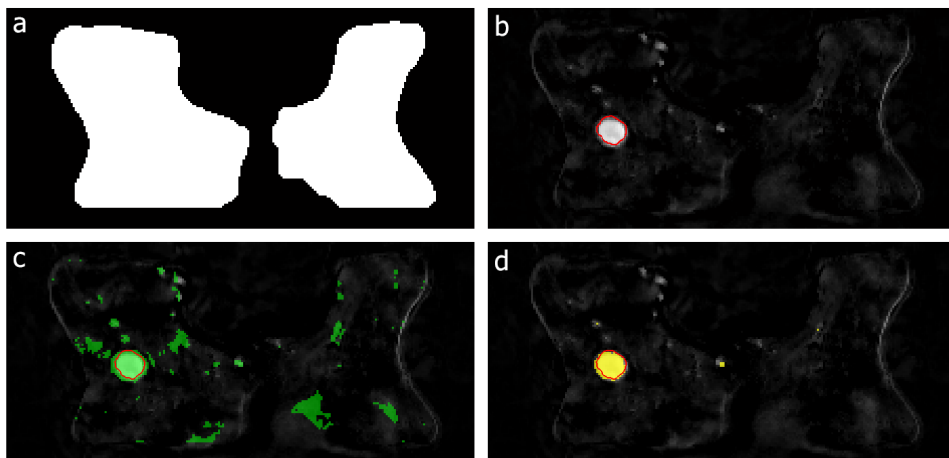


Figure 4.7: Detection results on a benign lesion: a) Brest-mask; b) Manual ROI lesion segmentation (red perimeter); c) Pre-selection mask (green area); d) automatic detected ROI (yellow area).

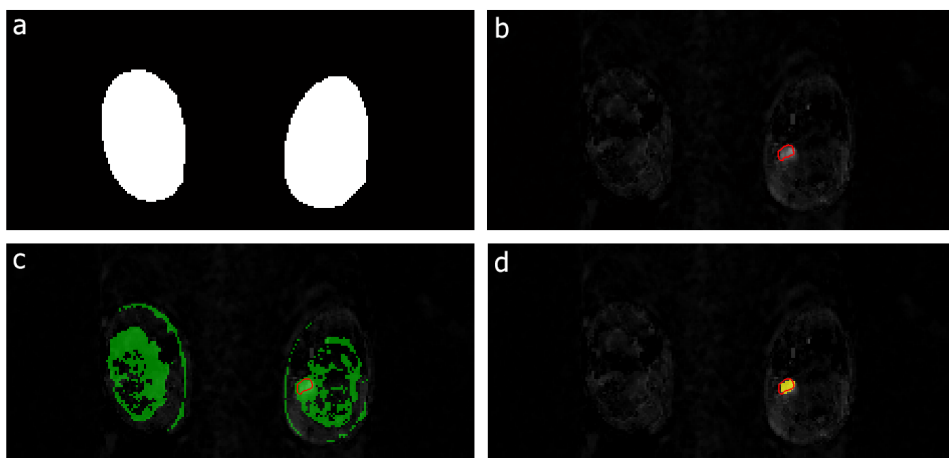


Figure 4.8: Detection results on a malignant lesion: a) Brest-mask; b) Manual ROI lesion segmentation (red perimeter); c) Pre-selection mask (green area); d) automatic detected ROI (yellow area).

Motion Correction	Pre-Selection	Classifier	ACC [%]	SEN [%]	SPE [%]
Median (3px)	Yes	SVM	98.70	71.56	98.94
Median (3px)	Yes	RF	98.65	67.78	98.95
Median (3px)	Yes	MLP	98.63	72.82	98.85
Rigid Reg.	Yes	SVM	98.57	67.13	98.85
Rigid Reg.	Yes	MLP	98.48	68.79	98.74
Rigid Reg.	Yes	RF	98.40	64.19	98.70
None	Yes	SVM	98.39	69.82	98.66
None	Yes	RF	98.31	65.92	98.62
None	Yes	MLP	97.87	72.61	98.13
Median (3px)	No	RF	95.07	90.81	95.10
Median (3px)	No	SVM	94.75	92.74	94.75
Rigid Reg.	No	RF	94.28	90.19	94.30
None	No	RF	94.19	90.74	94.21
Rigid Reg.	No	SVM	94.00	91.20	94.00
Rigid Reg.	No	MLP	93.97	92.18	93.98
None	No	MLP	93.75	90.65	93.76
Median (3px)	No	MLP	93.73	92.82	93.71
None	No	SVM	93.61	91.08	93.61

Table 4.8: ROI detection performance. Median values obtained in Leave-one-Patient-Out over 26 patients (a subset of ‘DSpascale42’) are reported. In each row, a different motion correction, classifier and pre-selection are presented.

results in the tables have been demonstrated to be statistically significant different ($p < 0.05$).

Table 4.10 reports the best result for lesion detection compared with other methodologies: a pixel-based approach proposed by Torricelli2003 et al. [244], another proposal based on dynamic features and MLP classifier [72], and a pixel-based approach based only on thresholding the Relative Enhancing (RE) (which is, indeed, our pre-selection methodology as described in the

Motion Correction	ACC [%]	SEN [%]	SPE [%]	AUC [%]
Median (3px)	95.71	82.72	96.06	85.15
None	93.96	77.96	94.82	85.21
Affine (w. Cubic Interp.)	93.75	80.30	94.94	85.36
Affine (w. Linear Interp.)	93.72	80.53	95.10	85.47
Rigid Reg.	92.86	77.52	94.57	86.65
Elastix	92.77	85.27	94.04	84.99
Median (5px)	92.40	83.09	94.45	83.63
FFD (w. Cubic Interp.)	91.70	79.97	93.03	84.32
FFD (w. Linear Interp.)	79.00	49.02	80.43	63.38

Table 4.9: ROI detection performance. Median values obtained in Leave-one-Patient-Out over 42 patients (‘DSpascale42’) are reported. In each row, the influence of different motion corrections are evaluated.

section 3.2.1). All the results in the tables have been demonstrated to be statistically significant different ($p < 0.05$).

Methodology	ACC [%]	SEN [%]	SPE [%]	AUC [%]
Proposed Methodology	95.71 (± 0.02)	82.72 (± 0.03)	96.05 (± 0.02)	89.39 (± 0.02)
Torricelli et al. [244]	94.13 (± 0.02)	41.32 (± 0.03)	89.45 (± 0.02)	65.39 (± 0.03)
Fusco et al. [72]	84.23 (± 0.03)	90.24 (± 0.02)	82.88 (± 0.03)	86.56 (± 0.02)
Pixel-Based on RE	81.23 (± 0.03)	85.56 (± 0.03)	82.45 (± 0.03)	84.01 (± 0.02)

Table 4.10: Performance comparison of the proposed method with other approaches. Median values obtained in Leave-one-Patient-Out over 42 patients (‘DSpascale42’) are reported.

In order to better analyse the results, figures 4.9 and 4.10 compare the automatic segmented region obtained for a benign and a malignant lesion, respectively, by using the approaches reported in table 4.10. In this case, the advantage of using the lesion detection module, proposed in this thesis, appears even more evident.

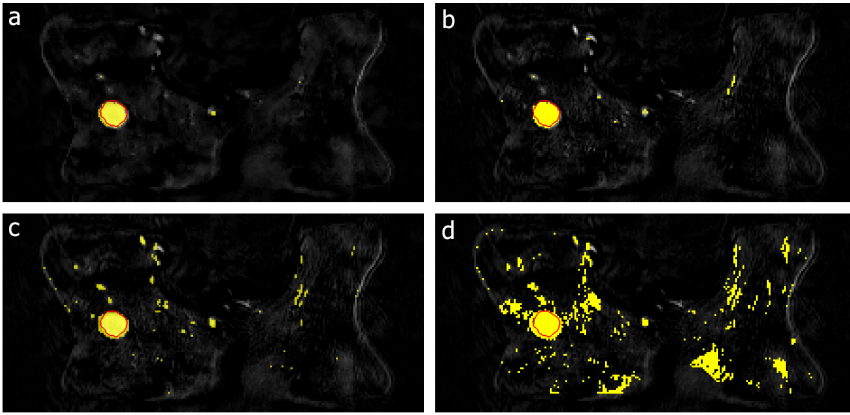


Figure 4.9: Comparing lesion detection results for a benign lesion: a) our proposed approach; b) the pixel-based approach by [244]; c) the MLP-based approach by [72]; d) pre-selection mask.

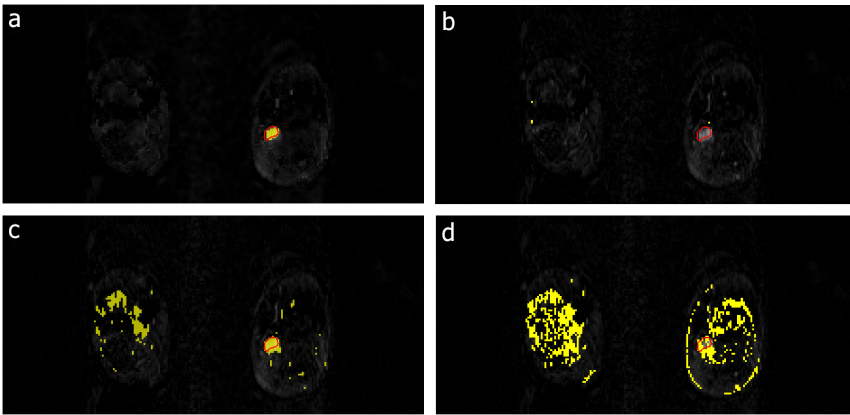


Figure 4.10: Comparing lesion detection results for a malignant lesion: a) our proposed approach; b) the pixel-based approach by [244]; c) the MLP-based approach by [72]; d) pre-selection mask. Note that in this case b) was not able to detect the lesion.

4.5 Lesion Diagnosis

Figure 4.11 shows the three Local Binary Patterns on Three Orthogonal Planes (LBP-TOP) concatenated histograms extracted for the ROI in Fig.4.6 with a temporal radius 1.

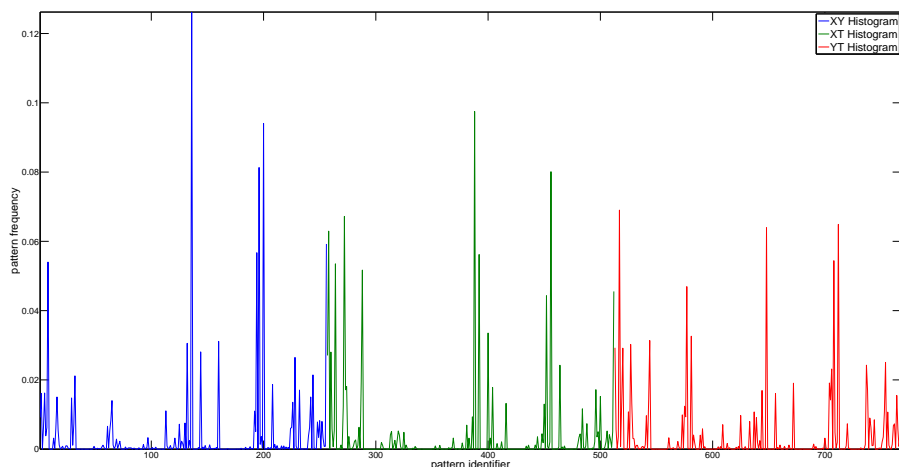


Figure 4.11: LBP-TOP concatenated histograms per each orthogonal plane corresponding to the ROI showed in fig.4.6.

In the Table 4.11 Accuracy, Sensitivity and Specificity per each motion correction technique and classifier have been reported. In all the experiments LBP-TOP feature was extracted using the complete feature-set (ALL). Rows are ordered according to decreasing accuracy (highest on the top row).

For the subsequent analysis, on the basis of Table 4.11, the best combination of classifier and motion correction having the highest accuracy have been selected. In Table 4.12 the performance of such a combination (RF as classifier and median filtering with a 5px windows as motion correction technique) have been assessed with different feature sets as described in Table 3.3.

The table 4.13 reports the comparison between the performance of the lesion diagnosis proposal (first row in Tab. 4.12) and other approaches

Motion Correction	Classifier	ACC [%]	SEN [%]	SPE [%]
Median	RF	80.80	86.70	72.70
No	RF	76.90	80.00	72.70
No	MLP	73.10	93.30	45.50
No	SVM	69.20	100.0	27.30
Median	MLP	61.50	93.30	18.20
Median	SVM	61.50	93.30	18.20

Table 4.11: Lesion diagnosis results per each combination of Motion Correction technique and Classifier. LBP-TOP were evaluated by using the complete feature-set (ALL). Rows are ordered according to decreasing accuracy (highest on the top row). Median values obtained in Leave-one-Patient-Out over 26 patients (a subset of ‘DSpascale42’) are reported.

Feature Set	ACC [%]	SEN [%]	SPE [%]
YT	84.60	80.00	90.90
ALL	80.80	86.70	72.70
XTYT	76.90	80.00	72.70
XY	69.20	80.00	54.50
XYXT	65.40	66.70	63.60
XYYT	61.50	66.70	54.50
XT	57.70	66.70	45.50

Table 4.12: Lesion diagnosis results per each Feature Set using the Random Forest as classifier and the Median Filter (5px) as Motion Correction technique. Rows are ordered according to decreasing accuracy (highest on the top row). Median values obtained in Leave-one-Patient-Out over 26 patients (a subset of ‘DSpascale42’) are reported.

proposed so far in the literature using different feature sets extracted from our dataset. In particular, it is worth to note that Fusco et al. [72] used both Dynamic and Morphological feature with a Multiple Classifiers System (MCS), while Glaßer et al. [81] combine Clinical and Morphological feature into a Decision Tree classifier.

A comparison with the deep learning approach proposed by Antropova et al. [12] is also reported. In [12] the authors apply transfer learning to the lesion diagnosis task, by using AlexNet [126] pre-trained on natural images from ImageNet [50]. As proposed by the authors, we trained a Support Vector machine (we used a polynomial kernel with degree 3) on the output of the last internal layer of AlexNet. For a fair comparison, a leave-one-patient- out cross-validation has been performed instead of the hold-out proposed in [12]-

The results of the Convolutional Neural Network are obtained by using the neural network toolbox from MATLAB and performed using our University’s grid computing infrastructure SCoPE (scope.unina.it) where five NVIDIA Tesla K20m GPU are available.

Author	Methodology	ACC [%]	SEN [%]	SPE [%]	AUC [%]
Our proposal	LBP-TOP + RF	83.33	95.14	66.67	88.41
Fusco et al. [72]	Dyn. only + NB	59.52	65.22	52.63	58.92
	Morph. only + DT	64.29	43.48	89.47	66.48
	Dyn. & Morph. + MCS	69.05	78.26	57.89	68.08
Antropova et al. [12]	DeepCNN as ‘feature extractor’ + SVM	66.67	78.26	52.63	67.85
Glaßer et al. [81]	Morph. & Clinical + DT	64.29	95.65	26.32	60.98

Table 4.13: Comparison among performances of our proposal, for ROI diagnosis, with different approaches in literature (on the private dataset). Median values obtained in Leave-one-Patient-Out over 42 patients (‘DSpascale42’) are reported. DT: Decision Tree; MCS: Multiple Classifier System; Dyn.: Dynamic Feature; Morph.: Morphological Feature.

Receiver Operating Characteristic (ROC) analysis of the classical machine learning results in table 4.13 has been presented in the figure 4.12

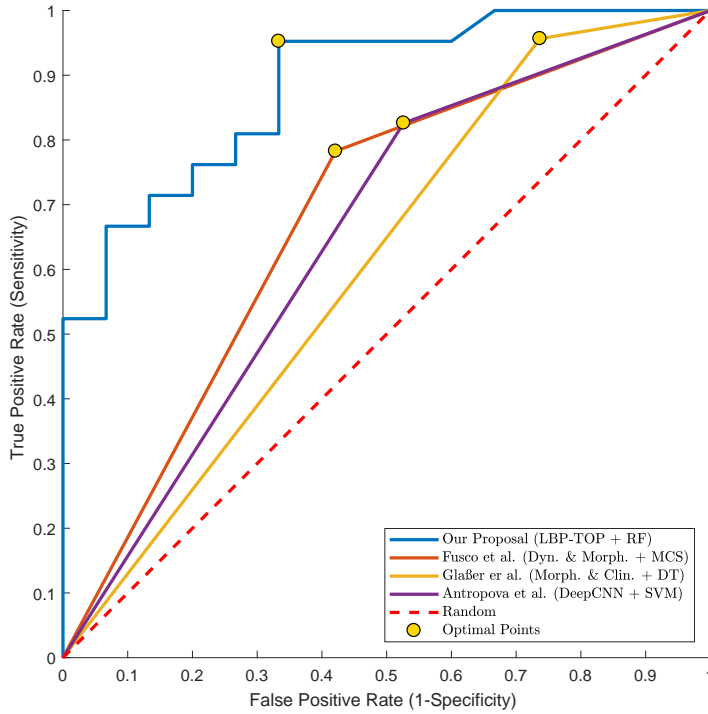


Figure 4.12: ROC analysis for the proposed approach and for the competitors for the ROI diagnosis task performed over 42 patients ('DSpascal42'). The quantitative evaluation is in table 4.13.

4.6 Therapy Assessment

The Therapy Assessment module has been evaluated on two public datasets, ‘DSpublic64’ and ‘DSpublic162’ as reported in the section 4.1. The classifiers of the ensemble have been trained on one of the available datasets and then tested on the other one; and vice-versa. Results are reported in the Table 4.14 and 4.15. Since the results of this evaluation show a low Sensitivity, the proposed approach has been evaluated in a Leave-one-patient-out modality on the union of both the datasets

	ACC [%]	SEN [%]	SPE [%]	AUC [%]
Dynamic & Pharmacokinetic	77.20	16.70	98.30	68.30
Clinical & Geometrical	76.50	26.20	94.20	63.90
Combined (wMV)	79.00	40.50	92.50	73.10

Table 4.14: Therapy assessment results. Training on ‘DSpublic64’ and Testing on ‘DSpublic162’. Median values are reported.

	ACC [%]	SEN [%]	SPE [%]	AUC [%]
Dynamic & Pharmacokinetic	68.80	20.00	100.00	69.00
Clinical & Geometrical	71.90	44.00	89.70	71.00
Combined (wMV)	71.90	60.00	79.50	73.60

Table 4.15: Therapy assessment results. Training on ‘DSpublic162’ and Testing on ‘DSpublic64’. Median values are reported.

In the Table 4.16 are shown the leave-one-patient-out result of recurrence classification for each branch and the combined result by means of weighted majority voting. The results are in terms of Accuracy, Specificity, Sensitivity and Area Under ROC Curve (AUC).

ROC analysis for each of the classifier in the MCS and the combined result is presented in the figure 4.13

	ACC [%]	SEN [%]	SPE [%]	AUC [%]
Dynamic & Pharmacokinetic	76.44	59.70	83.70	75.80
Clinical & Geometrical	75.20	28.40	95.00	73.30
Combined (wMV)	77.90	61.20	84.90	79.10

Table 4.16: Therapy assessment results on the union of ‘DSpublic64’ and ‘DSpublic162’. Median values obtained in Leave-one-Patient-Out are reported.

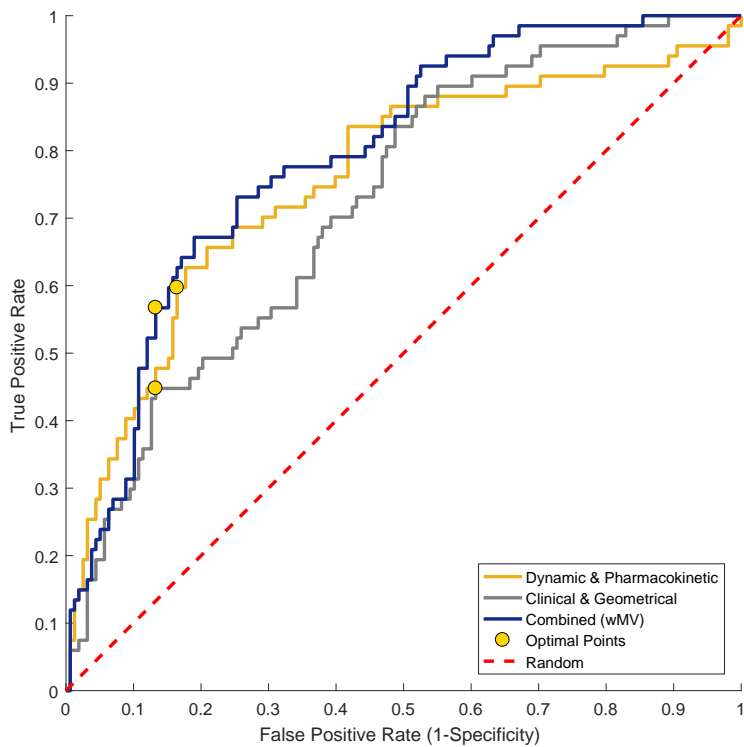


Figure 4.13: ROC analysis for the proposed approach of Therapy Assessment over 42 patients. Each branch and the combined result is reported. The quantitative evaluation is in table 4.16.

4.7 Putting it all together

The Table 4.17 reports the results of a cascade of operation in terms of Accuracy, Sensitivity, Specificity for the first stages up to the ROI Diagnosis are reported. When applicable, Dice Similarity Coefficient (DSC) and Area Under ROC Curve (AUC) is also reported. For convenience, the stand-alone execution results are reported in the table.

Module	ACC [%]	SEN [%]	SPE [%]	DSC [%]	AUC [%]
Breast Mask	97.56	95.67	98.12	91.36	-
ROI Detection	92.34 (95.71)	82.72 (82.72)	94.34 (96.06)	61.15	83.46 (85.15)
ROI Diagnosis	71.43 (83.33)	86.96 (95.14)	52.63 (66.67)	-	74.71 (88.41)

Table 4.17: Performance evaluation of the first stages up to the ROI Diagnosis. For convenience, the results of stand-alone execution are reported again (in grey). Median values obtained in Leave-one-Patient-Out over 42 patients (‘DSpascale42’) are shown.

4.8 Remote Architecture

In the following the results of the remote architecture evaluation according to the designed tests.

4.8.1 Compression tests

Four different compression protocols have been tested: Java Native Zip library, Lempel-Ziv-Markov (LZMA achieved using 7z open-source Java library), the Zip4j open source Java library and MATLAB file format compression. The transmission times of the whole dataset (for each patient) have been evaluated on a 10/100mbps Ethernet LAN. The table 4.18 reports the average results of the compression tests for Zip4j.

Compression Level	Compressed Size (MB)	Compression Ratio (%)	Compression Time (s)	Trasmission Time (s)
0 (Store)	111	0.00%	0.43	8.38
1 (Fastest)	34	68.78%	0.83	6.38
3 (Fast)	34	68.78%	1.12	6.42
5 (Normal)	32	70.33%	3.22	6.13
7 (Maximun)	31	71.28%	10.26	5.97
9 (Ultra)	31	71.48%	26.20	5.91

Table 4.18: Zip compression level impact on transmission time. The average size of an original DICOM study is about 111 MB. The compression ratio of Zip is about 70% for all levels. The level 1 (reported in bold) is the best trade-off between short transmission and compression times.

Zip4j can achieve a compression ratio of about 70% for all levels. Higher levels of compression do not seem to significantly improve the compression ratio. They dilate compression times without dramatically reducing the transmission times (that follows an exponential decrease with a lower-bound to about 6 seconds). The level 1 is the best trade-off between short transmission and compression times. It is worth noting some communication errors that alter the transmission time (on the Level 3 test) due to the best-effort feature of the TCP/IP protocol, over which, all the test have been performed.

The Figure 4.14 shows the average compression ratio computed over the overall patient dataset for each compression protocol. For each test, data is composed of both meta-information and signal intensity data. It is possible to appreciate that Zip4j algorithm (the runner-up), has a compression ratio approximately 10% lower than MATLAB results. All other files (XML) are compressed with Zip4j.

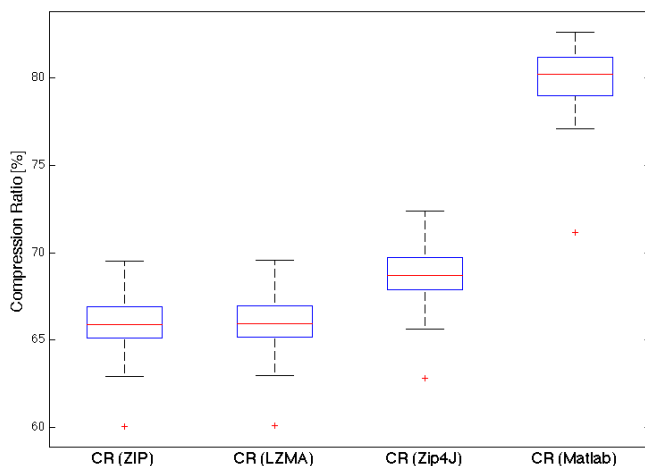


Figure 4.14: Compression ratio comparison between different compression methods, including MATLAB.

4.8.2 Transmission and Execution tests

the Figure 4.15 shows the distribution of execution and transmission times. Median values of execution (175s) and transmission (4.5s) times have been indicated as red lines.

The server side has been implemented on an Intel Core i7-3630QM 64bit Quad Core 2,4GHz equipped with 12GB RAM. Also in this case the transmission times have been evaluated on a 10/100mbps Ethernet LAN, a 100/1000mbps Ethernet LAN, a cheap xDSL (nominal 4mbps) and a MPLS (nominal 10mbps). Each average overhead was calculated according to eq. 4.3 and is shown in the Table 4.19 (for decreasing values of overhead).

In Figure 4.15, it can be observed that the transmission time has spread over a small interval (3 to 6s), while the execution time has two clear outliers of about 549s and 713s. These are due to two patients having a very high number of voxels to analyse.

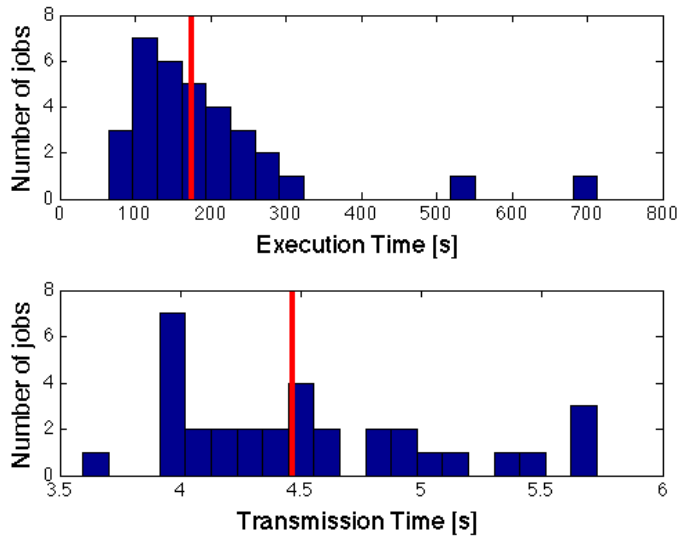


Figure 4.15: Distribution of remote execution and transmission times using 1 CPU on server node. Median values of execution (175s) and transmission (4.5s) have been indicated as red lines.

Network	Nominal	Transmission	Overhead
	Speed [<i>mbps</i>]	time [<i>s</i>]	
xDSL	4	17.104	9.15
LAN	100	4.541	2,62
MPLS (PPPoA)	10	2.832	1,66
fast LAN	1000	2.817	1,65

Table 4.19: Overhead in different network configuration (the execution time assess on about 188s). It is worth noticing that transmission time could be afflicted by network load (best-effort treatment).

4.8.3 Scalability evaluation

In the Table 4.20, are reported the average execution times of four different server side architecture configurations according to Section 4.2.3. Remote

execution times include image processing and transmission between client and server (and vice-versa). In the client-server approach, the server has been implemented on an Intel Core i7-3630QM 64bit Quad Core 2,4GHz equipped with 12GB RAM. The local evaluation has been tested on a typical OsiriX workstation (Apple iMac with Intel Core 2 Duo 2.0 GHz equipped with 3GB RAM) with lower characteristic than the client-server approach. Also in this case, transmission times have been evaluated on a 10/100mbps Ethernet LAN.

	execution time		throughput [jobs/h]	speed-up
	mean [s]	std.dev. [s]		
Local (1 job)	229.34	145.19	15.7	-
Remote (1 CPU, 1 job)	192.60	128.05	18.7	1.2
Remote (2 CPUs, 2 job)	199.40	130.41	36.1	2.3
Remote (4 CPUs, 4 job)	204.31	130.59	70.5	4.5

Table 4.20: Average execution times, throughput and speed-up in the different cases.

It is worth noticing that the execution times remain almost unchanged in all the considered configurations. However, as Table 4.20 shows, the throughput and the speed-up ratio increase are almost proportional to the number of processors used. This justifies the choice of a remote execution and brings benefits in terms of upgradability and maintainability of the segmentation algorithms and result sharing.

Discussion and Conclusions

The first objective of this thesis was to decompose the Dynamic Contrast-Enhanced Magnetic Resonance Imaging (DCE-MRI) analysis in different steps and design each phase with the aim of maximising the results with respect to the specific purpose. The second objective was to combine the single stages in a complete computer-aided detection and diagnosis (CAD) system for breast DCE-MRI. Finally, to push the collaboration of more physicians, and to have a valuable feedback for further improving the techniques, a client-server architecture for enabling the access to the CAD has been proposed. This final chapter summarises how all this was achieved, discusses the results and highlights the novel contributions.

All the performance evaluations have been obtained with respect to a manual segmentation, the histopathological reports and a ground-truth provided by an expert radiologist.

Breast Mask Extraction module

The breast mask extraction module has been designed by combining three 2D Fuzzy C-Means (FCM) clustering (executed along axial, coronal and transversal directions) and geometrical breast anatomy characterization through seven

well defined anatomical key-points. The FCM clustering is used to shift the breast mask extraction from a simple grey-level based segmentation to a membership probability one, while the geometrical characterization of breast anatomy is required to weight such probability by voxel spatial position. To improve the FCM effectiveness, the clustering was only performed on the volume delimited by the cuboid enclosing a rough breast mask. In the last stage, some morphological refinements were performed to improve the obtained breast mask. The effectiveness of each stage is shown in the Table 4.3.

Vignati et al. [252] is the only proposal able to cover 100% of the lesions but shows a notable over-segmentation and low accuracy. In general, all the pixel-based approaches shown poor accuracy to contain the side effect of the over-segmentation such as Goshal et al. [84]. Fooladivanda et al. [68] proposed an atlas-based approach to segment the pectoral muscle and refined a pixel-based breast-air segmentation. The proposal shows a very low lesion coverage and requires high computational effort in terms of time and hardware resources. Pectoral muscle is also segmented by geometrical-based approaches such as Lu et al. [151] and by Wu et al. [267]. The first one fails in cover the lesions because of the too specific parametrization of the deformable models. The second one is the best proposal in the analysed literature in terms of accuracy and lesion coverage but still fails in lesions lying on the pectoral muscle, since they confuse the edge detector.

The results in the Tables 4.4 and 4.5 show that the combined effect of a grey level segmentation, geometrical/anatomical characterization and three fuzziness evaluation lead us to overcome the former problems. Moreover, the key-point characterization of breast anatomy can be effectively used to weight FCM membership probability, allowing to accurately separate pectoral muscle from chest-wall.

Motion Correction module

In the Motion Correction module, a kinetic model-based Quality Index (QI) for evaluation of Motion Correction techniques (MCTs) in DCE-MRI has been proposed. The aim of this module was to choose and apply the best MCT for the subject under examination. The patient-based choice of MCT is required because, as shown in the Table 4.6, there is no single motion correction that outperforms the others among all the patient dataset. A novel QI is, then, required because traditional image registration similarity measures assume that voxel intensity changes only because of tissues spatial transformations, being unsuitable for images obtained under contrast medium flow as in DCE-MRI.

In general, as evident in the Table 4.7, the novel model-based QIs always outperform the traditional QIs. In particular, the results showed that the selected QI, obtained using the Extended Tofts-Kermode (ETK) model (*ETK-P*), is, at 74%, in accordance with the ‘reference ranking’ (in Table 4.6). The mixed QIs are not able to improve these results.

Furthermore, the amount of computational work can be abated from about ten hours till to about thirty minutes (tested on an Intel i7-3630QM 64bit Quad Core 2.4GHz equipped with 12GB RAM and MATLAB R2013b) without affecting the global performance (in terms of median and standard deviation values) by only using 15% of the data (Figure 4.4).

To the best of our knowledge, it is the first time that motion correction is evaluated by means of pharmacokinetic models. All the results show that using the novel tracer-kinetic-aware quality index and a small percentage of the whole volume is possible to adequately assess the effectiveness of a DCE-MRI motion correction. Moreover, as shown in the Figure 4.5, by using about 40% of the data (to always hit the best MCT), the proposed quality index could be efficiently used, before of any DCE-MRI data analysis, to choose the better performing motion correction technique for the specific patient.

Lesion Detection module

The Lesion Detection module aims to identify the lesion inside the whole breast tissues. The proposed method is based on a Support Vector Machine classifier trained on dynamic features extracted, after a suitable pre-processing of the image, from a pre-selected area by using a pixel-based approach. To prove the validity of the pre-selection stage, the final result has been considered with and without this step. Therefore, to better validate the module, different classifier and different MCTs have been considered.

The results in the Table 4.8 show that the approach with an SVM classification can give simultaneously a high accuracy and specificity, and a good value of sensitivity. It is also worth noticing that results in terms of sensitivity are even better in practice since they refer to voxels and not to ROIs. Since the purpose of the proposed method is to support the radiologist in his work, the best method is in fact the one that maximises accuracy (in order to increase the probability to correctly recognize suspect regions) and specificity (in order to reduce false alarms), looking at the same time to an acceptable sensitivity (to be almost sure to recognize a satisfying ROI area).

Moreover, from Table 4.8 can also be observed that, on average, the results obtained by using the median registration outperform those obtainable with any other MCT. The obtained results also confirmed that the use of a RE based voxel pre-selection gave always rise to better results with respect to the case when no pre-selection is used. When pre-selection was used, the SVM classifier performed consistently better than MLP and RF (differences in accuracy are always statistically significant ($p < 0.05$)).

Then, as it is evident in the Table 4.10, the proposal demonstrated the best accuracy, with a sensitivity which is significantly higher than the second best. As regards the other two approaches, the difference among their accuracies and the one obtained by our approach is statistically significant ($p < 0.05$).

The key point and the novelty of that stage consist of a suitable pre-processing stage able to performing a pre-selection of the most suspected voxels and strongly improving the final results.

Lesion Diagnosis module

For the Lesion Diagnosis module, the textural descriptor Local Binary Patterns on Three Orthogonal Planes (LBP-TOP) has been used for the assessment of lesion malignancy in breast DCE-MRI. Different classifiers (RF, MLP, and SVM), as well as the contribution of a motion correction technique, were evaluated. LBP-TOP were extracted from manually segmented ROIs for all patients in our database. Classification performance of LBP-TOP was assessed in a leave-one-out cross-validation.

From Table 4.11 emerges that, when RF is used in combination with LBP-TOP features, motion correction improves the classification results. On the other hand, for SVM and MLP it is better not to use motion correction. These last results seem in contrast with our previous findings in Lesion Detection module: differently from dynamic features, LBP-TOP textural features are not always influenced by patient movements. However, it is worth to note that, in the Lesion Detection module, the classification with dynamic features was aimed at voxel-by-voxel ROI segmentation instead of whole ROI classification. A sort of noise attenuation is to be considered intrinsically.

Results in table 4.12 indicate that LBP-TOP combined with random forest classifier and median filtering with a 5px sliding windows as motion correction technique achieves the highest accuracy (84.6%) when only the YT histogram is used.

To the best of our knowledge, this is the first time that LBP-TOP descriptors are used for breast tissue classification in DCE-MRI.

Moreover, it is worth noting that (see Tab.4.13) the proposed approach significantly outperforms the other method under comparison [72, 81] in terms of overall accuracy, giving rise to a very good specificity.

Antropova et al. [12] investigate deep learning in the lesion detection task using DCE-MRI data. The authors propose to apply transfer learning from a pre-trained Deep Convolutional-Neural-Network (DeepCNN). Results presented in table 4.13 show that transfer learning from natural images (ImageNet) of deep approaches seems to be not enough for classifying DCE-MRI images malignity. We obtained a slight improvement by using AlexNet with fine-tuning. A fine-tuning of a pre-trained deep CNN consists in replacing the last trained fully connected layers with the same untrained fully connected layer and re-train it on the target classification task. We got 69.05%, 65.22%, 73.68% and 68.99%, respectively, in terms of Accuracy, Sensitivity, Specificity and Area Under the ROC Curve. This result outperforms the one obtained with the approach proposed in [12] but it is still lower than our proposal.

One issue concerning the use of LBP in the context of DCE-MRI lies in the fact that there is no clear physiological interpretation (on the contrary of the dynamic feature having a direct physiological interpretation): therefore they can be difficult to understand from a radiologist point of view.

Therapy Assessment module

The Therapy Assessment module adds a novel stage to the computer-aided detection and diagnosis systems. The forecasting of therapy success was always demanded to physicians according to the clinical information and the few features easily handled from radiologists such as morphological evidence (such as volume or evident asymmetry) and pathological status (response to therapy and nodal status) of the subject.

This module automatically provides the recurrence probability relying on dynamic, pharmacokinetic, morphological and clinicopathologic features.

An ensemble of classifiers combines the most reliable information from each feature set to provide to the physician the tumour recurrence probability.

In the table 4.16 are shown the results of each branch of the ensemble, and the final combined result by means of weighted majority voting. An accuracy of 77.9% has been achieved.

Adding this stage to the so far proposed CAD aims to prevent potentially ineffective and toxic treatments before surgery and apply patient-based therapy in the most efficient way.

Putting it all Together

In order to validate the effectiveness of the complete CAD proposal, a cascade execution of the first steps of the CAD, up to the lesion diagnosis, has been performed. Even if the results in table 4.17 show lower performance with respect to the stand-alone execution of the respective blocks, the final result of ROI detection still outperforms the runner-up proposal. The final stage of Therapy Assessment can't be tested in a cascade execution mode due to the lack of heterogeneity in the datasets and in the ground truths.

Remote Architecture

The final result of this thesis is an architecture for advanced remote data processing in a secure and versatile client-server environment. This architecture aims to push the collaboration of more physicians to have a valuable feedback for further improving the techniques and to apply the research progress in a realistic environment

The result is a process-on-demand architecture, allowing the radiologist to have access to a secure, versatile and powerful remote CAD system.

The aim of the proposed architecture was the possibility of easily integrating a pre-existing medical image processing software within a complete CAD system deployed on a server machine and shared with many workstations.

This has the benefit to allow the physician to not change the user interface he is accustomed to, but to extend the pre-existent software via a plug-in. This is one of the main novelties with respect to previous works that proposed interaction with the user through proprietary interfaces [155].

The plug-in's main role is to interact with the physician making all required tasks (XML file creation, DICOM exporting, status monitoring and alerting, result reporting) totally transparent to the operator. The jM-FlowOrchestrator (client) role is to extract sensitive data from DICOM files, prepare the MATLAB formatted files to the lower transmission layer (jSecureSync) and manage status updates working jointly with its counterpart on the server side.

To make the proposed system available for a new client-side image processing application, only the small plug-in development is needed, as the JM-FlowOrchestrator is written in Java (making it portable and transferable to different operative systems with ease).

The proposed strategy allows meeting the integration goal easy, as long as the third-party client implements a customization such as a plug-in or API philosophy supported by some form of SDK toolboxes. As a result, the use of a plug-in together with jSecureSync and jM-FlowOrchestrator makes the proposed architecture versatile and have 'low-impact' on the pre-existent infrastructure.

The use of a remote server for advanced operation execution allows an increase in number and type of services offered. It also improves withstanding services without any modification on the client side. Moreover, during server execution, the client user can utilise his workstation for other kinds of work, optimising task time. The Table 4.20 shows that the use of a multiprocessor server (or a cluster of multi-processor servers) yields a system that has an execution time comparable with the local processing system, but with a higher throughput value, which is quite proportional to the number of used processors. The multi-client/single-server structure optimises the use of

resources by allocating different atomic jobs on different CPUs. The Table 4.20 also shows that, by increasing the number of the available CPUs and jobs, the mean execution time only slightly increases a little. This allows an easy handling of small and big increase of requests by adding additional CPUs or multiprocessors servers to the cluster.

It is worth noticing that the proposed architecture, with reference to a typical radiological workstation, does not require further expensive hardware, interconnection networking or operating system (all tests were performed on commercial notebook/pc/Mac and on conventional network infrastructures), making it suitable for small clinical structures with few radiologists, up to big hospitals or structures in which tens of radiologists are involved.

In order to limit transmission time, image files need to be compressed before being sent over the network. For the specific implementation of the architecture reported in this thesis, compression tests showed that, due to the significant correlation of medical image data and the extraction of repeated meta-data information, the use of the MATLAB format can produce results even better than those obtained by using the fastest compression offered by Zip4j (level 1). The compression ratio was about 70% for Zip4j, while MATLAB format can achieve a compression ratio up to 80% (Table 4.18). All other files not in DICOM format (XML) are compressed with the Zip4j protocol. Transmission and execution time measurements were then performed on some plausible scenario, for a practical clinical environment, corresponding both to a private network among different structures from the same company and to different companies connected through available network infrastructures (e.g. optical fiber). The overhead added by network infrastructure (Table 4.19), settles on about 2.5% (for the widespread 10/100 Mbps) of the remote processing execution time. This overhead reaches a still acceptable value of 10% in the worst case of a cheaper xDSL network WAN connection. This could make it possible to apply the proposed architecture

even over a more diffused network (such as xDSL) without a significant decrease in performance.

The remote processing of medical images, such as the approaches in this thesis, rises complex and severe security issues. When analysed, security issues are typically resolved by considering server and client connected by a private dedicated network [44]. The proposed architecture can be safely used over every kind of interconnection network that supports TCP/IP stack protocol, allowing the development of multi-center interconnections distributed over a wide geographical area. All the security evaluation is thorough using SSL, AES and RSA parameters meeting the 2012 NIST standard requirements [15] and will ensure channel privacy through to the year 2030 at minimum. This will allow for a distribution of the system cost over a longer period. On the other hand, the use of authorization certificates means a simple and safe authentication and authorisation phase.

Although the DICOM standard provides all functionality needed in the architecture, it has intentionally not used with the aim of decoupling the proposal from any particular application context. The proposed architecture has been demonstrated with reference to biomedical image processing, but it is possible to apply it even in different contexts (i.e. not using DICOM).

In conclusion, the proposed architecture has a secure, versatile and low-impact approach, making this work suitable to enable an easy integration into intelligent environments.

Open Issues

Even if, during the design of a CAD for breast cancer in Dynamic Contrast-Enhanced Magnetic Resonance Imaging (DCE-MRI), all the stages have been optimised as good as possible, few open issues still need to be investigated.

As a matter of fact, the number of patients should be increased by merging more dataset or by improving the partnership with the medical infrastructures. Moreover, a bigger number of patients could push the integration of different protocols such as T1 non fat-sup, T1 fat-sup and T2 in all the stage of the Computer-Aided Detection and Diagnosis (CAD).

The issues addressed in this thesis have been designed in the pattern recognition framework. In particular: Breast Mask Extraction and Lesion Detection consist of a 3D grey-level volume segmentation; Lesion Diagnosis is faced as an object classification task; Therapy Assessment can be configured either as a regression problem or a classification problem. The most recent literature proposals mostly differ in the feature vector used to describe the classification subject.

Then, even if newer features are constantly proposed by domain experts, it seems that small improvements were so far achieved. Some proposals try to overcome this limit by adding pre-processing or post-processing stages in each module with the purpose of preparing data or refining the final results.

Deep Learning, instead, provides a different approach to the resolution of such issues by using a set of successive layers that automatically learn the best way to describe data as composed of simpler concepts. The key idea is to involve the feature extraction process in the training stage. It follows that features are tailored to the specific problem and usually this approach performs better with respect to those using human designed features.

Deep Learning has demonstrated the ability to outperform the classical machine learning approaches in different fields, even getting able to outperform skilled humans in some computer vision tasks. In the last years, some 'Deep Approaches' have been proposed to assess different issues such as:

- Deep Belief Network (DBN) [17, 105]: used to solve general classification tasks;
- Deep Convolution Neural Network (Deep CNN) [135, 136, 125]: neural networks used for images labelling, face recognition and text analysis. If suitably adjusted, they could be used for segmentation tasks [150];
- Recurrent Neural Network (RNN) [86, 223]: employed in sequence learning and time series analysis.

Different frameworks are currently available to apply deep approaches. Each framework follows a different philosophy and needs to be analysed according to the problem to be solved. Among the most popular tools, it also worth to mention: Caffe, TensorFlow, Deeplearning4j, Microsoft Cognitive Toolkit, Theano and Torch.

To the best of our knowledge, in biomedical imaging field, deep approaches were mainly used in brain DCE-MRI, both for lesion and anatomical segmentation [58, 99, 184, 194, 261, 277]. Deep Learning was also applied for prostate tissues, by using deep auto-encoders for tumours grading and diagnosis [147, 208]. As far as we know, breast cancer DCE-MRI image segmentation was never faced with deep approaches.

We only find one work that uses MR images to predict malignity via pre-trained CNN on yet-segmented images [12]. Some works have also addressed the nuclei detection in histopathological images [255, 269].

However, our implementation of the approach proposed in [12] did not provide good results. So, it is necessary to study how to suitably adapt deep architectures to our CAD. Deep learning could be successfully applied in the segmentation stages to perform Breast Mask Extraction and Lesion Detection.

To further improve the results of each stage and, consequently, the final result, the DCE-MRI could be supported by introducing new imaging findings. DCE-MRI is frequently merged and jointly studied with mammography but other studies could be considered: Diffusion Weighted Imaging (DWI), Positron Emission Tomography (PET) or Computed Tomography (CT). Fusing that studies requires a very reliable co-registration technique and a strong knowledge of the most descriptive features derived from each study to achieve the best result from the fusion.

Since the breast mask stage is anatomical-based, some particular case should be specifically assessed. A well-designed algorithm should take into account Lumpectomy, Quadrantectomy and Mastectomy breast to operate in any case.

As regards as the quality index, in literature there are different physiological models still to be used as an underlying model of the proposed quality index. Then, there is still a margin of improvement. Moreover, the quality index of the motion correction technique could be used as a similarity measure to evaluate the step-by-step approach of motion correction in order to produce a new motion correction technique able to take into account the contrast agent evolution in the tissue and providing the best result for motion reduction in DCE-MRI.

Finally, with the aim of improving the feasibility of all the proposals, the computational impact should be taken into account. The most of the proposed algorithms could be parallelised to achieve a strong speed-up. GPU

computing should also be considered for speed-up purposes in computer vision tasks.

Bibliography

- [1] Abdolmaleki, P., Buadu, L. D., Murayama, S., Murakami, J., Hashiguchi, N., Yabuuchi, H., and Masuda, K. (1997). Neural network analysis of breast cancer from MRI findings. *Radiation medicine*, 15(5):283–93.
- [2] Abdolmaleki, P., Buadu, L. D., and Naderimansh, H. (2001). Feature extraction and classification of breast cancer on dynamic magnetic resonance imaging using artificial neural network. *Cancer letters*, 171(2):183–191.
- [3] Abraham, D. C., Jones, R. C., Jones, S. E., Cheek, J. H., Peters, G. N., Knox, S. M., Grant, M. D., Hampe, D. W., Savino, D. A., and Harms, S. E. (1996). Evaluation of neoadjuvant chemotherapeutic response of locally advanced breast cancer by magnetic resonance imaging. *Cancer*, 78(1):91–100.
- [4] Abramowitz, M. and Stegun, I. A. (1965). *Handbook of Mathematical Functions with Formulas, Graphs, and Mathematical Tables*. Dover New York.
- [5] Agner, S. C., Soman, S., Libfeld, E., McDonald, M., Thomas, K., Englander, S., Rosen, M. A., Chin, D., Nosher, J., and Madabhushi, A. (2011). Textural kinetics: A novel dynamic contrast-enhanced (DCE)-MRI feature for breast lesion classification. *Journal of Digital Imaging*, 24(3):446–463.
- [6] Agner, S. C., Xu, J., Fatakdawala, H., Ganesan, S., Madabhushi, A., Englander, S., Rosen, M., Thomas, K., Schnall, M., Feldman, M., and

- Tomaszewski, J. (2009). Segmentation and classification of triple negative breast cancers using DCE-MRI. In *2009 IEEE International Symposium on Biomedical Imaging: From Nano to Macro*, pages 1227–1230. IEEE.
- [7] Ahonen, T., Hadid, A., and Pietikäinen, M. (2006). Face description with local binary patterns: application to face recognition. *IEEE transactions on pattern analysis and machine intelligence*, 28(12):2037–41.
- [8] Alshanbari, H., Amain, S., Shuttelworth, J., Slman, K., and Muslam, S. (2015). Automatic Segmentation In Breast Cancer Using Watershed Algorithm. *International Journal of Biomedical Engineering and Science (IJBES)*, 2(2):1–6.
- [9] Amadasun, M. and King, R. (1989). Textural features corresponding to textural properties. *IEEE Transactions on Systems, Man, and Cybernetics*, 19(5):1264–1274.
- [10] American Cancer Society (2012). The History of Cancer.
- [11] Anand, P., Kunnumakkara, A. B., Kunnumakara, A. B., Sundaram, C., Harikumar, K. B., Tharakan, S. T., Lai, O. S., Sung, B., and Aggarwal, B. B. (2008). Cancer is a preventable disease that requires major lifestyle changes. *Pharmaceutical research*, 25(9):2097–116.
- [12] Antropova, N., Huynh, B., and Giger, M. (2016). SU-D-207B-06: Predicting Breast Cancer Malignancy On DCE-MRI Data Using Pre-Trained Convolutional Neural Networks. *Medical physics*, 43(6):3349–3350.
- [13] Arbach, L., Stolpen, A., and Reinhardt, J. (2004). Classification of breast MRI lesions using a backpropagation neural network (BNN). In *2004 2nd IEEE International Symposium on Biomedical Imaging: Macro to Nano (IEEE Cat No. 04EX821)*, volume 2, pages 253–256. IEEE.
- [14] Baluwala, H. Y. (2015). Breast MRI segmentation using supervoxel classification. In *Medical image computing and computer-assisted intervention : MICCAI ... International Conference on Medical Image Computing and Computer-Assisted Intervention*, number October.
- [15] Barker, E., Barker, W., Burr, W., Polk, W., and Smid, M. (2006). Recommendation for key management-part 1: General (revision 3). *NIST Special Publication*, pages 800–57.

-
- [16] Barker, E., Johnson, D., and Smid, M. (2007). Recommendation for pairwise key establishment schemes using discrete logarithm cryptography. *NIST Special Publication*, pages 800–56A.
- [17] Bengio, Y. (2009). Learning Deep Architectures for AI. *Foundations and Trends® in Machine Learning*, 2(1):1–127.
- [18] Berrington de González, A. and Darby, S. (2004). Risk of cancer from diagnostic X-rays: estimates for the UK and 14 other countries. *Lancet (London, England)*, 363(9406):345–51.
- [19] Bhooshan, N., Giger, M. L., Jansen, S. A., and Newstead, G. M. (2010). Cancerous Breast Lesions on Dynamic Contrast-enhanced MR Images. *Breast Imaging*, 254(3).
- [20] Bidgood, W. D., Horii, S. C., Prior, F. W., and Van Syckle, D. E. (1997). Understanding and using DICOM, the data interchange standard for biomedical imaging. *Journal of the American Medical Informatics Association : JAMIA*, 4(3):199–212.
- [21] Blake-Wilson, S., Bolyard, N., Gupta, V., Hawk, C., and Moeller, B. (2006). Elliptic Curve Cryptography (ECC) Cipher Suites for Transport Layer Security (TLS). RFC 4492 (Informational). Updated by RFCs 5246, 7027.
- [22] Bonadonna, G., Valagussa, P., Brambilla, C., Ferrari, L., Moliterni, A., Terenziani, M., and Zambetti, M. (1998). Primary chemotherapy in operable breast cancer: eight-year experience at the Milan Cancer Institute. *Journal of clinical oncology : official journal of the American Society of Clinical Oncology*, 16(1):93–100.
- [23] Bondy, M. (2011). Cancer Mortality and Morbidity Patterns in the U.S. Population: An Interdisciplinary Approach. *JAMA*, 306(6).
- [24] Breiman, L. (2001). Random forests. *Machine learning*, 45(1):5–32.
- [25] Brem, R. F., Baum, J., Lechner, M., Kaplan, S., Souders, S., Naul, L. G., and Hoffmeister, J. (2003). Improvement in sensitivity of screening mammography with computer-aided detection: a multiinstitutional trial. *AJR. American journal of roentgenology*, 181(3):687–93.
- [26] Brix, G., Kiessling, F., Lucht, R., Darai, S., Wasser, K., Delorme, S., and Griebel, J. (2004). Microcirculation and microvasculature in breast

tumors: Pharmacokinetic analysis of dynamic MR image series. *Magnetic Resonance in Medicine*, 52(2):420–429.

- [27] Brown, J., Buckley, D., Coulthard, A., Dixon, A. K., Dixon, J. M., Easton, D. F., Eeles, R. A., Evans, D. G., Gilbert, F. G., Graves, M., Hayes, C., Jenkins, J. P., Jones, A. P., Keevil, S. F., Leach, M. O., Liney, G. P., Moss, S. M., Padhani, A. R., Parker, G. J., Pointon, L. J., Ponder, B. A., Redpath, T. W., Sloane, J. P., Turnbull, L. W., Walker, L. G., and Warren, R. M. (2000). Magnetic resonance imaging screening in women at genetic risk of breast cancer: imaging and analysis protocol for the UK multicentre study. UK MRI Breast Screening Study Advisory Group. *Magnetic resonance imaging*, 18(7):765–76.
- [28] Brown, L. G. (1992). A survey of image registration techniques. *ACM Computing Surveys*, 24(4):325–376.
- [29] Buchholz, T. A., Hill, B. S., Tucker, S. L., Frye, D. K., Kuerer, H. M., Buzdar, A. U., McNeese, M. D., Singletary, S. E., Ueno, N. T., Pusztai, L., Valero, V., and Hortobagyi, G. N. (2001). Factors predictive of outcome in patients with breast cancer refractory to neoadjuvant chemotherapy. *Cancer journal (Sudbury, Mass.)*, 7(5):413–420.
- [30] Cai, H., Peng, Y., Ou, C., Chen, M., and Li, L. (2014). Diagnosis of breast masses from dynamic contrast-enhanced and diffusion-weighted MR: a machine learning approach. *PloS one*, 9(1):e87387.
- [31] Castellano, G., Bonilha, L., Li, L., and Cendes, F. (2004). Texture analysis of medical images. *Clinical Radiology*, 59(12):1061–1069.
- [32] Certicom Research (2000). Standards for efficient cryptography sec 1: Elliptic curve cryptography. Retrieved February, 2014, from http://www.secg.org/collateral/sec1_final.pdf.
- [33] Chang, C.-C. and Lin, C.-J. (2011). LIBSVM. *ACM Transactions on Intelligent Systems and Technology*, 2(3):1–27.
- [34] Chen, W., Giger, M. L., Bick, U., and Newstead, G. M. (2006). Automatic identification and classification of characteristic kinetic curves of breast lesions on DCE-MRI. *Medical Physics*, 33(8):2878–2887.
- [35] Cheng, H., Shi, X., Min, R., Hu, L., Cai, X., and Du, H. (2006). Approaches for automated detection and classification of masses in mammograms. *Pattern Recognition*, 39(4):646–668.

-
- [36] Cherry, S. R. and Dahlbom, M. (2006). PET: Physics, Instrumentation, and Scanners. In *PET*, pages 1–117, New York, NY. Springer, Springer New York.
- [37] Choi, E. J., Choi, H., Choi, S. A., and Youk, J. H. (2016). Dynamic contrast-enhanced breast magnetic resonance imaging for the prediction of early and late recurrences in breast cancer. *Medicine*, 95(48):e5330.
- [38] Chowdhury, S. and Boskamp, E. B. (1994). Breast coil for magnetic resonance imaging (US Patent 5,363,845).
- [39] Chown, P. (2002). Advanced Encryption Standard (AES) Ciphersuites for Transport Layer Security (TLS). RFC 3268 (Proposed Standard). Obsoleted by RFC 5246.
- [40] Chu, A., Sehgal, C., and Greenleaf, J. (1990). Use of gray value distribution of run lengths for texture analysis. *Pattern Recognition Letters*, 11(6):415–419.
- [41] Clark, K., Vendt, B., Smith, K., Freymann, J., Kirby, J., Koppel, P., Moore, S., Phillips, S., Maffitt, D., Pringle, M., and Others (2013). The Cancer Imaging Archive (TCIA): maintaining and operating a public information repository. *Journal of digital imaging*, 26(6):1045–1057.
- [42] Collignon, A., Maes, F., Delaere, D., Vandermeulen, D., Suetens, P., and Marchal, G. (1995). Automated multi-modality image registration based on information theory. *14th International Conference on Information Processing in Medical Imaging*, pages 263–274.
- [43] Cortes, C. and Vapnik, V. (1995). Support-vector networks. *Machine Learning*, 20(3):273–297.
- [44] Crane, J. C., Crawford, F. W., and Nelson, S. J. (2006). Grid enabled magnetic resonance scanners for near real-time medical image processing. *Journal of Parallel and Distributed Computing*, 66(12):1524–1533.
- [45] Damadian, R. (1971). Tumor detection by nuclear magnetic resonance. *Science (New York, N.Y.)*, 171(3976):1151–3.
- [46] Dasarathy, B. V. and Holder, E. B. (1991). Image characterizations based on joint gray level—run length distributions. *Pattern Recognition Letters*, 12(8):497–502.

- [47] De Kerviler, E., Leroy-Willig, A., Clément, O., and Frija, J. (1998). Fat suppression techniques in MRI: an update. *Biomedicine & pharmacotherapy = Biomedecine & pharmacotherapie*, 52(2):69–75.
- [48] Degani, H., Gusis, V., Weinstein, D., Fields, S., and Strano, S. (1997). Mapping pathophysiological features of breast tumors by MRI at high spatial resolution. *Nature medicine*, 3(7):780–782.
- [49] Delfaut, E. M., Beltran, J., Johnson, G., Rousseau, J., Marchandise, X., and Cotten, A. (1999). Fat suppression in MR imaging: techniques and pitfalls. *Radiographics : a review publication of the Radiological Society of North America, Inc*, 19(2):373–82.
- [50] Deng, J., Dong, W., Socher, R., Li, L.-J., Li, K., and Fei-Fei, L. (2009). Imagenet: A large-scale hierarchical image database. In *Computer Vision and Pattern Recognition, 2009. CVPR 2009. IEEE Conference on*, pages 248–255. IEEE.
- [51] Dice, L. R. (1945). Measures of the Amount of Ecologic Association Between Species. *Ecology*, 26(3):297–302.
- [52] Dierks, T. and Allen, C. (1999). The TLS Protocol Version 1.0. RFC 2246 (Proposed Standard). Obsoleted by RFC 4346, updated by RFCs 3546, 5746, 6176.
- [53] Dierks, T. and Rescorla, E. (2006). The Transport Layer Security (TLS) Protocol Version 1.1. RFC 4346 (Proposed Standard). Obsoleted by RFC 5246, updated by RFCs 4366, 4680, 4681, 5746, 6176.
- [54] Dierks, T. and Rescorla, E. (2008). The Transport Layer Security (TLS) Protocol Version 1.2. RFC 5246 (Proposed Standard). Updated by RFCs 5746, 5878, 6176.
- [55] Dmitriev, I. D., Loo, C. E., Vogel, W. V., Pengel, K. E., and A Gilhuijs, K. G. (2013). Fully automated deformable registration of breast DCE-MRI and PET/CT. *Phys. Med. Biol*, 58(4):1221–1233.
- [56] Drew, P. J., Kerin, M. J., Mahapatra, T., Malone, C., Monson, J. R. T., Turnbull, L. W., and Fox, J. N. (2001). Evaluation of response to neoadjuvant chemoradiotherapy for locally advanced breast cancer with dynamic contrast-enhanced MRI of the breast. *European Journal of Surgical Oncology*, 27(7):617–620.

-
- [57] Duda, R. O., Hart, P. E., and Stork, D. G. (2012). *Pattern classification*. John Wiley & Sons.
 - [58] Dvořák, P. and Menze, B. (2016). Local Structure Prediction with Convolutional Neural Networks for Multimodal Brain Tumor Segmentation. pages 59–71.
 - [59] Eder, M., Raith, S., Jalali, J., Volf, A., Settles, M., Machens, H. G., and Kovacs, L. (2014). Comparison of different material models to simulate 3-D breast deformations using finite element analysis. *Annals of Biomedical Engineering*, 42(4):843–857.
 - [60] Eiben, B., Han, L., Hipwell, J., Mertzaniidou, T., Kabus, S., Buelow, T., Lorenz, C., Newstead, G. M., Abe, H., Keshtgar, M., Ourselin, S., and Hawkes, D. J. (2013). Biomechanically guided prone-to-supine image registration of breast MRI using an estimated reference state. *Proceedings - International Symposium on Biomedical Imaging*, pages 214–217.
 - [61] Eiben, B., Vavourakis, V., Hipwell, J. H., Kabus, S., Lorenz, C., Buelow, T., and Hawkes, D. J. (2014). Breast deformation modelling: comparison of methods to obtain a patient specific unloaded configuration. page 903615.
 - [62] Ekblom, A., Adami, H. O., Trichopoulos, D., Lambe, M., Hsieh, C. C., and Pontén, J. (1994). Epidemiologic correlates of breast cancer laterality (Sweden). *Cancer causes & control : CCC*, 5(6):510–6.
 - [63] El-nasr, S. I. S., Rahman, R. W. A., Abdelrahman, S. F., Helal, M. H., and Hamed, S. T. (2016). Role of diffusion weighted imaging and dynamic contrast enhanced MR mammography to detect recurrence in breast cancer patients after surgery. *The Egyptian Journal of Radiology and Nuclear Medicine* El-nasr, S. I. S., Rahman, R. W. A., Abdelrahman, S. F., Helal, M. H., & Hamed, S. T. (2016). Role of diffusion weighted imaging and dynamic contrast enhanced MR mammography to detect recurrence in bre, 47(3):4–10.
 - [64] Ertaş, G., Gülçür, H. Ö., Osman, O., Uçan, O. N., Tunaci, M., and Dursun, M. (2008). Breast MR segmentation and lesion detection with cellular neural networks and 3D template matching. *Computers in Biology and Medicine*, 38(1):116–126.
 - [65] Eyal, E., Badikhi, D., Furman-Haran, E., Kelcz, F., Kirshenbaum, K. J., and Degani, H. (2009). Principal component analysis of breast DCE-MRI

- adjusted with a model-based method. *Journal of magnetic resonance imaging : JMRI*, 30(5):989–98.
- [66] Fenton, J. J., Taplin, S. H., Carney, P. A., Abraham, L., Sickles, E. A., D’Orsi, C., Berns, E. A., Cutter, G., Hendrick, R. E., Barlow, W. E., and Elmore, J. G. (2007). Influence of computer-aided detection on performance of screening mammography. *The New England journal of medicine*, 356(14):1399–409.
- [67] Fisher, B., Bryant, J., Wolmark, N., Mamounas, E., Brown, A., Fisher, E. R., Wickerham, D. L., Begovic, M., DeCillis, A., Robidoux, A., Margolese, R. G., Cruz, A. B., Hoehn, J. L., Lees, A. W., Dimitrov, N. V., and Bear, H. D. (1998). Effect of preoperative chemotherapy on the outcome of women with operable breast cancer. *Journal of clinical oncology : official journal of the American Society of Clinical Oncology*, 16(8):2672–85.
- [68] Fooladivanda, A., Shokouhi, S. B., Mosavi, M. R., and Ahmadinejad, N. (2014). Atlas-based automatic breast MRI segmentation using pectoral muscle and chest region model. In *2014 21th Iranian Conference on Biomedical Engineering (ICBME)*, pages 258–262. IEEE.
- [69] Force, U. P. S. T. (2009). Uspstf recommendation: Screening for breast cancer. <http://www.uspreventiveservicestaskforce.org/uspstf/uspbrca.htm>.
- [70] Freund, Y. and Schapire, R. E. (1997). A Decision-Theoretic Generalization of On-Line Learning and an Application to Boosting. In *Journal of Computer and System Sciences*, volume 55, pages 119–139. Springer.
- [71] Fusco, R., Sansone, M., Maffei, S., Raiano, N., and Petrillo, A. (2012a). Dynamic contrast-enhanced MRI in breast cancer: A comparison between distributed and compartmental tracer kinetic models. *Journal of Biomedical Graphics and Computing*, 2(2).
- [72] Fusco, R., Sansone, M., Petrillo, A., and Sansone, C. (2012b). A multiple classifier system for classification of breast lesions using dynamic and morphological features in DCE-MRI. In *Joint IAPR International Workshops on Statistical Techniques in Pattern Recognition (SPR) and Structural and Syntactic Pattern Recognition (SSPR)*, pages 684–692. Springer, Springer.
- [73] Fusco, R., Sansone, M., Petrillo, M., and Petrillo, A. (2014). Influence of Parameterization on Tracer Kinetic Modeling in DCE-MRI. *Journal of Medical and Biological Engineering*, 34(2):157.

-
- [74] Fusco, R., Sansone, M., Sansone, C., and Petrillo, A. (2012c). Segmentation and classification of breast lesions using dynamic and textural features in Dynamic Contrast Enhanced-Magnetic Resonance Imaging. In *2012 25th IEEE International Symposium on Computer-Based Medical Systems (CBMS)*, pages 1–4. IEEE, IEEE.
- [75] Gal, Y., Mehnert, A., Bradley, A., Kennedy, D., and Crozier, S. (2009). Feature and Classifier Selection for Automatic Classification of Lesions in Dynamic Contrast-Enhanced MRI of the Breast. In *2009 Digital Image Computing: Techniques and Applications*, pages 132–139. IEEE.
- [76] Galloway, M. M. (1975). Texture analysis using gray level run lengths. *Computer Graphics and Image Processing*, 4(2):172–179.
- [77] Garimella, V., Qutob, O., Fox, J. N., Long, E. D., Chaturvedi, A., Turnbull, L. W., and Drew, P. J. (2007). Recurrence rates after DCE-MRI image guided planning for breast-conserving surgery following neoadjuvant chemotherapy for locally advanced breast cancer patients. *European Journal of Surgical Oncology*, 33(2):157–161.
- [78] Giannini, V., Vignati, A., Morra, L., Persano, D., Brizzi, D., Carbonaro, L., Bert, A., Sardanelli, F., and Regge, D. (2010). A fully automatic algorithm for segmentation of the breasts in DCE-MR images. In *2010 Annual International Conference of the IEEE Engineering in Medicine and Biology*, pages 3146–3149. IEEE.
- [79] Gilbert, F. J., Astley, S. M., McGee, M. A., Gillan, M. G. C., Boggis, C. R. M., Griffiths, P. M., and Duffy, S. W. (2006). Single reading with computer-aided detection and double reading of screening mammograms in the United Kingdom National Breast Screening Program. *Radiology*, 241(1):47–53.
- [80] Gilhuijs, K. G. A., Giger, M. L., and Bick, U. (1998). Computerized analysis of breast lesions in three dimensions using dynamic magnetic-resonance imaging. *Medical Physics*, 25(9):1647–1654.
- [81] Glaßer, S., Niemann, U., Preim, B., and Spiliopoulou, M. (2013). Can we distinguish between benign and malignant breast tumors in DCE-MRI by studying a tumor’s most suspect region only? In *Proceedings of CBMS 2013 - 26th IEEE International Symposium on Computer-Based Medical Systems*, pages 77–82. IEEE.

- [82] Gong, Y. C. and Brady, M. (2008). Texture-based simultaneous registration and segmentation of breast DCE-MRI. *Lecture Notes in Computer Science (including subseries Lecture Notes in Artificial Intelligence and Lecture Notes in Bioinformatics)*, 5116 LNCS:174–180.
- [83] Goodman, M. T., Tung, K.-H., and Wilkens, L. R. (2006). Comparative epidemiology of breast cancer among men and women in the US, 1996 to 2000. *Cancer causes & control : CCC*, 17(2):127–36.
- [84] Goshal, D. and Acharjya, P. P. (2012). MRI image segmentation using watershed transform. *International Journal of Emerging Technology and Advanced Engineering Website: www.ijetae.com (ISSN 2250-2459, Volume 2, Issue 4*, 373.
- [85] Goshtasby, A. A. (2005). *2-D and 3-D image registration: for medical, remote sensing, and industrial applications*. Wiley.com.
- [86] Graves, A., Liwicki, M., Fernández, S., Bertolami, R., Bunke, H., and Schmidhuber, J. (2009). A novel connectionist system for unconstrained handwriting recognition. *IEEE transactions on pattern analysis and machine intelligence*, 31(5):855–68.
- [87] Gromet, M. (2008). Comparison of computer-aided detection to double reading of screening mammograms: review of 231,221 mammograms. *AJR. American journal of roentgenology*, 190(4):854–9.
- [88] Gubern-Mérida, A., Kallenberg, M., Mann, R. M., Martí, R., Karssemeijer, N., Gubern-Merida, A., Kallenberg, M., Mann, R. M., Marti, R., and Karssemeijer, N. (2015a). Breast segmentation and density estimation in breast MRI: A fully automatic framework. *IEEE Journal of Biomedical and Health Informatics*, 19(1):349–357.
- [89] Gubern-Mérida, A., Kallenberg, M., Martí, R., and Karssemeijer, N. (2012). Segmentation of the pectoral muscle in breast MRI using atlas-based approaches. *Medical image computing and computer-assisted intervention : MICCAI ... International Conference on Medical Image Computing and Computer-Assisted Intervention*, 15(Pt 2):371–8.
- [90] Gubern-Mérida, A., Martí, R., Melendez, J., Hauth, J. L., Mann, R. M., Karssemeijer, N., and Platel, B. (2015b). Automated localization of breast cancer in DCE-MRI. *Medical image analysis*, 20(1):265–74.

-
- [91] Guyon, I. and Elisseeff, A. (2003). An Introduction to Variable and Feature Selection. *Journal of Machine Learning Research*, 3:1157–1182.
- [92] Hahn, S. Y., Ko, E. Y., Han, B. K., Shin, J. H., and Ko, E. S. (2014). Role of diffusion-weighted imaging as an adjunct to contrast-enhanced breast MRI in evaluating residual breast cancer following neoadjuvant chemotherapy. *European Journal of Radiology*, 83(2):283–288.
- [93] Hajdu, S. I. (2011). A note from history: landmarks in history of cancer, part 1. *Cancer*, 117(5):1097–102.
- [94] Hall, M., Frank, E., Holmes, G., Pfahringer, B., Reutemann, P., and Witten, I. H. (2009). The WEKA data mining software. *ACM SIGKDD Explorations Newsletter*, 11(1):10.
- [95] Han, L., Hipwell, J. H., Eiben, B., Barratt, D., Modat, M., Ourselin, S., and Hawkes, D. J. (2014). A nonlinear biomechanical model based registration method for aligning prone and supine mr breast images. *IEEE Transactions on Medical Imaging*, 33(3):682–694.
- [96] Haralick, R. M., Shanmugam, K., and Dinstein, I. (1973). Textural Features for Image Classification. *IEEE Transactions on Systems, Man, and Cybernetics*, 3(6):610–621.
- [97] Hasan, D. I., Mazrouh, M. A., and Tantawy, I. M. (2010). The value of dynamic MRI in the evaluation of the breast following conservative surgery and radiotherapy. *The Egyptian Journal of Radiology and Nuclear Medicine*, 41(4):469–473.
- [98] Hassanien, A. E., Kim, T.-h., Aboul Ella Hassanien, and Tai-hoon Kim (2012). Breast cancer MRI diagnosis approach using support vector machine and pulse coupled neural networks. *Journal of Applied Logic*, 10(4):277–284.
- [99] Havaei, M., Dutil, F., Pal, C., Larochelle, H., and Jodoin, P.-M. (2016). A Convolutional Neural Network Approach to Brain Tumor Segmentation. pages 195–208.
- [100] Hayton, P., Brady, M., Tarassenko, L., and Moore, N. (1997). Analysis of dynamic MR breast images using a model of contrast enhancement. *Medical image analysis*, 1(3):207–24.
- [101] Hennessy, J. L. and Patterson, D. A. (2011). *Computer architecture: a quantitative approach*. Morgan Kaufmann, 5 edition.

- [102] Herman, G. T. (2009). *Fundamentals of Computerized Tomography*. Advances in Pattern Recognition. Springer London, London, 2nd edition.
- [103] Hill, A., Mehnert, A., Crozier, S., Leung, C., Wilson, S., McMahon, K., and Kennedy, D. (2006). Dynamic breast MRI: image registration and its impact on enhancement curve estimation. *Conference proceedings : ... Annual International Conference of the IEEE Engineering in Medicine and Biology Society. IEEE Engineering in Medicine and Biology Society. Annual Conference*, 1:3049–52.
- [104] Hill, A., Mehnert, A., Crozier, S., and McMahon, K. (2009). Evaluating the accuracy and impact of registration in dynamic contrast-enhanced breast MRI. *Concepts in Magnetic Resonance Part B: Magnetic Resonance Engineering*, 35(2):106–120.
- [105] Hinton, G. E., Osindero, S., and Teh, Y.-W. (2006). A fast learning algorithm for deep belief nets. *Neural computation*, 18(7):1527–54.
- [106] Hipwell, J. H., Vavourakis, V., Han, L., Mertzaniidou, T., Eiben, B., and Hawkes, D. J. (2016). A review of biomechanically informed breast image registration. *Physics in medicine and biology*, 61(2):R1–R31.
- [107] Honda, E., Nakayama, R., Koyama, H., and Yamashita, A. (2016). Computer-Aided Diagnosis Scheme for Distinguishing Between Benign and Malignant Masses in Breast DCE-MRI. *Journal of Digital Imaging*, 29(3):388–393.
- [108] Hopp, T., Baltzer, P., Dietzel, M., Kaiser, W. A., and Ruiter, N. V. (2012). 2D/3D image fusion of X-ray mammograms with breast MRI: Visualizing dynamic contrast enhancement in mammograms. *International Journal of Computer Assisted Radiology and Surgery*, 7(3):339–348.
- [109] Hopp, T., Dietzel, M., Baltzer, P. A., Kreisel, P., Kaiser, W. A., Gemmeke, H., and Ruiter, N. V. (2013). Automatic multimodal 2D/3D breast image registration using biomechanical FEM models and intensity-based optimization. *Medical Image Analysis*, 17(2):209–218.
- [110] Hughes, G. (1968). On the mean accuracy of statistical pattern recognizers. *IEEE Transactions on Information Theory*, 14(1):55–63.
- [111] Hunt, K. K., Ames, F. C., Singletary, S. E., Buzdar, A. U., and Hortobagyi, G. N. (1996). Locally advanced noninflammatory breast cancer. *The Surgical clinics of North America*, 76(2):393–410.

- [112] Hylton, N. M., Gatsonis, C. A., Rosen, M. A., Lehman, C. D., Newitt, D. C., Partridge, S. C., Bernreuter, W. K., Pisano, E. D., Morris, E. A., Weatherall, P. T., Polin, S. M., Newstead, G. M., Marques, H. S., Esserman, L. J., and Schnall, M. D. (2016). Neoadjuvant Chemotherapy for Breast Cancer: Functional Tumor Volume by MR Imaging Predicts Recurrence-free Survival—Results from the ACRIN 6657/CALGB 150007 I-SPY 1 TRIAL. *Radiology*, 279(1):44–55.
- [113] Jafri, N. F., Newitt, D. C., Kornak, J., Esserman, L. J., Joe, B. N., and Hylton, N. M. (2014). Optimized breast MRI functional tumor volume as a biomarker of recurrence-free survival following neoadjuvant chemotherapy. *Journal of Magnetic Resonance Imaging*, 40(2):476–482.
- [114] Jayender, J., Chikarmane, S., Jolesz, F. A., and Gombos, E. (2014). Automatic segmentation of invasive breast carcinomas from dynamic contrast-enhanced MRI using time series analysis. *Journal of Magnetic Resonance Imaging*, 40(2):467–475.
- [115] Johansen, R., Jensen, L. R., Rydland, J., Goa, P. E., Kvistad, K. A., Bathen, T. F., Axelson, D. E., Lundgren, S., and Gribbestad, I. S. (2009). Predicting survival and early clinical response to primary chemotherapy for patients with locally advanced breast cancer using DCE-MRI. *Journal of Magnetic Resonance Imaging*, 29(6):1300–1307.
- [116] Johnsen, S. F., Taylor, Z. A., Clarkson, M. J., Hipwell, J., Modat, M., Eiben, B., Han, L., Hu, Y., Mertzanidou, T., Hawkes, D. J., and Ourselin, S. (2015). NiftySim: A GPU-based nonlinear finite element package for simulation of soft tissue biomechanics. *International Journal of Computer Assisted Radiology and Surgery*, 10(7):1077–1095.
- [117] Jones, E. F., Sinha, S. P., Newitt, D. C., Klifa, C., Kornak, J., Park, C. C., and Hylton, N. M. (2013). MRI Enhancement in Stromal Tissue Surrounding Breast Tumors: Association with Recurrence Free Survival following Neoadjuvant Chemotherapy. *PLoS ONE*, 8(5):e61969.
- [118] Juntu, J., Sijbers, J., De Backer, S., Rajan, J., and Van Dyck, D. (2010). Machine learning study of several classifiers trained with texture analysis features to differentiate benign from malignant soft-tissue tumors in T1-MRI images. *Journal of Magnetic Resonance Imaging*, 31(3):680–689.
- [119] Kaiser, W. A. (1990). Dynamic Magnetic Resonance Breast Imaging Using a Double Breast Coil: An Important Step Towards Routine Exam-

- ination of the Breast. In *Frontiers in European radiology*, pages 39–68. Springer.
- [120] Kannan, S., Ramathilagam, S., Devi, R., and Sathya, A. (2011). Robust kernel FCM in segmentation of breast medical images. *Expert Systems with Applications*, 38(4):4382–4389.
- [121] Kim, M., Wu, G., and Shen, D. (2011). Groupwise registration of breast DCE-MR images for accurate tumor measurement. In *2011 IEEE International Symposium on Biomedical Imaging: From Nano to Macro*, pages 598–601. IEEE.
- [122] Klein, S., Staring, M., Murphy, K., Viergever, M. A., and Pluim, J. P. W. (2010). Elastix: A toolbox for intensity-based medical image registration. *IEEE Transactions on Medical Imaging*, 29(1):196–205.
- [123] Korde, L. A., Zujewski, J. A., Kamin, L., Giordano, S., Domchek, S., Anderson, W. F., Bartlett, J. M. S., Gelmon, K., Nahleh, Z., Bergh, J., Cutuli, B., Pruneri, G., McCaskill-Stevens, W., Gralow, J., Hortobagyi, G., and Cardoso, F. (2010). Multidisciplinary meeting on male breast cancer: summary and research recommendations. *Journal of clinical oncology : official journal of the American Society of Clinical Oncology*, 28(12):2114–22.
- [124] Krishnan, S., Chenevert, T. L., Helvie, M. a., and Londy, F. L. (1999). Linear motion correction in three dimensions applied to dynamic gadolinium enhanced breast imaging. *Medical physics*, 26(5):707–14.
- [125] Krizhevsky, A., Sutskever, I., and Hinton, G. E. (2012a). ImageNet Classification with Deep Convolutional Neural Networks. *Advances In Neural Information Processing Systems*, pages 1–9.
- [126] Krizhevsky, A., Sutskever, I., and Hinton, G. E. (2012b). Imagenet classification with deep convolutional neural networks. In Pereira, F., Burges, C. J. C., Bottou, L., and Weinberger, K. Q., editors, *Advances in Neural Information Processing Systems 25*, pages 1097–1105. Curran Associates, Inc.
- [127] Kroon, D.-J. and Slump, C. H. (2009). MRI modalitiy transformation in demon registration. In *2009 IEEE International Symposium on Biomedical Imaging: From Nano to Macro*, pages 963–966. IEEE.

- [128] Kuerer, H. M., Newman, L. A., Smith, T. L., Ames, F. C., Hunt, K. K., Dhingra, K., Theriault, R. L., Singh, G., Binkley, S. M., Sneige, N., Buchholz, T. A., Ross, M. I., McNeese, M. D., Buzdar, A. U., Hortobagyi, G. N., and Singletary, S. E. (1999). Clinical course of breast cancer patients with complete pathologic primary tumor and axillary lymph node response to doxorubicin-based neoadjuvant chemotherapy. *Journal of clinical oncology : official journal of the American Society of Clinical Oncology*, 17(2):460–9.
- [129] Kuhl, C. (2007a). The current status of breast MR imaging. Part I. Choice of technique, image interpretation, diagnostic accuracy, and transfer to clinical practice. *Radiology*, 244(2):356–78.
- [130] Kuhl, C. K. (2007b). Current status of breast MR imaging. Part 2. Clinical applications. *Radiology*, 244(3):672–91.
- [131] Kuhl, C. K., Mielcareck, P., Klaschik, S., Leutner, C., Wardelmann, E., Gieseke, J., and Schild, H. H. (1999). Dynamic breast MR imaging: are signal intensity time course data useful for differential diagnosis of enhancing lesions? *Radiology*, 211:101–110.
- [132] Kybic, J. and Unser, M. (2003). Fast parametric elastic image registration. *IEEE Transactions on Image Processing*, 12(11):1427–1442.
- [133] Lai, C., Gong, L., Koved, L., Nadalin, A., and Schemers, R. (1999). User authentication and authorization in the java tm platform. In *Computer Security Applications Conference, 1999.(ACSAC'99) Proceedings. 15th Annual*, pages 285–290. IEEE.
- [134] Larsson, H. B., Stubgaard, M., S ndergaard, L., and Henriksen, O. (1994). In vivo quantification of the unidirectional influx constant for Gd-DTPA diffusion across the myocardial capillaries with MR imaging. *Journal of magnetic resonance imaging : JMRI*, 4(3):433–40.
- [135] LeCun, Y., Bengio, Y., and Hinton, G. (2015). Deep learning. *Nature*, 521(7553):436–444.
- [136] Lecun, Y., Bottou, L., Bengio, Y., and Haffner, P. (1998). Gradient-based learning applied to document recognition. *Proceedings of the IEEE*, 86(11):2278–2324.
- [137] Lee, A. W. C., Rajagopal, V., Babarenda Gamage, T. P., Doyle, A. J., Nielsen, P. M. F., and Nash, M. P. (2013). Breast lesion co-localisation

between X-ray and MR images using finite element modelling. *Medical Image Analysis*, 17(8):1256–1264.

- [138] Lee, S. H., Kim, J. H., Cho, N., Park, J. S., Yang, Z., Jung, Y. S., and Moon, W. K. (2010). Multilevel analysis of spatiotemporal association features for differentiation of tumor enhancement patterns in breast DCE-MRI. *Medical physics*, 37(8):3940–56.
- [139] Lee, S. H., Kim, J. H., Park, J. S., Chang, J. M., Park, S. J., Jung, Y. S., and Moon, W. K. (2008). Computerized Segmentation and Classification of Breast Lesions Using Perfusion Volume Fractions in Dynamic Contrast-enhanced MRI. In *2008 International Conference on BioMedical Engineering and Informatics*, pages 58–62. IEEE.
- [140] Lee, S. H., Kim, J. H., Park, J. S., Jung, Y. S., and Moon, W. K. (2009). Characterizing time-intensity curves for spectral morphometric analysis of intratumoral enhancement patterns in breast DCE-MRI: Comparison between differentiation performance of temporal model parameters based on DFT AND SVD. *Proceedings - 2009 IEEE International Symposium on Biomedical Imaging: From Nano to Macro, ISBI 2009*, pages 65–68.
- [141] Leinsinger, G., Schlossbauer, T., Scherr, M., Lange, O., Reiser, M., and Wismüller, A. (2006). Cluster analysis of signal-intensity time course in dynamic breast MRI: Does unsupervised vector quantization help to evaluate small mammographic lesions? *European Radiology*, 16(5):1138–1146.
- [142] Levman, J., Leung, T., Causer, P., Plewes, D., and Martel, A. L. (2008). Classification of dynamic contrast-enhanced magnetic resonance breast lesions by support vector machines. *IEEE Transactions on Medical Imaging*, 27:688–696.
- [143] Levman, J. and Martel, A. L. (2010). Computer-aided diagnosis of breast cancer from magnetic resonance imaging examinations by custom radial basis function vector machine. *Conference proceedings : ... Annual International Conference of the IEEE Engineering in Medicine and Biology Society. IEEE Engineering in Medicine and Biology Society. Conference*, 2010:5577–80.
- [144] Li, K.-L., Partridge, S. C., Joe, B. N., Gibbs, J. E., Lu, Y., Esserman, L. J., and Hylton, N. M. (2008). Invasive Breast Cancer: Predicting Disease Recurrence by Using High-Spatial-Resolution Signal Enhancement Ratio Imaging. *Radiology*, 248(1):79–87.

-
- [145] Li, X., Dawant, B. M., Welch, E. B., Chakravarthy, A. B., Freehardt, D., Mayer, I., Kelley, M., Meszoely, I., Gore, J. C., and Yankeelov, T. E. (2009). A nonrigid registration algorithm for longitudinal breast MR images and the analysis of breast tumor response. *Magnetic Resonance Imaging*, 27(9):1258–1270.
- [146] Liang, X., Sedai, S., Wang, H., Liang, S., Hashmi, N., Mcneillie, P., and Hashoul, S. (2015). Multi-atlas based segmentation of multiple organs in breast MRI. *SPIE medical imaging*, page 94133R.
- [147] Liao, S., Gao, Y., Oto, A., and Shen, D. (2013). Representation learning: a unified deep learning framework for automatic prostate MR segmentation. *Medical image computing and computer-assisted intervention : MICCAI ... International Conference on Medical Image Computing and Computer-Assisted Intervention*, 16(Pt 2):254–61.
- [148] Lin, M., Chen, J.-H., Wang, X., Chan, S., Chen, S., and Su, M.-Y. (2013). Template-based automatic breast segmentation on MRI by excluding the chest region. *Medical physics*, 40(12):122301.
- [149] Loeckx, D., Slagmolen, P., Maes, F., Vandermeulen, D., and Suetens, P. (2007). Nonrigid image registration using conditional mutual information. *Information processing in medical imaging : proceedings of the ... conference*, 20:725–37.
- [150] Long, J., Shelhamer, E., and Darrell, T. (2015). Fully convolutional networks for semantic segmentation. In *2015 IEEE Conference on Computer Vision and Pattern Recognition (CVPR)*, volume 14, pages 3431–3440. IEEE.
- [151] Lu, W., Yao, J., Lu, C., Prindiville, S., and Chow, C. (2006). DCE-MRI Segmentation and Motion Correction Based on Active Contour Model and Forward Mapping. In *Seventh ACIS International Conference on Software Engineering, Artificial Intelligence, Networking, and Parallel/Distributed Computing (SNPD'06)*, pages 208–212. IEEE.
- [152] Lucht, R., Delorme, S., and Brix, G. (2002). Neural network-based segmentation of dynamic MR mammographic images. *Magnetic resonance imaging*, 20(2):147–54.
- [153] Lucht, R. E. A., Knopp, M. V., and Brix, G. (2001). Classification of signal-time curves from dynamic MR mammography by neural networks. *Magnetic Resonance Imaging*, 19(1):51–57.

- [154] Maes, F., Collignon, A., Vandermeulen, D., Marchal, G., and Suetens, P. (1997). Multimodality image registration by maximization of mutual information. *IEEE transactions on medical imaging*, 16(2):187–98.
- [155] Mahmoudi, S. E., Akhondi-Asl, A., Rahmani, R., Faghih-Roohi, S., Taimouri, V., Sabouri, A., and Soltanian-Zadeh, H. (2010). Web-based interactive 2D/3D medical image processing and visualization software. *Computer methods and programs in biomedicine*, 98(2):172–82.
- [156] Maintz, J. B. and Viergever, M. A. (1998). A survey of medical image registration. *Medical image analysis*, 2(1):1–36.
- [157] Malich, A., Boehm, T., Facius, M., Freesmeyer, M. G., Fleck, M., Anderson, R., and Kaiser, W. A. (2001). Differentiation of mammographically suspicious lesions: evaluation of breast ultrasound, MRI mammography and electrical impedance scanning as adjunctive technologies in breast cancer detection. *Clinical radiology*, 56(4):278–83.
- [158] Mao, J., Yan, H., Brey, W. W., Bidgood, W. D., Steinbach, J. J., and Mancuso, A. (1993). Fat tissue and fat suppression. *Magnetic resonance imaging*, 11(3):385–93.
- [159] Marrone, S., Piantadosi, G., Fusco, R., Petrillo, A., Sansone, M., and Sansone, C. (2013). Automatic Lesion Detection in Breast DCE-MRI. In *Image Analysis and Processing (ICIAP)*, pages 359–368. Springer Berlin Heidelberg.
- [160] Marrone, S., Piantadosi, G., Fusco, R., Petrillo, A., Sansone, M., and Sansone, C. (2014). A Novel Model-Based Measure for Quality Evaluation of Image Registration Techniques in DCE-MRI. In *2014 IEEE 27th International Symposium on Computer-Based Medical Systems*, pages 209–214. IEEE, IEEE.
- [161] Marrone, S., Piantadosi, G., Fusco, R., Petrillo, A., Sansone, M., and Sansone, C. (2016). Breast segmentation using Fuzzy C-Means and anatomical priors in DCE-MRI. In *23rd International Conference on Pattern Recognition*.
- [162] Martel, A. L., Froh, M. S., Brock, K. K., Plewes, D. B., and Barber, D. C. (2007). Evaluating an optical-flow-based registration algorithm for contrast-enhanced magnetic resonance imaging of the breast. *Physics in Medicine and Biology*, 52(13):3803–3816.

- [163] MATLAB (2016). *version 9.1.0.441655 (R2016b)*. The MathWorks Inc., Natick, Massachusetts.
- [164] Mayerhoefer, M. E., Breitenseher, M., Amann, G., and Dominkus, M. (2008). Are signal intensity and homogeneity useful parameters for distinguishing between benign and malignant soft tissue masses on MR images?. Objective evaluation by means of texture analysis. *Magnetic Resonance Imaging*, 26(9):1316–1322.
- [165] McClymont, D., Mehnert, A., Trakic, A., Kennedy, D., and Crozier, S. (2014). Fully automatic lesion segmentation in breast MRI using mean-shift and graph-cuts on a region adjacency graph. *Journal of Magnetic Resonance Imaging*, 39(4):795–804.
- [166] McLaren, C. E., Chen, W.-P., Nie, K., and Su, M.-Y. (2009). Prediction of Malignant Breast Lesions from MRI Features. A Comparison of Artificial Neural Network and Logistic Regression Techniques. *Academic Radiology*, 16(7):842–851.
- [167] Meeuwis, C., van de Ven, S. M., Stapper, G., Fernandez Gallardo, A. M., van den Bosch, M. A. A. J., Mali, W. P. T. M., and Veldhuis, W. B. (2010). Computer-aided detection (CAD) for breast MRI: evaluation of efficacy at 3.0 T. *European radiology*, 20(3):522–8.
- [168] Meinel, L. A., Stolpen, A. H., Berbaum, K. S., Fajardo, L. L., and Reinhardt, J. M. (2007). Breast MRI lesion classification: Improved performance of human readers with a backpropagation neural network computer-aided diagnosis (CAD) system. *Journal of Magnetic Resonance Imaging*, 25(1):89–95.
- [169] Méndez, C. A., Pizzorni Ferrarese, F., Summers, P., Petralia, G., and Menegaz, G. (2012). DCE-MRI and DWI integration for breast lesions assessment and heterogeneity quantification. *International Journal of Biomedical Imaging*, 2012.
- [170] Mertzaniidou, T., Hipwell, J., Johnsen, S., Han, L., Eiben, B., Taylor, Z., Ourselin, S., Huisman, H., Mann, R., Bick, U., Karssemeijer, N., and Hawkes, D. (2014). MRI to X-ray mammography intensity-based registration with simultaneous optimisation of pose and biomechanical transformation parameters. *Medical Image Analysis*, 18(4):674–683.
- [171] Meyer-Baese, A., Schlossbauer, T., Lange, O., and Wismueller, A. (2009). Small Lesions Evaluation Based on Unsupervised Cluster Analysis

- of Signal-Intensity Time Courses in Dynamic Breast MRI. *International Journal of Biomedical Imaging*, 2009:1–10.
- [172] Mildenerger, P., Eichelberg, M., and Martin, E. (2002). Introduction to the DICOM standard. *European radiology*, 12(4):920–7.
- [173] Moftah, H. M., Azar, A. T., Al-Shammari, E. T., Ghali, N. I., Hassanien, A. E., and Shoman, M. (2014). Adaptive k-means clustering algorithm for MR breast image segmentation. *Neural Computing and Applications*, 24(7-8):1917–1928.
- [174] Mustra, M., Bozek, J., and Grgic, M. (2009). Breast border extraction and pectoral muscle detection using wavelet decomposition. In *IEEE EUROCON 2009*, pages 1426–1433. IEEE.
- [175] Mustra, M., Delac, K., and Grgic, M. (2008). Overview of the dicom standard. In *50th International Symposium ELMAR, 2008*, volume 1, pages 39–44. IEEE.
- [176] Myronenko, A. and Song, X. (2010). Intensity-based image registration by minimizing residual complexity. *IEEE Transactions on Medical Imaging*, 29(11):1882–1891.
- [177] Nagarajan, M. B., Huber, M. B., Schlossbauer, T., Leinsinger, G., Krol, A., and Wismüller, A. (2013a). Classification of Small Lesions in Breast MRI: Evaluating The Role of Dynamically Extracted Texture Features Through Feature Selection. *Journal of medical and biological engineering*, 33(1):59.
- [178] Nagarajan, M. B., Huber, M. B., Schlossbauer, T., Leinsinger, G., Krol, A., and Wismüller, A. (2013b). Classification of small lesions in dynamic breast MRI: Eliminating the need for precise lesion segmentation through spatio-temporal analysis of contrast enhancement over time. *Machine vision and applications*, 24(7):895–901.
- [179] Navaei-Lavasani, S., Fathi-Kazerooni, A., Saligheh-Rad, H., and Gity, M. (2015). Discrimination of Benign and Malignant Suspicious Breast Tumors Based on Semi-Quantitative DCE-MRI Parameters Employing Support Vector Machine. *Frontiers in Biomedical Technologies*, 2(2):87–92.
- [180] NEMA, N. E. M. A. (2004). Digital imaging and communications in medicine (dicom) part 1: Introduction and overview. http://medical.nema.org/dicom/2004/04_01PU.PDF.

-
- [181] Newell, D., Nie, K., Chen, J. H., Hsu, C. C., Yu, H. J., Nalcioglu, O., and Su, M. Y. (2010). Selection of diagnostic features on breast MRI to differentiate between malignant and benign lesions using computer-aided diagnosis: Differences in lesions presenting as mass and non-mass-like enhancement. *European Radiology*, 20(4):771–781.
- [182] Newitt, D. and Hylton, N. (2016). Single site breast DCE-MRI data and segmentations from patients undergoing neoadjuvant chemotherapy.
- [183] Newitt, D. C., Partridge, S. C., Chang, B., Joe, B. N., and Hylton, N. (2011). Optimization of the percent enhancement threshold for breast MRI tumor volume measurement during neoadjuvant treatment of breast cancer for predicting recurrence free survival time. *Proc Intl Soc Mag Reson Med (ISMRM)*, 19:508.
- [184] Nie, D., Wang, L., Gao, Y., and Sken, D. (2016). Fully convolutional networks for multi-modality isointense infant brain image segmentation. In *2016 IEEE 13th International Symposium on Biomedical Imaging (ISBI)*, volume 8, pages 1342–1345. IEEE.
- [185] Nodine, C. F. and Kundel, H. L. (1987). Using eye movements to study visual search and to improve tumor detection. *Radiographics : a review publication of the Radiological Society of North America, Inc*, 7(6):1241–50.
- [186] Ojala, T., Pietikainen, M., and Maenpaa, T. (2002). Multiresolution gray-scale and rotation invariant texture classification with local binary patterns. *IEEE Transactions on Pattern Analysis and Machine Intelligence*, 24(7):971–987.
- [187] Oracle Corporation (2011). Java authentication and authorization service reference guide. Retrieved February, 2014.
- [188] Ortiz, C. G. and Martel, a. L. (2012). Automatic atlas-based segmentation of the breast in MRI for 3D breast volume computation. *Medical Physics*, 39(2012):5835.
- [189] Otsu, N. (1979). A Threshold Selection Method from Gray-Level Histograms. *IEEE Transactions on Systems, Man, and Cybernetics*, 9(1):62–66.
- [190] Parker, G. J. M., Roberts, C., Macdonald, A., Buonaccorsi, G. A., Cheung, S., Buckley, D. L., Jackson, A., Watson, Y., Davies, K., and Jayson,

- G. C. (2006). Experimentally-derived functional form for a population-averaged high-temporal-resolution arterial input function for dynamic contrast-enhanced MRI. *Magnetic resonance in medicine*, 56(5):993–1000.
- [191] Partridge, S. C., Gibbs, J. E., Lu, Y., Esserman, L. J., Tripathy, D., Wolverton, D. S., Rugo, H. S., Hwang, E. S., Ewing, C. A., and Hylton, N. M. (2005). MRI measurements of breast tumor volume predict response to neoadjuvant chemotherapy and recurrence-free survival. *AJR. American journal of roentgenology*, 184(6):1774–81.
- [192] Peintinger, F., Symmans, W. F., Gonzalez-Angulo, A. M., Boughey, J. C., Buzdar, A. U., Yu, T. K., Hunt, K. K., Singletary, S. E., Babiera, G. V., Lucci, A., Meric-Bernstam, F., and Kuerer, H. M. (2006). The safety of breast-conserving surgery in patients who achieve a complete pathologic response after neoadjuvant chemotherapy. *Cancer*, 107(6):1248–54.
- [193] Penney, G. P., Weese, J., Little, J. A., Desmedt, P., Hill, D. L. G., Others, and Hawkes, D. J. (1998). A comparison of similarity measures for use in 2-D-3-D medical image registration. *IEEE transactions on medical imaging*, 17(4):586–595.
- [194] Pereira, S., Pinto, A., Alves, V., and Silva, C. A. (2016). Brain Tumor Segmentation Using Convolutional Neural Networks in MRI Images. *IEEE Transactions on Medical Imaging*, 35(5):1240–1251.
- [195] Periaswamy, S. and Farid, H. (2003). Elastic registration in the presence of intensity variations. *IEEE Transactions on Medical Imaging*, 22(7):865–874.
- [196] Perkins, C. I., Hotes, J., Kohler, B. A., and Howe, H. L. (2004). Association between breast cancer laterality and tumor location, United States, 1994-1998. *Cancer causes & control : CCC*, 15(7):637–45.
- [197] Peters, N. H. G. M., Borel Rinkes, I. H. M., Zuithoff, N. P. A., Mali, W. P. T. M., Moons, K. G. M., and Peeters, P. H. M. (2008). Meta-analysis of MR imaging in the diagnosis of breast lesions. *Radiology*, 246(1):116–24.
- [198] Piantadosi, G., Fusco, R., Petrillo, A., Sansone, M., and Sansone, C. (2015a). LBP-TOP for Volume Lesion Classification in Breast DCE-MRI. In *Lecture Notes in Computer Science (including subseries Lecture Notes in Artificial Intelligence and Lecture Notes in Bioinformatics)*, volume 9279, pages 647–657.

- [199] Piantadosi, G., Marrone, S., Fusco, R., Petrillo, A., Sansone, M., and Sansone, C. (2015b). Data-driven selection of motion correction techniques in breast DCE-MRI. In *2015 IEEE International Symposium on Medical Measurements and Applications (MeMeA) Proceedings*, pages 273–278, Torino, Italy. IEEE.
- [200] Piantadosi, G., Marrone, S., Sansone, M., and Sansone, C. (2013). A Secure OsiriX Plug-In for Detecting Suspicious Lesions in Breast DCE-MRI. In *Algorithms and Architectures for Parallel Processing*, pages 217–224. Springer International Publishing.
- [201] Piantadosi, G., Marrone, S., Sansone, M., and Sansone, C. (2015c). A secure, scalable and versatile multi-layer client–server architecture for remote intelligent data processing. *Journal of Reliable Intelligent Environments*, 1(2-4):173–187.
- [202] Pickles, M. D., Lowry, M., and Gibbs, P. (2016). Pretreatment Prognostic Value of Dynamic Contrast-Enhanced Magnetic Resonance Imaging Vascular, Texture, Shape, and Size Parameters Compared With Traditional Survival Indicators Obtained From Locally Advanced Breast Cancer Patients. *Investigative radiology*, 51(3):177–85.
- [203] Pickles, M. D., Lowry, M., Manton, D. J., Gibbs, P., and Turnbull, L. W. (2005). Role of dynamic contrast enhanced MRI in monitoring early response of locally advanced breast cancer to neoadjuvant chemotherapy. *Breast Cancer Research and Treatment*, 91(1):1–10.
- [204] Pickles, M. D., Manton, D. J., Lowry, M., and Turnbull, L. W. (2009). Prognostic value of pre-treatment DCE-MRI parameters in predicting disease free and overall survival for breast cancer patients undergoing neoadjuvant chemotherapy. *European Journal of Radiology*, 71(3):498–505.
- [205] Pluim, J. P. W., Maintz, J. B. a., and Viergever, M. a. (2003). Mutual information based registration of medical images: a survey. *IEEE Transactions on medical imaging*, XX(Y):1–21.
- [206] Preda, L., Villa, G., Rizzo, S., Bazzi, L., Origgi, D., Cassano, E., and Bellomi, M. (2006). Magnetic resonance mammography in the evaluation of recurrence at the prior lumpectomy site after conservative surgery and radiotherapy. *Breast Cancer Res*, 8(5):R53.

- [207] Quinlan, J. (1986). Induction of Decision Trees. *Machine Learning*, 1(1):81–106.
- [208] Reda, I., Shalaby, A., El-Ghar, M. A., Khalifa, F., Elmogy, M., Aboulfotouh, A., Hosseini-Asl, E., El-Baz, A., and Keynton, R. (2016). A new NMF-autoencoder based CAD system for early diagnosis of prostate cancer. *Proceedings - International Symposium on Biomedical Imaging*, 2016-June:1237–1240.
- [209] Roche, A., Malandain, G., Pennec, X., and Ayache, N. (1998). The correlation ratio as a new similarity measure for multimodal image registration. In *Medical Image Computing and Computer-Assisted Intervention (MICCAI)*, pages 1115–1124. Springer.
- [210] Rohlfing, T., Brandt, R., Menzel, R., and Maurer, C. R. (2004). Evaluation of atlas selection strategies for atlas-based image segmentation with application to confocal microscopy images of bee brains. *NeuroImage*, 21(4):1428–1442.
- [211] Rohlfing, T., Maurer, C. R., Bluemke, D. a., and Jacobs, M. A. (2003). Volume-preserving nonrigid registration of MR breast images using free-form deformation with an incompressibility constraint. *IEEE Transactions on Medical Imaging*, 22(6):730–741.
- [212] Rokach, L. (2007). *Data mining with decision trees: theory and applications*, volume 69. World Scientific.
- [213] Roozgard, A., Barzigar, N., Cheng, S., and Verma, P. (2012). Medical image registration using sparse coding and belief propagation. *Conference proceedings : ... Annual International Conference of the IEEE Engineering in Medicine and Biology Society. IEEE Engineering in Medicine and Biology Society. Annual Conference*, 2012(1):1141–4.
- [214] Roozgard, A., Barzigar, N., Verma, P., and Cheng, S. (2015). 3D-SCoBeP: 3D medical image registration using sparse coding and belief propagation. *International Journal of Diagnostic Imaging*, 2(1).
- [215] Rosado-Toro, J. A., Barr, T., Galons, J.-P., Marron, M. T., Stopeck, A., Thomson, C., Thompson, P., Carroll, D., Wolf, E., Altbach, M. I., and Rodríguez, J. J. (2015). Automated breast segmentation of fat and water MR images using dynamic programming. *Academic radiology*, 22(2):139–48.

-
- [216] Rosenblatt, F. (1961). Principles of neurodynamics. perceptrons and the theory of brain mechanisms. Technical report, DTIC Document.
- [217] Rosenfeld, A. and Kak, A. C. (2014). *Digital picture processing*, volume 1. Elsevier.
- [218] Rosset, A., Spadola, L., and Ratib, O. (2004). OsiriX: An Open-Source Software for Navigating in Multidimensional DICOM Images. *Journal of Digital Imaging*, 17(3):205–216.
- [219] Rueckert, D., Sonoda, L. I., Hayes, C., Hill, D. L. G., Leach, M. O., and Hawkes, D. J. (1999). Nonrigid registration using free-form deformations: application to breast MR images. *IEEE transactions on medical imaging*, 18(8):712–721.
- [220] Rumelhart, D. E., Hintont, G. E., and Williams, R. J. (1986). Learning representations by back-propagating errors. *Nature*, 323(6088):533–536.
- [221] Rumelhart, D. E. and McClelland, J. L. (1986). Parallel distributed processing: explorations in the microstructure of cognition. Volume 1. Foundations.
- [222] Russell, S. J., Norvig, P., Canny, J. F., Malik, J. M., and Edwards, D. D. (2010). *Artificial intelligence: a modern approach*. Prentice hall Englewood Cliffs, 3 edition.
- [223] Sak, H., Senior, A., and Beaufays, F. (2014). Long Short-Term Memory Based Recurrent Neural Network Architectures for Large Vocabulary Speech Recognition. *Nature*, 518(7540):529–33.
- [224] Sansone, M., Fusco, R., Petrillo, A., Petrillo, M., and Bracale, M. (2011). An expectation-maximisation approach for simultaneous pixel classification and tracer kinetic modelling in dynamic contrast enhanced-magnetic resonance imaging. *Medical & Biological Engineering & Computing*, 49(4):485–495.
- [225] Sathya, D. and Geetha, K. (2013a). Mass classification in breast DCE-MR images using an artificial neural network trained via a bee colony optimization algorithm. *ScienceAsia*, 39(3):294.
- [226] Sathya, J. and Geetha, K. (2013b). Experimental Investigation of Classification Algorithms for Predicting Lesion Type on Breast DCE-MR Images. *International Journal of Computer Applications*, 82(4):1–8.

- [227] Schabel, M. C. (2012). A unified impulse response model for DCE-MRI. *Magnetic resonance in medicine*, 68(5):1632–46.
- [228] Schabel, M. C., Morrell, G. R., Oh, K. Y., Walczak, C. A., Barlow, R. B., and Neumayer, L. A. (2010). Pharmacokinetic mapping for lesion classification in dynamic breast MRI. *Journal of magnetic resonance imaging : JMRI*, 31(6):1371–8.
- [229] Schnabel, J. A., Rueckert, D., Quist, M., Blackall, J. M., Castellano-Smith, A. D., Hartkens, T., Penney, G. P., Hall, W. A., Liu, H., Truwit, C. L., Gerritsen, F. A., Hill, D. L. G., and Hawkes, D. J. (2001). A generic framework for non-rigid registration based on non-uniform multi-level free-form deformations. *Lecture Notes in Computer Science (including subseries Lecture Notes in Artificial Intelligence and Lecture Notes in Bioinformatics)*, 2208:573–581.
- [230] Shahbazi-Gahrouei, D., Williams, M., and Allen, B. J. (2001). In vitro study of relationship between signal intensity and gadolinium-DTPA concentration at high magnetic field strength. *Australasian radiology*, 45(3):298–304.
- [231] Sinha, S., Lucas-Quesada, F. A., DeBruhl, N. D., Sayre, J., Farria, D., Gorczyca, D. P., and Bassett, L. W. (1997). Multifeature analysis of Gd-enhanced MR images of breast lesions. *Journal of Magnetic Resonance Imaging*, 7(6):1016–1026.
- [232] Sobin, L. H. and Fleming, I. D. (1997). TNM Classification of Malignant Tumors, fifth edition (1997). Union Internationale Contre le Cancer and the American Joint Committee on Cancer. *Cancer*, 80(9):1803–4.
- [233] Studholme, C., Hill, D., and Hawkes, D. (1996). Automated 3-D registration of MR and CT images of the head. *Medical Image Analysis*, 1(2):163–175.
- [234] Studholme, C., Hill, D. L. G., and Hawkes, D. J. (1995). Multiresolution voxel similarity measures for MR-PET registration. In *Information processing in medical imaging*, volume 3, pages 287–298. Dordrecht, The Netherlands: Kluwer.
- [235] Studholme, C., Hill, D. L. G., and Hawkes, D. J. (1997). Automated three-dimensional registration of magnetic resonance and positron emission tomography brain images by multiresolution optimization of voxel similarity measures. *Medical Physics*, 24(1):25.

- [236] Studholme, C., Hill, D. L. G., and Hawkes, D. J. (1999). An overlap invariant entropy measure of 3D medical image alignment. *Pattern Recognition*, 32:71–86.
- [237] Szabó, B. K., Aspelin, P., and Wiberg, M. K. (2004). Neural network approach to the segmentation and classification of dynamic magnetic resonance images of the breast: comparison with empiric and quantitative kinetic parameters. *Academic radiology*, 11(12):1344–54.
- [238] Tanner, C., Hawkes, D. J. D., Khazen, M., Kessar, P., Leach, M. O. M., and Hawkes, D. J. D. (2006). Does registration improve the performance of a computer aided diagnosis system for dynamic contrast-enhanced MR mammography? In *3rd IEEE International Symposium on Biomedical Imaging: Nano to Macro*, volume d, pages 466–469. IEEE.
- [239] Thévenaz, P., Ruttimann, U. E., and Unser, M. (1998). A pyramid approach to subpixel registration based on intensity. *IEEE transactions on image processing : a publication of the IEEE Signal Processing Society*, 7(1):27–41.
- [240] Thibault, G., Fertil, B., Navarro, C., Pereira, S., Cau, P., Levy, N., Sequeira, J., and Mari, J.-L. (2013). Shape and Texture Indexes Application to Cell Nuclei Classification. *International Journal of Pattern Recognition and Artificial Intelligence*, 27(01):1357002.
- [241] Tofts, P. S. (1997). Modeling tracer kinetics in dynamic Gd-DTPA MR imaging. *Journal of Magnetic Resonance Imaging*, 7(1):91–101.
- [242] Tofts, P. S., Brix, G., Buckley, D. L., Evelhoch, J. L., Henderson, E., Knopp, M. V., Larsson, H. B. W., Lee, T.-Y., Mayr, N. A., Parker, G. J. M., and Others (1999). Estimating kinetic parameters from dynamic contrast-enhanced T1-weighted MRI of a diffusable tracer: standardized quantities and symbols. *Journal of Magnetic Resonance Imaging*, 10(3):223–232.
- [243] Torheim, G., Godtliebsen, F., Axelsson, D., Kvistad, K. A., Haraldseth, O., and Rinck, P. A. (2001). Feature extraction and classification of dynamic contrast-enhanced T2*-weighted breast image data. *IEEE transactions on medical imaging*, 20(12):1293–301.
- [244] Torricelli, P., Pecchi, A., Luppi, G., and Romagnoli, R. (2003). Gadolinium-enhanced MRI with dynamic evaluation in diagnosing the local recurrence of rectal cancer. *Abdominal imaging*, 28(1):19–27.

- [245] Tuncbilek, N., Tokatli, F., Altaner, S., Sezer, A., Türe, M., Omurlu, I. K., and Temizoz, O. (2012). Prognostic value DCE-MRI parameters in predicting factor disease free survival and overall survival for breast cancer patients. *European Journal of Radiology*, 81(5):863–867.
- [246] Twellmann, T., Saalbach, A., Müller, C., Nattkemper, T. W., and Wismüller, A. (2004). Detection of suspicious lesions in dynamic contrast enhanced MRI data. *Conference proceedings : ... Annual International Conference of the IEEE Engineering in Medicine and Biology Society. IEEE Engineering in Medicine and Biology Society. Annual Conference*, 1:454–7.
- [247] Twellmann, T. and ter Haar Romeny, B. (2008). Computer-aided classification of lesions by means of their kinetic signatures in dynamic contrast-enhanced MR images. *Proceedings of SPIE*, 6915(September):69150J–69150J–9.
- [248] Tzacheva, A. A., Najarian, K., and Brockway, J. P. (2003). Breast cancer detection in gadolinium-enhanced mr images by static region descriptors and neural networks. *Journal of Magnetic Resonance Imaging*, 17(3):337–342.
- [249] Tzalavra, A., Dalakleidi, K., Zacharaki, E. I., Tsiaparas, N., Constantinidis, F., Paragios, N., and Nikita, K. S. (2016). Comparison of Multi-resolution Analysis Patterns for Texture Classification of Breast Tumors Based on DCE-MRI. In *Machine Learning in Medical Imaging*, pages 296–304. Springer International Publishing.
- [250] Vergnaghi, D., Monti, a., Setti, E., and Musumeci, R. (2001). A use of a neural network to evaluate contrast enhancement curves in breast magnetic resonance images. *Journal of digital imaging : the official journal of the Society for Computer Applications in Radiology*, 14(2):58–59.
- [251] Vignati, A., Giannini, V., Bert, A., Deluca, M., Morra, L., Persano, D., Martincich, L., and Regge, D. (2009). A fully automatic lesion detection method for DCE-MRI fat-suppressed breast images. *SPIE medical imaging*, 7260(July):726026–726026–12.
- [252] Vignati, A., Giannini, V., De Luca, M., Morra, L., Persano, D., Carbonaro, L. A., Bertotto, I., Martincich, L., Regge, D., Bert, A., and Sardanelli, F. (2011). Performance of a fully automatic lesion detection system for breast DCE-MRI. *Journal of Magnetic Resonance Imaging*, 34(6):1341–1351.

- [253] Viola, P. and Wells III, W. M. (1997). Alignment by Maximization of Mutual Information. *The International Journal of Computer Vision*, 24(2):137–154.
- [254] Vomweg, T. W., Buscema, M., Kauczor, H. U., Teifke, A., Intraligi, M., Terzi, S., Heussel, C. P., Achenbach, T., Rieker, O., Mayer, D., and Thelen, M. (2003). Improved artificial neural networks in prediction of malignancy of lesions in contrast-enhanced MR-mammography. *Medical physics*, 30:2350–2359.
- [255] Wan, T., Cao, J., Chen, J., and Qin, Z. (2017). Automated grading of breast cancer histopathology using cascaded ensemble with combination of multi-level image features. *Neurocomputing*, 229:34–44.
- [256] Wang, H., Dong, L., O’Daniel, J., Mohan, R., Garden, A. S., Ang, K. K., Kuban, D. a., Bonnen, M., Chang, J. Y., and Cheung, R. (2005). Validation of an accelerated ‘demon’s algorithm for deformable image registration in radiation therapy. *Physics in medicine and biology*, 50(12):2887–2905.
- [257] Wang, L., Filippatos, K., Friman, O., and Hahn, H. (2011). Fully automated segmentation of the pectoralis muscle boundary in breast MR images. *SPIE medical imaging*, 7963(October):796309–796309–8.
- [258] Wang, L., Platel, B., Ivanovskaya, T., Harz, M., and Hahn, H. K. (2012). Fully automatic breast segmentation in 3D breast MRI. In *2012 9th IEEE International Symposium on Biomedical Imaging (ISBI)*, pages 1024–1027. IEEE.
- [259] Wang, T. C., Huang, Y. H., Huang, C. S., Chen, J. H., Huang, G. Y., Chang, Y. C., and Chang, R. F. (2014). Computer-aided diagnosis of breast DCE-MRI using pharmacokinetic model and 3-D morphology analysis. *Magnetic Resonance Imaging*, 32(3):197–205.
- [260] Wang, Y., Morrell, G., Heibrun, M. E., Payne, A., and Parker, D. L. (2013). 3D multi-parametric breast MRI segmentation using hierarchical support vector machine with coil sensitivity correction. *Academic radiology*, 20(2):137–47.
- [261] Wang, Y., Sun, Z., Liu, C., Peng, W., and Zhang, J. (2016). MRI image segmentation by fully convolutional networks. In *2016 IEEE International Conference on Mechatronics and Automation*, pages 1697–1702. IEEE.

- [262] Wang, Z., Bovik, A. C., Sheikh, H. R., and Simoncelli, E. P. (2004). Image quality assessment: From error visibility to structural similarity. *IEEE Transactions on Image Processing*, 13(4):600–612.
- [263] Weinmann, H. J., Laniado, M., and Mützel, W. (1984). Pharmacokinetics of GdDTPA/dimeglumine after intravenous injection into healthy volunteers. *Physiological chemistry and physics and medical NMR*, 16(2):167–72.
- [264] West, J., Fitzpatrick, J. M., Wang, M. Y., Dawant, B. M., Maurer, C. R., Kessler, R. M., Maciunas, R. J., Barillot, C., Lemoine, D., Collignon, A., Maes, F., Suetens, P., Vandermeulen, D., van den Elsen, P. A., Napel, S., Sumanaweera, T. S., Harkness, B., Hemler, P. F., Hill, D. L., Hawkes, D. J., Studholme, C., Maintz, J. B., Viergever, M. A., Malandain, G., and Woods, R. P. (1997). Comparison and evaluation of retrospective intermodality brain image registration techniques. *Journal of computer assisted tomography*, 21(4):554–66.
- [265] Witten, I. H., Frank, E., and Hall, M. A. (2011). *Data Mining: Practical Machine Learning Tools and Techniques* (Google eBook).
- [266] Woods, B. J., Clymer, B. D., Kurc, T., Heverhagen, J. T., Stevens, R., Orsdemir, A., Bulan, O., and Knopp, M. V. (2007). Malignant-lesion segmentation using 4D co-occurrence texture analysis applied to dynamic contrast-enhanced magnetic resonance breast image data. *Journal of Magnetic Resonance Imaging*, 25(3):495–501.
- [267] Wu, S., Weinstein, S. P., Conant, E. F., Schnall, M. D., and Kontos, D. (2013). Automated chest wall line detection for whole-breast segmentation in sagittal breast MR images. *Medical physics*, 40(4):042301 1–12.
- [268] Xiaohua, C., Brady, M., Lo, J. J., and Moore, N. (2005). Simultaneous segmentation and registration of contrast-enhanced breast MRI. *Information Processing in Medical Imaging*, pages 31–59.
- [269] Xu, J., Xiang, L., Hang, R., and Wu, J. (2014). Stacked Sparse Autoencoder (SSAE) based framework for nuclei patch classification on breast cancer histopathology. In *2014 IEEE 11th International Symposium on Biomedical Imaging (ISBI)*, volume 35, pages 999–1002. IEEE.
- [270] Yang, C., White, J., and Li, X. (2012). Deformable Breast MRI and CT Registration for Radiation Treatment Planning Using B-spline With

- Rigidity and Feature Point Distance Regularization. *International Journal of Radiation Oncology*Biology*Physics*, 84(3):S111.
- [271] Yang, Q., Li, L., Zhang, J., Shao, G., Zhang, C., and Zheng, B. (2014). Computer-aided diagnosis of breast DCE-MRI images using bilateral asymmetry of contrast enhancement between two breasts. *Journal of Digital Imaging*, 27(1):152–160.
- [272] Young, H., Baum, R., Cremerius, U., Herholz, K., Hoekstra, O., Lammertsma, A. A., Pruim, J., and Price, P. (1999). Measurement of clinical and subclinical tumour response using [^{18}F]fluorodeoxyglucose and positron emission tomography: review and 1999 EORTC recommendations. *European journal of cancer (Oxford, England : 1990)*, 35(13):1773–82.
- [273] Zhao, G., Barnard, M., and Pietikäinen, M. (2009). Lipreading with local spatiotemporal descriptors. *IEEE Transactions on Multimedia*, 11:1254–1265.
- [274] Zhao, G. and Pietikäinen, M. (2007). Dynamic texture recognition using local binary patterns with an application to facial expressions. *IEEE Transactions on Pattern Analysis and Machine Intelligence*, 29:915–928.
- [275] Zheng, Y., Baloch, S., Englander, S., Schnall, M. D., and Shen, D. (2007). Segmentation and classification of breast tumor using dynamic contrast-enhanced MR images. *Medical image computing and computer-assisted intervention : MICCAI ... International Conference on Medical Image Computing and Computer-Assisted Intervention*, 10(Pt 2):393–401.
- [276] Zheng, Y., Englander, S., Baloch, S., Zacharaki, E. I., Fan, Y., Schnall, M. D., and Shen, D. (2009). STEP: Spatiotemporal enhancement pattern for MR-based breast tumor diagnosis. *Medical Physics*, 36(7):3192.
- [277] Zikic, D., Ioannou, Y., Criminisi, A., and Brown, M. (2014). Segmentation of Brain Tumor Tissues with Convolutional Neural Networks. In *MICCAI workshop on Multimodal Brain Tumor Segmentation Challenge (BRATS)*. Springer.
- [278] Zuo, C. S., Jiang, A., Buff, B. L., Mahon, T. G., and Wong, T. Z. (1996). Automatic motion correction for breast MR imaging. *Radiology*, 198(3):903–6.

List of figures

1.1	A female breast and its main parts.	6
1.2	Spatial incidence of breast cancer.	7
1.3	Magnetic moment and precession of a proton with spin. . . .	12
1.4	Raymond Damadian's: first 'Apparatus and method for detecting cancer in tissue.' [45]	13
1.5	MRI Scanner Gradient Magnets.	15
1.6	Neo-angiogenesis process induced by a malignant lesion. . .	16
1.7	Structure of a DCE-MRI. The four dimensions (3 spatial + 1 temporal) of a complete dynamic study.	17
1.8	Guidelines for visual analysis of TIC curves.	18
1.9	The first approach to CAD design.	21
1.10	A DCE-MRI segmented slice.	25
1.11	Overlap of a Segmented ROI mask with the ground-truth (for the 2D case).	34
2.1	Interest of the scientific community.	39
2.2	Pie-chart of the CAD tasks.	40

2.3	Pie-charts of the used features and the proposed approaches for the Lesion Detection task in the analysed literature works.	50
2.4	Pie-charts of the used features and the proposed approaches for the Tumour Diagnosis task in the analysed literature works.	55
2.5	Pie-chart of the features used for the Therapy Assessment in the analysed literature works.	58
2.6	Database size histogram.	63
2.7	Explicative use of serial DCE-MRI examinations during neoadjuvant chemotherapy for breast cancer.	64
3.1	Block diagram of the automated proposed CAD.	65
3.2	The breast mask extraction proposal at a glance.	68
3.3	The cuboid containing the Otsu segmented volume.	69
3.4	Automatic localisation of the nipples and of the chest-wall key-point.	70
3.5	Automatic localisation of the armpits, of the sternum key-point and of the heart key-point.	71
3.6	Action radius for each key-point.	72
3.7	The three fuzziness volumes for breast mask extraction. . . .	74
3.8	A representative case in which some evident artefacts are introduced by an improper MCT.	78
3.9	compartmental approach for the distribution of the contrast agent within the tissue.	84
3.10	Fitting of DCE-MRI sampled data by means of a physiological model (ETK-P).	87
3.11	Block diagram of the Lesion Detection method.	89
3.12	Examples of average TICs over the three types of ROIs. . . .	91
3.13	Block diagram of the lesion diagnosis approach.	93
3.14	LBP-TOP extraction strategy.	94
3.15	Normalized Area Under Curve map.	97

3.16	Block diagram of the therapy assessment Multiple Classifier System.	99
3.17	Layers overview of the proposed architecture for remote computing.	102
3.18	Client-Server communication protocol timing.	105
3.19	SSL Client Authenticated mode timing protocol.	107
3.20	Component level sequence diagram for a single job request execution. Rounded rectangles on temporal line represent state changing.	111
3.21	OsiriX GUI example.	113
3.22	The proposed architecture in the specific context of DCE-MRI evaluation, by using OsiriX and a previously proposed CAD tool (BLADeS [159 , 200]).	114
4.1	Processing flow for ‘reference ranking’ and assessment strategy.	123
4.2	Breastmask extraction stage-by-stage results (in transversal projection).	129
4.3	Final 3D reproduction of breast mask extracted with the proposed approach.	130
4.4	Result of sub-sampling strategy in terms of S-RCC over the sampling percentage.	131
4.5	Hit percentage over the sampling percentage.	132
4.6	DCE-MRI slice in a pre-contrast image with a manual selected ROI.	135
4.7	Detection results on a benign lesion.	136
4.8	Detection results on a malignant lesion.	136
4.9	Comparing lesion detection results for a benign lesion. . . .	139
4.10	Comparing lesion detection results for a malignant lesion. . .	139
4.11	LBP-TOP concatenated histograms per each orthogonal plane corresponding to the ROI showed in fig.4.6	140

4.12 ROC analysis for the proposed approach and for the competitors for the ROI diagnosis task.	143
4.13 ROC analysis for the proposed approach of Therapy Assessment over 42 patients.	145
4.14 Compression ratio comparison between different compression methods, including MATLAB.	148
4.15 Distribution of remote execution and transmission times using 1 CPU on server node.	149

List of tables

1.1	TNM table with stage and survival index at 5 years.	9
1.2	Some of the most important fields of DICOM header for magnetic resonance images.	23
1.3	Features type classification and description according to five major classes.	26
1.4	Dynamic features list.	27
1.5	Clinico-Pathologic features list.	28
1.6	Morphological features list.	28
1.7	Texural features list.	29
1.8	Physiological Based Pharmacokinetics Modelling features list.	30
2.1	Search criteria for the literature review.	38
2.2	Literature analysis of breast-masking approaches.	42
2.3	Distribution of MCTs in the literature works.	44
2.4	Motion Correction Techniques literature review.	45
2.5	Lesion Detection literature review.	49
2.6	Tumour Diagnosis literature review (1/2).	53
2.7	Tumour Diagnosis literature review (2/2).	54

2.8	Literature analysis of therapy assessment approaches for recurrence prediction.	57
2.9	Private datasets size for each work (1/2).	60
2.10	Private datasets size for each work (2/2).	61
2.11	Public datasets. Number of subjects, related works and available ground-truths are reported.	62
3.1	Key-Points action radii formulas.	72
3.2	Physiological Models Symbols.	84
3.3	Different subset of LBP-TOP feature for lesion diagnosis. . .	95
4.1	Lesions details for the private dataset ‘DSpascale42’.	119
4.2	DCE-MRI acquisition parameters for the different used dataset.	121
4.3	Performance comparison among different combination of proposed breast mask extraction method stages.	127
4.4	Comparison of the breast mask extraction proposed approach with some literature proposals (1/2).	127
4.5	Comparison of the breast mask extraction proposed approach with some literature proposals (2/2).	128
4.6	Reference ranking.	133
4.7	Comparison among QIs.	134
4.8	ROI detection performance over 26 patients.	137
4.9	ROI detection performance over 42 patients.	138
4.10	Performance comparison of the proposed method with other approaches.	138
4.11	Lesion diagnosis results per each combination of Motion Correction technique and Classifier.	141
4.12	Lesion diagnosis results per each Feature Set using the Random Forest as classifier and the Median Filter (5px) as Motion Correction technique.	141

4.13	Comparison among performances of our proposal, for ROI diagnosis, with different approaches in literature (on the private dataset).	142
4.14	Therapy assessment results. Training on ‘DSpublic64’ and Testing on ‘DSpublic162’.	144
4.15	Therapy assessment results. Training on ‘DSpublic162’ and Testing on ‘DSpublic64’.	144
4.16	Therapy assessment results on the union of ‘DSpublic64’ and ‘DSpublic162’.	145
4.17	Performance evaluation of the first stages up to the ROI Diagnosis.	146
4.18	Zip compression level impact on transmission time	147
4.19	Overhead in different network configuration.	149
4.20	Average execution times, throughput and speed-up in the different cases.	150